Searching for Innovative Thermionic Emitters and Understanding Their Work Functions Using Density Functional Theory Calculations

by

Tianyu Ma

A dissertation submitted in partial fulfillment of

the requirements for the degree of

Doctor of Philosophy

(Materials Science)

at the

University of Wisconsin-Madison

2021

Date of final oral examination: 05/25/2021

The dissertation is approved by the following members of the Final Oral Committee:

Dane Morgan, Professor, Materials Science and Engineering
John Booske, Professor, Electrical and Computer Engineering
Ryan Jacobs, Assistant Scientist, Materials Science and Engineering
Jason Kawasaki, Assistant Professor, Materials Science and Engineering
JR Schmidt, Professor, Chemistry

Abstract

The work function is a fundamental materials property which governs electron emission and has thus become a key design parameter for materials used in thermionic energy converters and vacuum electronic devices. In this dissertation, we use Density Functional Theory (DFT) calculations to search for low work function materials which is needed for efficient thermionic energy converters and compact high power terahertz vacuum electronic devices.

The first part of this dissertation establishes a systematic work function data set for rare-earth hexaborides, rare-earth tetraborides, and transition metal nitrides. The work function trends in these materials can be understood based on the atomic properties of their parent metals, i.e., electronegativity and atomic radius. We find Ba alloyed LaB_6 ($La_xBa_{1-x}B_6$) has lower work function than both endmembers, due to the positive surface dipole created by surface rumpling. We also propose HfN as a promising electron emitter material as it has a low work function comparable to pure LaB_6 according to our calculations.

In the second part of our work, we benchmark the accuracy of DFT calculated work functions for complex oxide surfaces. The results demonstrate a mean absolute error of ~0.2 eV between Heyd-Scuseria-Ernzerhof (HSE) calculated work functions and experimental values for select $SrTiO_3$ ideal and reconstructed surfaces. This accuracy is at the same level as that for elemental metals. By comparing work functions obtained from HSE functional and Perdew-Burke-Ernzerhof (PBE) functional, we find HSE functional yields more accurate work function values, while PBE functional seems to correctly capture the changes in work functions. We also explore the effects of common surface features, including vacancies, adatoms, reconstructions, and surface steps, on the work function.

The third part of our work is a high-throughput screening in search of low work function perovskite oxides. We use the linear correlation between the O *p*-band center and the work function to quickly predict work functions of 2913 perovskites. After further screening based on the stability under typical cathode operating conditions and electrical conductivity, we finally identify seven perovskites as promising thermionic cathode materials which are predicted to have low AO-terminated (001) surface work function, high stability, and high conductivity. We also discover a qualitative relationship between the work function and the number of *d* electrons, where perovskites with barely filled *d* bands have the lowest work functions while perovskites with empty *d* bands or nearly filled *d* bands have the highest work functions.

List of Publications

1. Jacobs, R., Lin, L., Ma, T., Lu-Steffes, O., Vlahos, V., Morgan, D. and Booske, J., 2018, April. Perovskite electron emitters: Computational prediction and preliminary experimental assessment of novel low work function cathodes. In *2018 IEEE International Vacuum Electronics Conference (IVEC)* (pp. 37-38). IEEE.
2. Ma, T., Jacobs, R., Booske, J. and Morgan, D., 2020. Understanding the interplay of surface structure and work function in oxides: A case study on SrTiO3. *APL Materials*, *8*(7), p.071110.
3. Ma, T., Jacobs, R., Booske, J. and Morgan, D., Discovery and engineering of low work function perovskite materials. (Submitted to Journal of Materials Chemistry C)
4. Ma, T., Jacobs, R., Booske, J. and Morgan, D., Work function trends and new low work function boride and nitride materials for electron emission applications. (Submitted to The Journal of Physical Chemistry C)
5. Lin, L., Jacobs, R., Ma, T., Chen, D., Morgan, D. and Booske, J., Work function, its measurement and engineering - a review. (In preparation)

List of Conference Presentations

1. Ma, T., Lin, L., Jacobs, R., Morgan, D. and Booske, J., Perovskite electron emitters - computational prediction and preliminary experimental assessment of novel low work function cathodes. 2018 Materials Research Society Fall Meeting. (Poster presentation)
2. Ma, T., Jacobs, R., Morgan, D. and Booske, J., Computational screening in search of low work function perovskite materials. 2019 International Vacuum Nanoelectronics Conference. (Oral presentation)
3. Ma, T., Jacobs, R., Morgan, D. and Booske, J., Searching for low work function perovskite oxides using Density Functional Theory. 2020 IEEE International Vacuum Electronics Conference. (Oral presentation)

Acknowledgements

I would like to first express my sincere thanks to my advisors, Prof. Dane Morgan and Prof. John Booske. All these works in this dissertation would not be accomplished without their constant support and guidance. During our weekly meetings, they have provided valuable suggestions on the critical science, and have reminded me when I was about to diverge from our original goal. I also have many thanks to my mentor, Dr. Ryan Jacobs. We have had many individual meetings on topics ranging from scientific details of VASP calculations to high-level research directions. My colleagues, Lin Lin and Dongzheng Chen, have had frequent discussions with me on various physics issues, which were all very helpful. I am grateful of all their helps and feel very lucky to work with these kind and knowledgeable people. I would also like to thank Prof. Jason Kawasaki and Prof. JR Schmidt for being my committee members and providing valuable insights and advice on my Ph.D. research.

This work would not have been possible without the significant research funds and services provided by the Defense Advanced Research Projects Agency (DARPA) through the Innovative Vacuum Electronic Science and Technology (INVEST) program; the Extreme Science and Engineering Discover Environment (XSEDE), which is supported by the National Science Foundation award number ACI-1548562; and the UW-Madison Center for High Throughput Computing (CHTC) in the Department of Computer Sciences.

Table of Contents

List of Figures

List of Tables

1. Introduction

1.1. Thesis overview

The work function, defined as the energy needed to move an electron from a solid to the vacuum immediately outside the solid surface, is a crucial electronic property which governs the electron emission. Therefore, a low work function material is critical in emission cathodes for the generation of the high emitted current density[1], [2] needed for the efficient use of thermionic and field emitters widely employed in high power, high frequency vacuum electronic device (VED) applications such as traveling wave tubes (TWTs),[3] klystrons,[4] gyrotrons,[5] and magnetrons.[6] These devices are crucial components in diverse applications ranging from communications, industrial food production, national defense, deep space exploration, and scientific research.[7]

The majority of commercial cathodes are lanthanum hexaboride (LaB_6) cathodes and impregnated cathodes.[8] LaB_6 has been used for decades without essential changes, and there is no comprehensive study which provides understanding of work function trends of the complete set of hexaborides and demonstrates that LaB_6 indeed has the lowest work function among all pure rare-earth hexaborides. Impregnated cathodes are porous tungsten matrix with impregnants of different compositions. Such cathodes rely on a surface dipole layer formed from the impregnants to reduce the work function, however, this pivotal dipole layer is volatile and therefore limits the cathodes' lifetime and emission uniformity.[9]

In this dissertation, we sought to search for new low work function materials for electron emission applications, and provide the understanding of their work functions by using Density Functional Theory (DFT) calculations. In Chapter 3, we perform DFT calculations on all rare-earth hexaborides to demonstrate work function trends. We also investigate rare-earth tetraborides

and transition metal nitrides (TMNs), which are refractory and electrically conductive like hexaborides, and may also be promising electron emitters. In Chapter 4, we benchmark the accuracy of DFT-calculated work functions for complex oxide surfaces, and systematically assess the impact of typical surface features on oxide work functions. Next in Chapter 5, to find better substitution for impregnated cathodes, we study perovskite oxides ($A_{1-x}A_x'B_{1-y}B_y'O_3$) which can possess intrinsic polar surface that facilitates low work function without volatile exotic dipole layer.

1.2. Review on lanthanum hexaboride (LaB_6) and dispenser cathodes

In this section, we will briefly review the two most common commercial cathodes, and show potential opportunities to improve their performance. Materials used as thermionic electron emitters broadly fall into two groups: monolithic cathodes and dispenser cathodes.[8] Monolithic cathodes consist of a single, non-porous material, which natively contains low work function surfaces without the presence of additional work function-lowering species. Dispenser cathodes, such as the classic Ba-impregnated cathode and newer scandate cathode, typically consist of a porous tungsten body infiltrated with an alkaline-earth containing emission mix.[8] At high temperature, the emission mix decomposes and reacts with oxygen to form work-function-lowering dipole species.[9]–[11] For many applications, the chief advantages of employing a monolithic material are improved lifetime, more reliable device performance (the volatile surface species can desorb and cause performance issues in many devices), and more straightforward material processing and activation.[12] The main disadvantage of using monolithic materials is that they tend to have higher work functions than dispenser cathodes (e.g. about 0.5-1 eV higher, depending on the precise materials considered).[8]

A seminal event in the development of modern monolithic thermionic emitters came in 1951, when Lafferty, studying the electron emission properties of several hexaborides, found that lanthanum hexaboride (LaB_6) displayed outstanding thermionic emission properties, with a low measured work function of about 2.6 eV.[13] This discovery by Lafferty later spurred tremendous interest in this material space, with many following studies making progress in LaB_6 materials processing to successfully synthesize single crystal LaB_6, in-depth studies of surface-dependent work function to further assess emission performance and guide single crystal engineering,[14], [15] and stability studies which found that LaB_6 has low vapor pressure at high temperature, ensuring sufficient material stability at elevated temperatures for thousands of hours of collective emission.[15], [16] As a result of these attractive materials properties, LaB_6 has been used for decades as a commercial electron source in applications needing a combination of high brightness and long life, such as electronic propulsion systems, electron microscopes, lithography systems, electron-beam welders, X-ray sources, and free electron lasers.[12], [17], [18] As one of the main electron emitters used in numerous commercial applications, LaB_6 has remained essentially unchanged for last fifty years. Despite the large number of studies on hexaboride emitters, they are often limited to one or a few hexaborides, and different studies adopt different sample preparation conditions and/or measurement methods. These differences can make one-to-one comparison of results difficult, and make chemical trends or effects of different surfaces challenging to discern. Importantly, to our knowledge there is no study which comprehensively evaluates and provides understanding of work function trends of the complete set of rare-earth hexaborides. Such knowledge may suggest possible avenues toward designing new boride materials with lower work function than LaB_6.

Impregnated W cathodes consists of a porous tungsten body impregnated with electron emission promoting materials such as a CaO-Al_2O_3-BaO mixture. During activation, free Ba atoms diffuse to the W surface and form a Ba-O monolayer[10], which acts as a surface dipole[11] and lowers the effective work function of the cathode from 4.5 eV (the average value of bare polycrystalline W) to about 2 eV.[8] The impregnated cathode has been further engineered to include an Os/Ru thin film coating, resulting in a further reduced work function of about 1.8 eV (the so-called "M-type" cathode).[19] The newest generation of impregnated W cathode is the scandate cathode where Sc_2O_3 is added into the impregnant. These cathodes have gained much research interest in the past 25 years due to their extremely low work function of about 1.1 eV and ability to realize ultra-high emitted current densities in excess of 100 A/cm^2.[20]–[24] Despite the commercial use of impregnated cathodes and decades of research on scandate cathodes, they all have important shortcomings. Namely, these cathodes suffer from Ba depletion[25], [26] and surface degradation[19] as a result of the continual evaporation of Ba from the emitting surface during high temperature operation. This off-gassing of the work-function-lowering Ba species limits the cathode lifetime. In addition, impregnated cathodes can experience non-uniform Ba coverage, leading to device efficiency limits[27] and engineering challenges.[28] For the specific case of scandate cathodes, the previous shortcomings all apply, but scandate cathodes tend to require extra activation and have issues of manufacturing and performance repeatability.[24], [29]–[31] These above-mentioned issues all stem from the fact that impregnated cathodes realize their low work function through the formation of a volatile surface dipole layer believed to be comprised mainly of Ba and O. While much study has been devoted to understanding the surface chemistry, atomic-scale structures and resultant work functions of the surface dipole species for B-type, M-type and scandate cathodes,[9], [11], [32]–[35] the natural materials design question

becomes: is there a different material one could use as an electron emitter that can reach low work function without extra surface layer, and therefore not be prone to the critical issue of limited cathode lifetime? The discovery and design of such a stable, low work function, ultra-long-lifetime electron emission material may ultimately enable the deployment of high-power, high frequency VEDs and related devices that can operate at lower temperatures, realize high emitted current densities, and reduce operational and device replacement costs.

1.3. Review of low work function perovskite materials

The key to address the aforementioned materials design question is to find a class of materials which have stable intrinsic surface dipoles that can lower the work function. In this dissertation we turn our attention to perovskite oxide materials as a potential solution. In general, perovskites are a broad class of materials known for their high degree of compositional flexibility, where their structure can support upwards of 90% of the elements in the periodic table (within some solubility limit) without losing its three-dimensional interconnected network of octahedra.[36] This high degree of compositional flexibility enables perovskites to have a wide range of tunable properties, including tunable work function values. The recent studies of Jacobs *et al.*[37] and Zhong *et al.*[38] both demonstrated that the work function of perovskite materials can vary on the scale of several eV, and depends on the bulk material composition, the surface orientation (e.g. (001) versus (011)), and the surface termination (e.g. AO- versus BO_2-terminated (001) surface). These studies were the first to characterize the work functions of a representative set of perovskite oxides using DFT methods for applications in electron emission and heterojunction engineering, and suggest that perovskites with low work functions may be realized by virtue of the polar (001) oriented surfaces of the perovskite structure.[37], [38] Jacobs *et al.*

also identified an approximate linear correlation between (001) surface work function and the bulk O *p*-band center.[37]

The O *p*-band center can be obtained from a single DFT bulk structure relaxation run. This established correlation of surface work function with bulk O *p*-band center enables fast screening of perovskite work functions at a rate that is approximately two orders of magnitude faster than conducting computationally expensive surface slab calculations. Jacobs *et al.* specifically identified $SrVO_3$ as a promising cathode material with a calculated (001) SrO terminated work function of about 1.9 eV and predicted that Ba dopant impurities in $SrVO_3$ should segregated onto the (001) surface, creating a BaO-terminated (001) surface with a very low work function of 1.1 eV[37]. Meanwhile, $SrVO_3$ has been experimentally shown to be a good electronic conductor and stable under reducing conditions.[39], [40] These properties make $SrVO_3$ a promising electron emission cathode material worthy of further study. And these results also suggest that there might be other perovskite oxides possessing low work function, good electrical conductivity, and good chemical stability, and thus are promising electron emission materials.

1.4. Work function related applications

VEDs are devices that can generate or amplify electromagnetic waves throughout the microwave and millimeter wave bands using the interaction between an electron beam and a magnetic field. VEDs have been widely used in satellite communications, radars, medical detections, and many other civilian, military, scientific, and industrial applications.[7] The International Linear Collider (ILC) uses high power klystrons as the power source for the accelerator.[41] High power terahertz (THz) VEDs are especially needed for noninvasive sensing, high-data-rate communications, high resolution radar, and analysis fluids and condensed matter.[7]

To achieve compact high power THz VEDs, a high current density electron beam is necessary, and a practical approach would be using magnetic and electrostatic fields to compress an electron beam of ~10 A/cm^2 to ~100 A/cm^2. However, 10 A/cm^2 is a high current density for conventional cathodes that will rapidly exhaust their lifetime. For example, conventional M cathode with a work function of 1.85 eV can produce 5 A/cm^2 current density at 1020 °C for over 50,000 h. However, to reach 10 A/cm^2 current density, the temperature must be elevated to 1200 °C and the lifetime is significantly reduced to 1,000 h due to exacerbated depletion of the volatile surface layer.[9] Therefore, a novel cathode with low work function and robust surface is necessary for long-lived THz VEDs.

Electron beams and X-rays are commonly used to probe the electronic structure and real-space geometry of materials. And low work function cathodes are essential parts in contemporary imaging equipment, such as X-ray diffractometer (XRD), scanning electron microscope (SEM), and transmission electron microscope (TEM), to directly generate electron beams or indirectly generate X-rays by colliding with a metal target. Cathodes with lower work function are desired to provide electron beams with higher brightness and harder X-rays.

The work function is not always the lower the better. An example is photon-enhanced thermionic emission (PETE) energy converter[42], [43] which harvests solar energy to produce electricity at temperatures exceeding 200 ◦C. A PETE device consists of a hot cathode and a cooler anode separated by a vacuum gap. The cathode is a p-type semiconductor, in which the electrons are excited into the conduction band by solar radiation. Then the electrons rapidly thermalize to the equilibrium distribution and diffuse throughout the cathode. Finally, electrons with energies greater than the electron affinity of the cathode can emit from the cathode surface to the anode, generating electricity current. In such process, each electron harvests solar energy to overcome the

band gap, and also thermal energy to overcome the electron affinity. Benefitting from this ‘thermal boost’, the total voltage of a PETE device is higher than a regular photovoltaic system of the same band gap, and unused heat from the PETE cycle can be collected and utilized by an additional thermal engine, therefore making the best use of the solar energy.

The current density generated from a PETE device is identical to that of mere thermionic emission, except that the energy barrier is lowered by the difference between the quasi-Fermi level with photoexcitation and the Fermi level without photoexcitation. The power output of a PETE converter is the product of the current density and the operating voltage, which is given by the difference between the cathode and the anode work function. To maximize the output, the cathode work function should balance between the current density and the operating voltage to reach the optimal value, while the anode work function should be as low as possible. Such complicated device design requires the capability of tuning the work function in both directions.

2. Background

2.1. Work function and electron emission

2.1.1. Definition of the work function

The work function is the minimum energy required to move an electron from a solid to its immediate vacuum. Here immediate vacuum means the distance is larger than lattice constant but smaller than grain size, so that the emitted electron still feels the electric dipole of specific crystal surface.

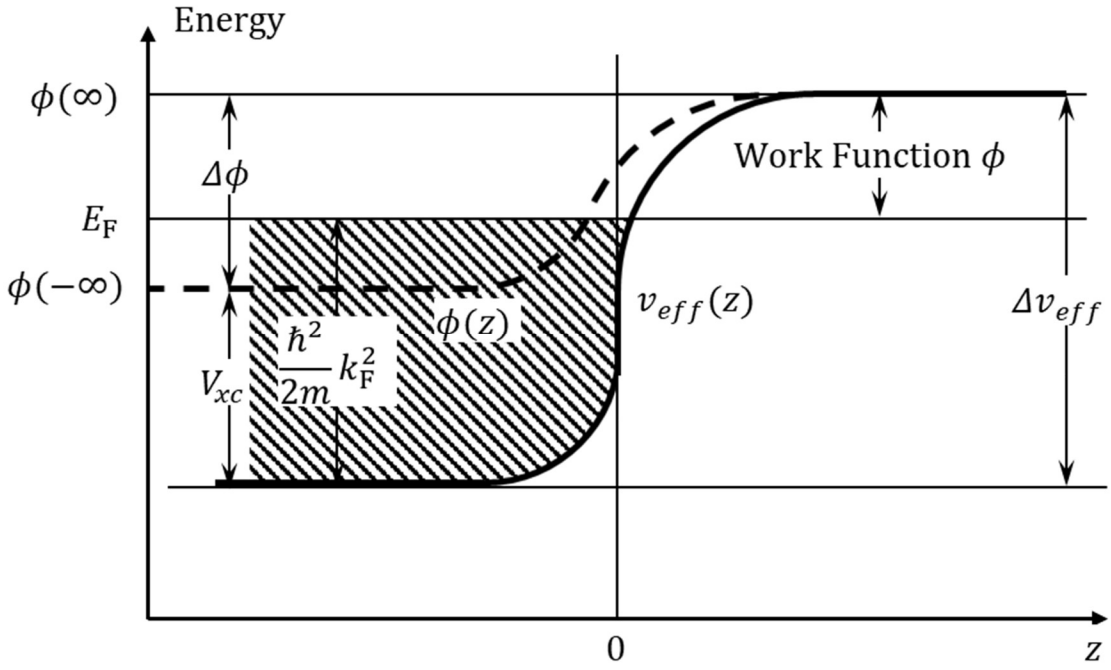

Figure 2.1: Schematic potential well diagram in a solid.

As shown in Figure 2.1, the potential well Δv_{eff} in which electrons are confined in a solid can be decomposed to two components, the cohesive force potential V_{xc}, and the electrostatic force potential $\Delta\phi$. The former one is a bulk property that arises from the electrostatic interactions

among electrons in the solid, and the latter one is a surface property depends on the surface dipole originating from atomic surface structures.

Electrons are filled in such potential well until the Fermi wave number k_{F} is reached. Thus, the electron filling is completed when the electron with energy $E_{\mathrm{F}} = (\hbar^2/2m)k_{\mathrm{F}}^2$ is filled in place, and the work function is $\phi = \Delta v_{eff} - E_{\mathrm{F}}$. Under such definition, the work function ϕ is anisotropic because anisotropic surface dipole generates different electrostatic force potential $\Delta\phi$.

2.1.2. Electron emission and work function measurement

Electron emission is directly governed by the work function. Physically there are many types of electron emission: thermionic emission and field emission are the most common electron emission mechanisms used in vacuum electronics; photoemission is widely employed in experimental measurements to obtain sample's work function;[44] and there are also secondary electron emission and so forth.

In thermionic emission, electrons gain thermal energy and overcome the potential energy barrier between the solid and the vacuum. Richardson-Laue-Dushman (RLD) equation,[45] named after the Nobel Prize winner Owen Willans Richardson, describes the current density from thermionic emission in the temperature-limited region

$$J = \lambda_R A_0 T^2 e^{-\frac{\phi}{kT}} \tag{2.1}$$

where λ_{R} is a material-specific correction factor and $A_0 = \frac{4\pi m k^2 e}{h^3}$ is Richardson constant. According to Richardson's law, the thermionic emission current density is dictated exponentially by the work function, lower work function will significantly increase current density.

The thermionic current density cannot infinitely increase as temperature raises, it is of course limited by the melting temperature of the solid, and it is also limited by space charge limit, which is described by the Child-Langmuir law[46], [47]

$$J = \frac{4\epsilon_0}{9}\sqrt{2e/m_e}\frac{V_a^{3/2}}{d^2} \tag{2.2}$$

where d is the distance between cathode and anode, and V_a is the anode voltage. The existence of space charge limit is due to the repulsion of the cloud of electrons in the solid's neighborhood.

Thermionic emission could be used to measure the work function. Following Richardson's law, the work function ϕ is usually obtained by fitting both Richardson constant and work function with experimental $J-T$ data. However, the fitted Richardson constant may differ from its theoretical value by many orders of magnitude,[48], [49] and sometimes the linear relationship between $\ln(J/T^2)$ and $1/T$ may break in extended range of temperatures.[50] In such anomalous situations, using fitted Richardson constant or theoretical Richardson constant could result in quite different work function values. Therefore, it is important to examine the Richardson constant when evaluating the work function value obtained from thermionic emission.

Field emission is the quantum mechanical tunneling of electrons to vacuum through the work function barrier with applied external electric field at high intensity (~10^9 V/m). The field emission current density is formulated as Fowler-Nordheim equation[1]

$$J = \frac{AF^2}{\Phi}e^{-\frac{B\Phi^{3/2}}{F}} \tag{2.3}$$

where $A = e^2/8\pi ht^2(\Phi,F)$ and $B = 4\sqrt{2m_e}v(\Phi,F)/3e\hbar$, F is the applied electric field, $v(\Phi,F)$ and $t(\Phi,F)$ are both correction factors. The work function can also be obtained from fitting the Fowler-Nordheim equation, while in practice, there is complexity due to entangled

emission current density and electric field,[51] and the distortion in Fowler-Nordheim equation under high current density.

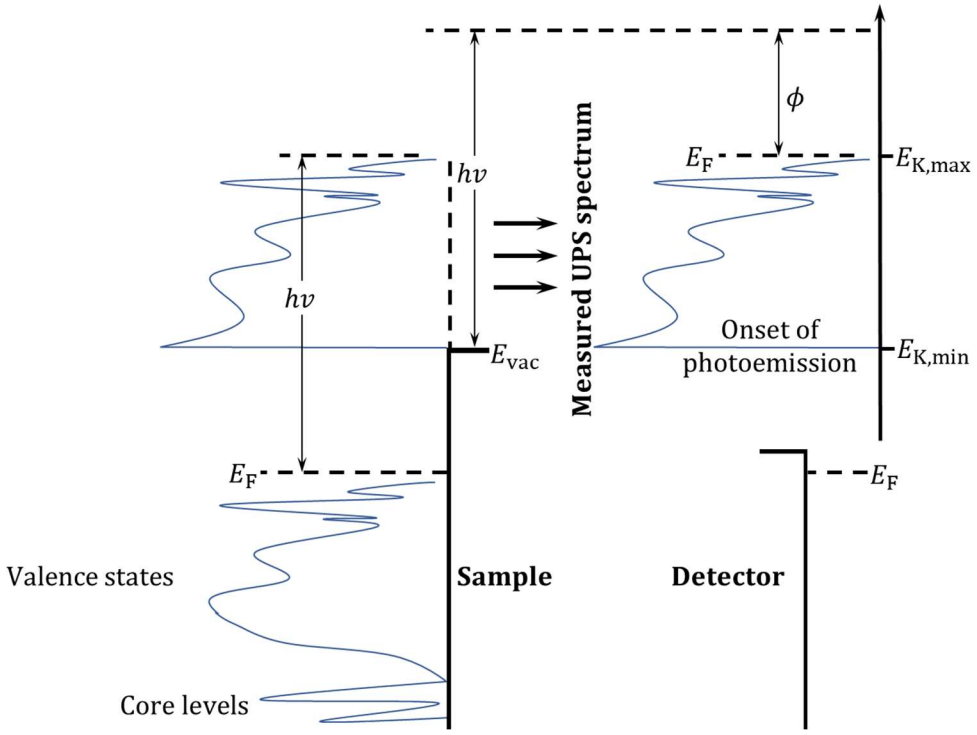

Figure 2.2: Schematic diagram demonstrating UPS work function measurement.

Photoemission obeys Einstein's photoelectric equation:[52]

$$\phi = hv - E_{K,max} \quad 2.4$$

Despite the simplicity of the equation, the work function cannot be directly derived from measuring the maximum photoelectron kinetic energy, because the vacuum level between the sample and the collector is not flat, thus accelerating or decelerating the photoelectrons; and the collector has its own work function which would modify the kinetic energy of the photoelectrons. In practice, X-ray photoelectron spectroscopy (XPS) or ultraviolet photo-electron spectroscopy (UPS) measures the onset of photoemission and the maximum kinetic energy $E_{K,max}$, namely the photoemission spectrum band width W, as shown in Fig 2.2. By observing the band diagram at

the sample surface, the spectrum band width can also be expressed as $W = E_{\mathrm{F}} - (E_{\mathrm{va}} - h\nu)$, therefore,[53]

$$\begin{aligned} \phi &= E_{\mathrm{vac}} - E_{\mathrm{F}} \\ &= h\nu + E_{\mathrm{vac}} - h\nu - E_{\mathrm{F}} \\ &= h\nu - W \end{aligned} \tag{2.5}$$

2.2. Density Functional Theory (DFT) fundamentals

2.2.1. Derivation and formalism

Density Functional Theory (DFT) is a computational quantum mechanical modeling method used to investigate the electronic structure of many-body systems.

In an N-electron system, based on Born-Oppenheimer approximation,[54] the atomic nuclei can be treated as fixed, and the electrons are in a static potential exerted by those atomic nuclei. The wavefunction of the N electrons $\Psi(\vec{r}_1, \ldots, \vec{r}_N)$ then satisfies the time-independent Schrödinger equation[55]

$$\hat{H}\Psi(\vec{r}_1, \ldots, \vec{r}_N) = E\Psi(\vec{r}_1, \ldots, \vec{r}_N) \tag{2.6}$$

where E is the total energy, and $\hat{H}$ is the Hamiltonian which can be expressed as

$$\hat{H} = \sum_i^N \left(-\frac{\hbar^2}{2m}\nabla_i^2\right) + \sum_i^N V(\vec{r}_i) + \sum_{i<j}^N U(\vec{r}_i, \vec{r}_j) \tag{2.7}$$

The first term is the kinetic energy, the second term is the potential energy from the field generated by the atomic nuclei, and the third term represents electron-electron interaction energy. The many-body wavefunction has 3N dimensions, and due to the interaction term in the Hamiltonian, this many-body Schrödinger equation cannot be decomposed to simpler single-particle equations. Therefore, for systems of scientific interest which usually contain hundreds of electrons, directly solving their many-body Schrödinger equation is computationally intractable.

The development of DFT addressed this issue by providing a method to map a 3N-dimensional many-body Schrödinger equation onto N 3-dimensional single-particle Kohn-Sham equations. The cornerstone of DFT was established by Pierre Hohenberg and Walter Kohn, where they proved that the ground-state energy is a functional of electron density,[56] and the correct electron density minimizes the energy functional. Walter Kohn and Lu Jeu Sham then further developed the above theorem and successfully reduced the many-body Schrödinger equation to tractable Kohn-Sham equations,[57] which adopt the form

$$\left[-\frac{\hbar^2}{2m}\nabla^2 + V(\vec{r}) + V_H(\vec{r}) + V_{XC}(\vec{r})\right]\varphi_i(\vec{r}) = \varepsilon_i\varphi_i(\vec{r}) \qquad 2.8$$

where $\varphi_i(\vec{r})$ is the single-electron wavefunction and ε_i is the electron energy level. On the left side of the Kohn-Sham equation, the first term in the parenthesis is the kinetic energy operator, $V(\vec{r})$ represents the potential energy of the electron in the field generated by the atomic nuclei, $V_H(\vec{r})$ is the Hartree term describing the electron-electron Coulomb repulsion, and $V_{XC}(\vec{r})$ denotes the exchange-correlation potential. With the single-electron wavefunctions calculated from Kohn-Sham equations, one can reproduce the electron density of the original many-body system by

$$n(\vec{r}) = \sum_i^N \varphi_i^*(\vec{r})\varphi_i(\vec{r}) \qquad 2.9$$

Here we can notice that the electron density $n(\vec{r})$ is calculated from potentials $V_H(\vec{r})$ and $V_{XC}(\vec{r})$, while these two potentials in turn depend on the electron density, therefore, Kohn-Sham equations must be solved self-consistently: one begins with an assumed electron density $n(\vec{r})$, calculate wavefunctions $\varphi_i(\vec{r})$ and construct new electron density $n(\vec{r})$, repeat above iteration until the electron density $n(\vec{r})$ reaches self-consistency, as shown in Figure 2.3.

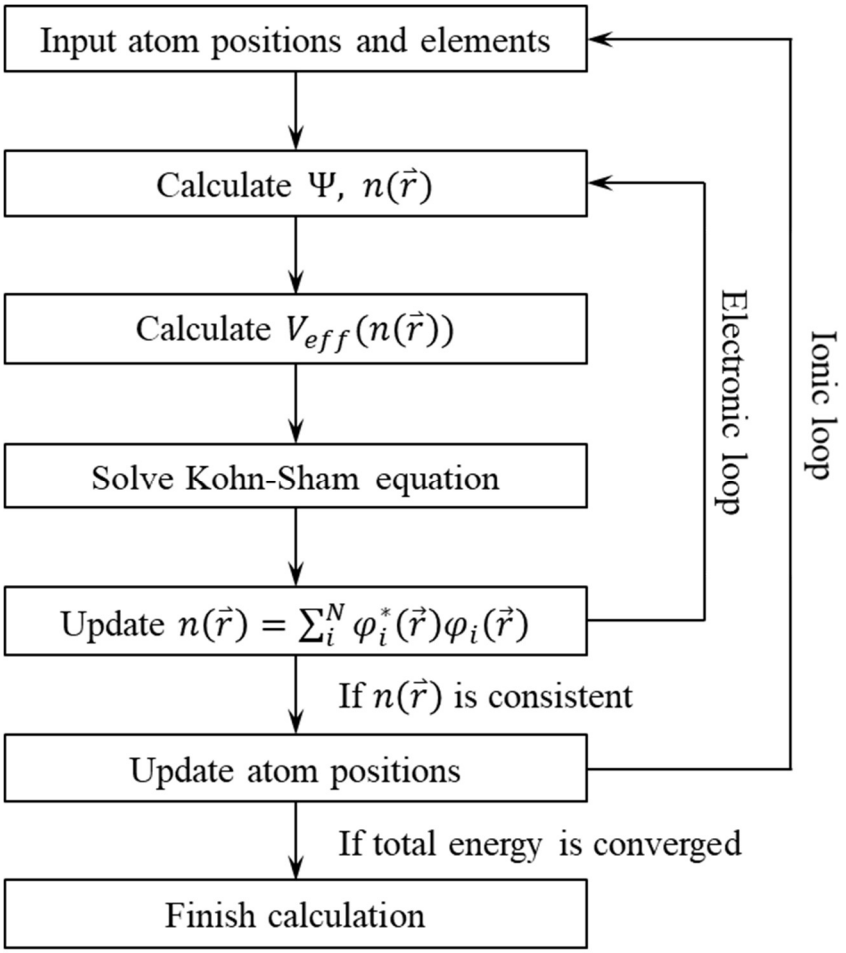

Figure 2.3: Schematic flow chart of DFT self-consistent iterations.

2.2.2. Exchange-correlation functionals in DFT

The major approximation in DFT comes from the treatment of exchange-correlation functionals, of which the exact form in unknow except for the homogeneous electron gas. Historically, the first approximate exchange-correlation functional is the local density approximation (LDA), which solely depends on the electron density at each point in space. In LDA, the exchange-correlation energy at each point is calculated by the homogeneous electron gas of the same density.

Then LDA was improved by incorporating the gradient of the electron density and evolved to generalized gradient approximation (GGA).[58], [59] Since then, GGA has been successfully predicting accurate results for many structural and energetic properties of not only bulk materials but also surfaces, defects and impurities.[60], [61] However, GGA fails to predict the band gap of transition metal oxides. In such systems, d electrons are strongly correlated, while from GGA calculations *d* states are overextended, and *p*-*d* repulsion then pushes the valence band maximum (VBM) upward and closer to the conduction band minimum (CBM), resulting in underestimated band gap.[62] For instance, the experimental band gap of ZnO is 3.4 eV, but GGA calculated value is only 0.7 eV.[63]

One of the corrections to address the band gap problem is DFT+*U* scheme. In such scheme, an orbital-dependent Coulomb repulsion *U* is applied to the semicore *d* states to enhance their localization.[64] But the band gap is yet fully corrected, and it also introduces uncertainty in the choice of the *U* parameter. And although sometimes correct band gap can be obtained by tuning the *U* parameter, other properties may behave unphysically.

In studies where highly accurate electronic structure is desired, hybrid functionals can be implemented. One of the popular hybrid functionals is HSE, named after its developers Heyd, Scuseria, and Ernzerhof.[65] HSE mixes a fraction of screened exact exchange into regular GGA exchange-correlation functional.[58], [59] With the aid of hybrid functionals, DFT predicted electronic structure is significantly improved,[66]–[68] but they are also much more computationally demanding.

2.2.3. Work function calculations

From the aforementioned definition, the work function is a surface property and is the energy difference between vacuum energy level and Fermi level. Therefore, the first step to

calculate the work function using DFT is to cleave the bulk material along a specific crystal plane, the termination of interest is thus exposed and a vacuum region is introduced into the supercell. With periodic boundary condition, such supercell is repeated three-dimensionally to form material slabs separated by vacuum regions, as shown schematically in Figure 2.4(a). By solving the Kohn-Sham equations of the above system, the electronic structure can be determined. Further with the knowledge on the amount of electrons in the system, the Fermi level can be easily obtained from Pauli exclusion principle and Fermi-Dirac distribution.[69], [70] In commercialized DFT simulation packages (for instance, the Vienna Ab Initio Simulation Package (VASP)[71]), the Fermi level is usually directly given in output files. Solving Kohn-Sham equations also gives the electron density, which can be used to calculate the electrostatic potential of each point in space in the system. Next, by averaging the electrostatic potential of xy-plane, the plane-average electrostatic potential along z direction which is normal to the surface can be obtained and be used to determine the vacuum energy level, as shown in Figure 2.4(b). So far, we have both the Fermi level and the vacuum level, and the work function is simply their energy difference.

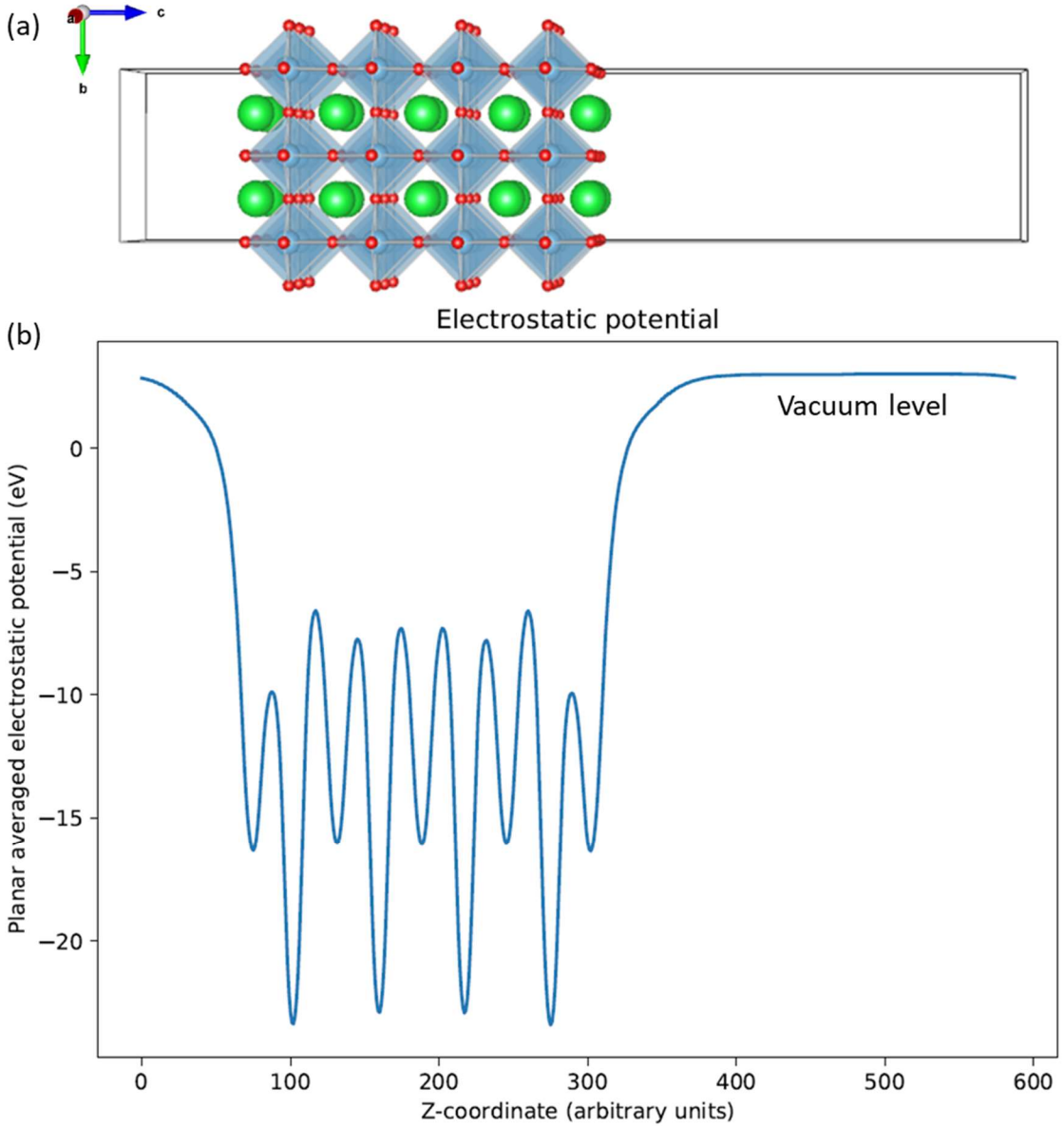

Figure 2.4: (a) Schematic surface slab model used in DFT calculations to obtain the work function of the exposing termination. (b) Electrostatic potential from the surface calculation, where the vacuum level can be determined.

Due to quantum-size effects, the Fermi level derived from slab calculation might be inaccurate. Fall *et al.* proposed a technique utilizing macroscopic electrostatic potential to reduce such effects and help with the convergence.[72] The idea is to use macroscopic average electrostatic potential from bulk calculation, where no quantum-size effects are involved, as a

reference. Comparing the average electrostatic potential in the slab to the bulk reference would give an energy difference representing the quantum-size effects on the electronic energy, applying this energy difference as a correction yields accurate Fermi level for slab calculation, and thus accurate work function. A simpler way to reach the same accuracy is to use thick enough slabs to ensure a bulk-like region in the middle, and hence the Fermi level of the slab is converged to that of the corresponding bulk. We use the latter method in our calculations and the deviation between bulk and slab Fermi levels is smaller than 0.05 eV.

2.2.4. Accuracy of DFT calculated work functions

DFT has been used to calculate the work function of pure elements[73], [74], metal hexaborides[75], [76], transition metal carbides, oxides[37], [77]–[79], and 2D materials like doped or surface decorated graphene[80], [81]. Some recent studies have benchmarked the accuracy of DFT calculated work function for elemental crystals: De Waele *et al.*[73] compared experimental work function values of poly-crystalline elemental materials to the lowest DFT calculated value among different surfaces, and found both LDA and GGA yield accurate work functions with mean absolute error (MAE) below 0.3 eV; Tran *et al.*[74] proposed a weighted DFT-GGA work function based on the Wulff shape and compared well with experimental polycrystalline data with MAE around 0.2 eV. In addition, more targeted DFT studies of tungsten with various surface orientations and adsorbate types by Vlahos *et al.*[11], Jacobs *et al.*[34] and Zhou *et al.*[33] demonstrated qualitative agreement between calculated DFT work functions and experimentally derived work functions from thermionic emission experiments. For compound materials, Uijttewaal *et al.*[75] and Schmidt *et al.*[76] have demonstrated great agreement between DFT-GGA calculated work functions and experimental values for lanthanum hexaboride (LaB_6) on different surfaces. Analogous comparison is difficult for oxide systems as the work function of

this kind of materials is highly dependent on surface termination,[37], [78] and oxides also exhibit abundant surface reconstructions,[82]–[86] while experimental work function measurements often lack accompanying atomic-level surface characterization. Our recent work[87] performed a case study on $SrTiO_3$ whose work function and surface structure are both well-studied, and made careful comparison between DFT-HSE calculated work functions and experimental values of the same surface, the results will be discussed in detail in Chapter 4. In brief, a deviation of around 0.2 eV was concluded, which is at the same level of accuracy as elemental materials.

2.2.5. Computational methods

All calculations are performed with DFT using the VASP[71] software with either the GGA-PBE[59] functional or the HSE06[88] hybrid functional with 25% exact exchange and inverse screening length of 0.2 $Å^{-1}$. The cut-off energy for the plane-wave basis set is 500 eV. The convergence criterion of ionic steps is 10^{-3} eV per supercell energy change. All calculations are performed with spin polarization enabled. PBE-type pseudopotentials utilizing the projector augmented wave (PAW)[89] method are used for all atoms. For bulk calculations, hexaborides adopt a cell consisting of one formula unit containing 7 atoms for pure compounds, and an enlarged supercell consisting of eight unit cells containing 56 atoms ($2a_0 \times 2a_0 \times 2a_0$) for alloyed compounds to accommodate alloy components, with a Monkhorst-Pack[90] 12×12×12 *k*-point mesh and 6×6×6 *k*-point mesh, respectively. Tetraborides use a cell consisting of four formula units containing 20 atoms, with a Monkhorst-Pack 7×7×12 *k*-point mesh. TMNs use a supercell consisting of four formula units containing 8 atoms, with a Monkhorst-Pack 12×12×12 *k*-point mesh. Perovskites use a supercell consisting of eight formula units containing 40 atoms, with a Monkhorst-Pack 4×4×4 *k*-point mesh for GGA or GGA+*U* relaxations, or a 2×2×2 Monkhorst-Pack *k*-point mesh for HSE relaxations. For perovskites GGA+*U* simulations, the *U* values of V,

Cr, Mo, W, Mn, Fe, Co, Ni are 3.25 eV, 3.7 eV, 4.38 eV, 6.2 eV, 3.9 eV, 5.3 eV, 3.32 eV, and 6.2 eV,[91] respectively, and are chosen to maintain consistency with the Materials Project database, which is necessary for accurate thermodynamic stability calculations.[91] For perovskites HSE calculations, the fractions of exact exchange are obtained from previous studies.[37], [92], [93] In these previous studies, the fractions of exact exchange were chosen to reproduce the experimental bandgaps and densities of states, and were chosen in these previous studies as 0.25 ($LaScO_3$), 0.15 ($LaTiO_3$, $LaCrO_3$, $LaMnO_3$, $LaFeO_3$), 0.125 ($LaVO_3$), 0.05 ($LaCoO_3$), and 0 ($LaNiO_3$).[92], [93] For the materials $SrVO_3$, $CaNbO_3$, $SrNbO_3$, and pure and doped $BaNbO_3$, an exact exchange value of 0.125 is used because these V- and Nb-based compounds are in the same group of the periodic table and thus are expected to be chemically similar to $LaVO_3$, for which an exact exchange value of 0.125 was found to result in a good fit with experimental electronic structure data. For the band insulators and all other perovskites, a default value of 0.25 is used for the Hartree-Fock exchange fraction. For HSE calculations of doped perovskites, the fraction of exact exchange used is the same as the corresponding pure compound. While we do not know the precise optimal exact exchange value that should be used for each perovskite composition, select tests of the effect of the choice of the exact exchange fraction on the resulting work function for $PrHfO_3$ and $Ba_{0.5}La_{0.25}Rb_{0.25}NbO_3$ demonstrate that varying the exact exchange between 0.125 and 0.25 (the typical range of exact exchange fractions employed in HSE calculations) results in a change in work function on the order of 0.05 eV.

The structures of doped perovskites are obtained by replacing elements in the pure perovskites at concentrations ranging from 12.5% to 50% of the A- and/or B-sites. Following the previous study of Jacobs *et al.*, to keep the number of screening calculations of doped compounds tractable, we consider a single ordering for each doped compound, where the dopant atoms are

distributed as far from each other as possible on the appropriate perovskite sublattice (i.e. A- or B-sites). We have confirmed that different orderings have only minor effects on the O *p*-band center and energy above convex hull. A total of 2913 bulk perovskite materials are examined in chapter 5. Of these 2913 materials, 2514 materials are obtained from the work of Jacobs *et al.*, who used similar high-throughput DFT methods to search for stable, high activity perovskite oxides as solid oxide fuel cell cathodes.[94] The remaining 399 compounds are calculated in this dissertation following preliminary screening analysis which demonstrated that metallic perovskites with a low number of *d* electrons tend to exhibit the lowest work functions, thus making this space of materials promising for additional, focused exploration.

To obtain the work function, we perform symmetric slab calculations with a vacuum region at least 20 Å thick, and *k*-point meshes which are scaled from the bulk values above according to the dimensions of each slab supercell. Hexaboride slabs are $5a_0$ in thickness, tetraboride slabs are $4a_0$ in thickness. We study the (001) metal-terminated surface, with the top two layers of metal atoms and one layer of the boron cage allowed to relax. The (001) surface can be terminated by metal or B. The (001)-metal terminated surface is generally believed to be the lowest work function surface in hexaborides based on experimental observations of (001) surfaces and simple dipole arguments which imply that a metal vs. B termination will have lower work function.[95]–[99] While there is little information in the literature on observed tetraboride terminations, we assume the (001)-metal terminated surface is the most relevant and lowest work function based on the similarity between hexaborides and tetraborides. TMN slabs are $4a_0$ in thickness and top three layers are relaxed. We examine (001) and (111) surfaces of TMNs as they have been experimentally observed.[100], [101] Perovskite slabs are $4a_0$ in thickness with a cross-sectional area of $2a_0 \times 2a_0$. For some simulations of $SrTiO_3$ (STO), different surface slab sizes are needed in

order to represent a particular surface reconstruction, surface defect concentration or Nb doping concentration. These simulations use either a $4a_0 \times 2a_0$ or $4a_0 \times 4a_0$ cross-sectional area. In all cases, the top 3 surface layers are relaxed, as well as any defected or adsorbed surface atoms. Tests with more *k*-points and larger slabs suggest that work function errors associated with *k*-point sampling and finite slab thickness and layer relaxation are less than 0.1 eV. The surface vacancies and adsorbates are placed on the surface as far from each other as possible. For Nb-doped STO, Nb dopants are substituted for Ti in the middle of the slab to eliminate possible influence on the surface dipole and to mimic a bulk Nb-doped STO material. To keep the simulated cell size practical for the HSE-level simulations, the Nb dopant concentrations used in our simulations are x_{Nb} = 5 at% (6.25 at%) for TiO_2-terminated (SrO-terminated) surface, and are thus higher than typical experimental values of x_{Nb} = 1 at%.[102]–[106]

The work function can be expressed as $\Phi = E_{\mathrm{vac}} - E_{\mathrm{F}} = \Phi_0 + \Delta\Phi_{\mathrm{dipole}}$. Here E_{vac} is defined as the value of the converged electrostatic potential sufficiently far from the terminating surface of interest such that the restoring force on an emitted electron is negligible. E_{F} is the Fermi energy, Φ_0 is the intrinsic work function that would be observed for a surface with no dipole, and $\Delta\Phi_{\mathrm{dipole}}$ is the change of the work function resulting from the surface dipole. The relationship between surface dipole and $\Delta\Phi_{\mathrm{dipole}}$ is given by the Helmholtz equation.[107], [108] Since DFT simulations calculate ground state properties (T = 0 K), VASP-calculated Fermi level, $E_{\mathrm{F,VASP}}$, is always positioned at the energy of the highest occupied electronic state, which for a semiconductor like STO is the valence band maximum (VBM). For cases explored in this work where this occupancy is not correct for a given comparison or analysis, we perform a correction to shift $E_{\mathrm{F,VASP}}$ to the appropriate occupied state(s). Specifically, to compare our DFT-calculated work

functions of STO with experimental values of pure and n-type STO we shifted $E_{\mathrm{F,VASP}}$ from the VBM to the middle of the band gap (to mimic finite temperature behavior) and to the conduction band minimum (CBM), respectively. In other words, to model pure and n-type STO from a pure STO calculation we shift $E_{\mathrm{F,VASP}}$ by $E_{\mathrm{G}}/2$ and E_{G}, respectively.

Such corrections require accurate band gaps, and we have found that the use of HSE correctly reproduces the experimental band gap of 3.2 eV. In contrast, the use of GGA not only underestimates the magnitude of the band gap but places the VBM and CBM levels at different positions relative to the vacuum level, thus affecting the work function values obtained for GGA versus HSE. Note that we use band gaps from the slab calculations rather than bulk as we assume the former best represent the near-surface environment that controls the work function.

The O *p*-band center is the centroid of the oxygen-projected density of states, referenced to the Fermi level, and is defined as:

$$\bar{O}_{2p}(E) = \frac{\int_{-\infty}^{\infty} E \cdot D_{O_{2p}}(E)dE}{\int_{-\infty}^{\infty} D_{O_{2p}}(E)dE} - E_{\mathrm{Fermi}} \qquad 2.10$$

In Section 5.2.3 and Section 5.2.7, perovskite materials are analyzed by grouping materials based on the number of *d*-band electrons. The number of *d*-band electrons in a material is calculated using empirical electron counting rules and the assumption of completely ionic bonding. These assumptions result in alkali metals always regarded to be in the 1+ oxidation state, alkaline earth metals in the 2+ state, lanthanides in the 3+ state, oxygen in the 2- state, and the transition metals possessing an oxidation state or mix of oxidation states such that charge balance is realized. In the case of a material containing multiple species on the B-site, the number of *d*-band electrons for the material is taken as the average number of *d*-band electrons of the B-site species present.

For example, in the case of $SrVO_3$, V is in the 4+ oxidation state, so this is a $3d^1$ material, and the *d*-band occupation therefore equal to 1.

The stability of all materials is evaluated using the energy above the convex hull (E_{hull}). To calculate the E_{hull} values, we use the *GrandPotentialPhaseDiagram* class in the phase diagram module within the Pymatgen toolkit.[109] To mimic environmental conditions typical of a thermionic electron emission cathode, we calculated E_{hull} for an open system where the chemical potential of O was calculated to coincide with thermionic cathode operating conditions of T=1000 ˚C and $p(O_2) = 10^{-10}$ Torr. The chemical potential of O was calculated following the work of Jacobs *et al.*,[110] where the DFT-calculated O_2 molecule energy was shifted to account for the finite temperature gas enthalpy and entropy values at T = 1000 ˚C, as well as the ideal gas partial pressure shift to coincide with $p(O_2) = 10^{-10}$ Torr.[111] Finally, the DFT-PBE errors associated with O binding were handled using the Materials Project energy shift of -0.7023 eV/O,[91] and the vibrational entropy contribution was included using an Einstein model with an Einstein temperature of 500 K, following previous studies.[11], [111]

2.3. Review on lanthanum hexaboride (LaB_6) cathodes

Lanthanum hexaboride (LaB_6) adopts CsCl type structure, where octahedral boron cages locate at all corners and lanthanum locates at the body center. The boron cage framework is electron deficient and requires 2 electrons per unit formula to saturate,[112] with lanthanum providing 3 electrons to the system, the excess electron makes LaB_6 electrically conductive; and the strong covalent bonding in the boron framework grants LaB_6 a high melting temperature, both properties are favorable to thermionic emitters. Lafferty[113] tested the thermionic emission properties of polycrystalline CaB_6, SrB_6, BaB_6, LaB_6, CeB_6, ThB_6 in 1951 and found LaB_6 to be

the most promising with a low work function of 2.66 eV, as shown in Figure 2.5. Twenty years after Lafferty's discovery, Broers experimentally demonstrated that LaB_6 cathode could significantly improve the spatial resolution of electron micro-scopes.[114] That study aroused great interest towards LaB_6, and as the demand of LaB_6 for scientific instruments started to increase, single crystal LaB_6 was fabricated by floating-zone method and Al flux method to provide higher brightness and longer lifetime. The crystallographic dependence of LaB_6 work function was also investigated, and the (001) surface was found to possess the lowest work function among various surface orientations. [14], [75], [115] The superiority of (001) surface is believed to be the high La coverage providing a positive surface dipole.

Main disadvantages of LaB_6 are brittleness which makes them difficult to be fabricated into sophisticated configurations, and poor thermal shock resistance even in single crystal form. Attempts to improve LaB_6's mechanical and/or emission properties by alloying with rare-earth or transition metals have been unsuccessful. Studies on other hexaboride systems, including BaB_6, YB_6, CeB_6, PrB_6, NdB_6, SmB_6, EuB_6, and GdB_6, have not yielded better emission performance than LaB_6.[48], [49], [116]–[122]

More recent studies show that composites comprised of LaB_6 and transition metal diboride (LaB_6-MeB_2) have improved properties over regular LaB_6 cathodes.[12] LaB_6-MeB_2 system has a eutectic type of phase diagram, which results in stable phase compositions and thus stable physical properties. Several LaB_6-MeB_2 eutectic systems have been synthesized (Me=Ti, Zr, Hf, V, Ta, Cr) where needle-like MeB_2 second phase evenly distributed in a single crystal LaB_6 matrix. In such structure, MeB_2 second phase reinforces the composite and enhances both the mechanical strength and the thermal shock resistance. The emission current density is also improved for LaB_6-MeB_2 system, at 2000 K, the current density of LaB_6-VB_2 can reach 85.0 A/cm^2, whereas the current

density of LaB_6 is only 4.9 A/cm^2. By low energy electron microscopy (LEEM), the work function distribution of LaB_6-VB_2 is observed, and most of the low work function areas are concentrated at the boundaries between LaB_6 matrix and needle-like VB_2 second phase. The lowest work function is close to 1 eV.[123]

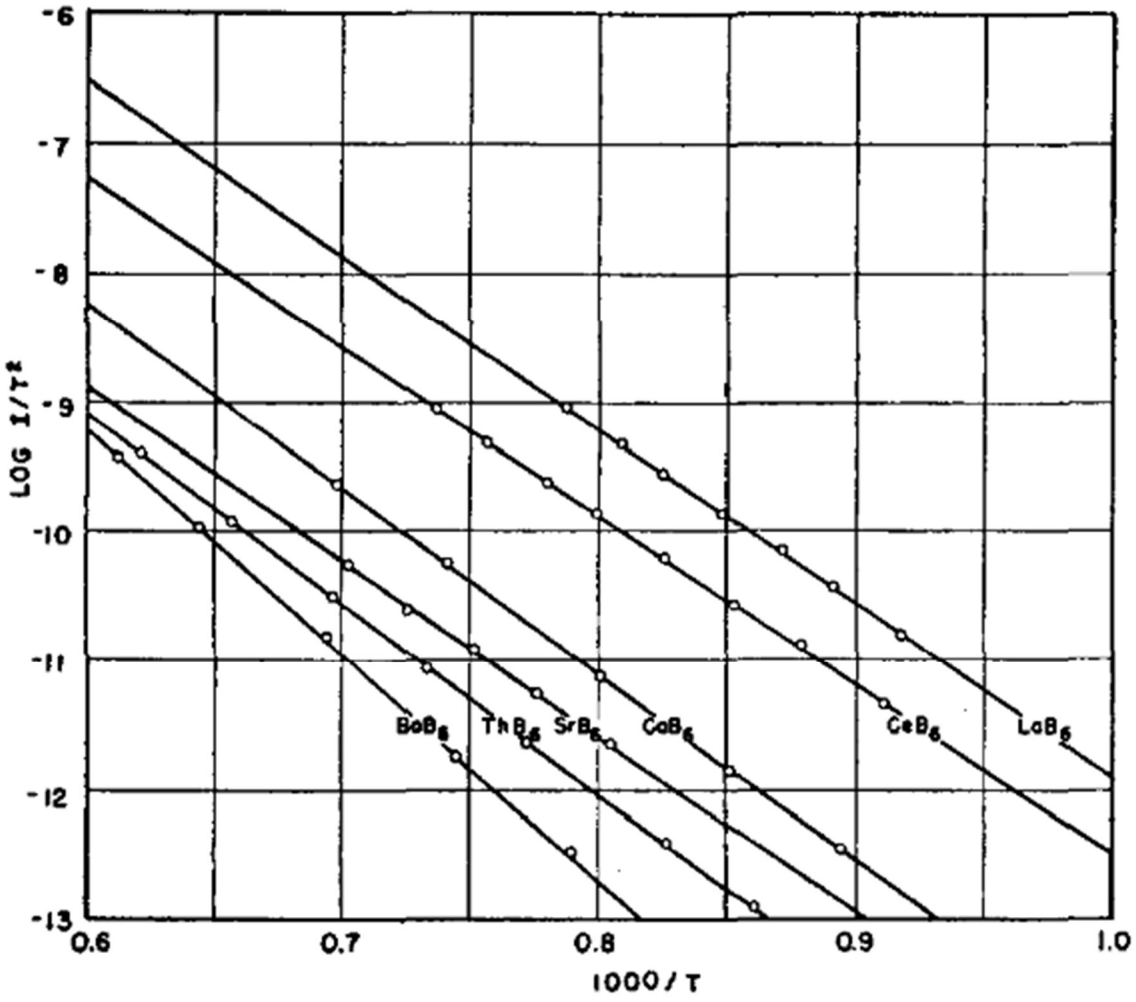

Figure 2.5: Richardson plots for the hexaborides investigated by Lafferty, from ref[113].

2.4. Review on dispenser cathodes

2.4.1. Development of dispenser cathodes

After W cathode, oxide cathode was discovered in 1904 by Wehnelt. Due to its poor electrical conductivity, oxide cathode can only produce low current density to avoid Joule heating. Dispenser cathodes were evolved from oxides cathodes under the demand of higher current density. L cathode, named after its inventor's last name, was the first dispenser cathode. This cathode consists of a porous W lid welded on a Ta cavity in which electron emissive material ($BaCO_3$) is filled. The Ta cavity was later substituted by a porous W matrix, and the electron emissive materials were impregnated into the W matrix, such are the impregnated cathodes. Impregnated cathodes are categorized as different types based on their electron emissive materials (i.e., impregnants): for A-type cathode, a mixture of $BaCO_3$ and Al_2O_3 is used as the impregnant; for B-type and S-type, mixtures of $BaCO_3$, $CaCO_3$ and Al_2O_3 at the molar ratio of 5:3:2 and 4:1:1 are used, respectively. A typical impregnated cathode design is shown in Figure 2.6. Under operating at high temperature, the impregnant is reduced by W and releases free Ba atoms, which diffuse to the cathode surface and react with oxygen to form a BaO monolayer lowering the work function. While the work function of pure W is ~4.5 eV, with the aid of the BaO dipole layer, the work function of impregnated cathodes can reach ~2 eV.

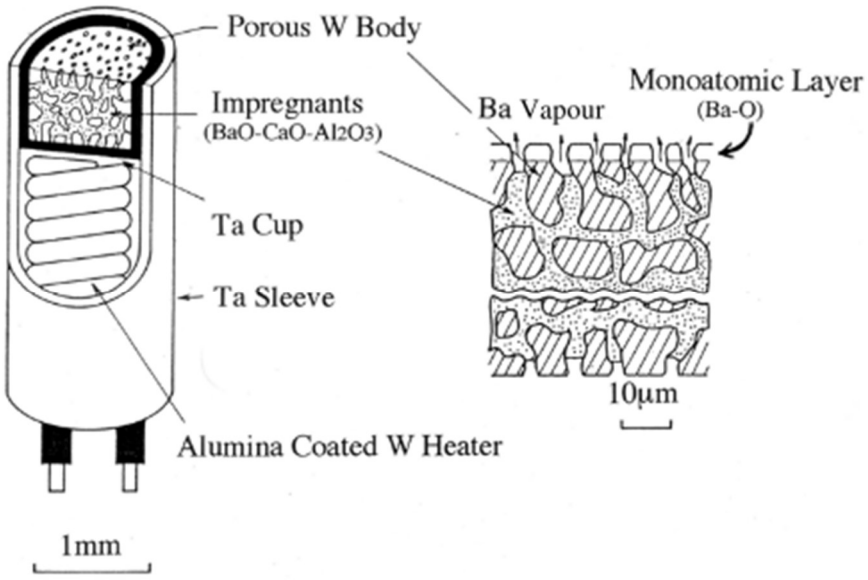

Figure 2.6: Schematic demonstration of typical impregnated cathode design from ref[8].

By depositing an Os thin film on a standard impregnated cathode, the work function was found to be further lowered by ~0.2 eV, and the work function uniformity was also improved.[8] Such Os coated cathode was able to operate 100 °C lower while maintaining the same current density as standard impregnated cathode, the revolutionary performance earned it the name 'Magic cathode', or 'M cathode'. Due to the toxicity of OsO_4, now an Os-Ru alloy is used as the surface coating.

During surface modification studies on the impregnated cathodes, Sc_2O_3 was found to significantly improve electron emission when added to the impregnant. This discovery encouraged the invention of scandate cathode, which is fabricated by either adding Sc_2O_3 into the impregnant or depositing a Sc_2O_3-containing thin film as top layer. Although the current density of scandates cathode can reach as high as 400 A/cm^2 at 1020 °C,[124] an emission model for scandate cathodes has not been well established, preventing further optimizations. And scandate cathodes also suffer from poor emission uniformity and short lifetime.[125], [126]

2.4.2. Surface structures of impregnated cathodes

The Ba-O monolayer model for impregnated cathodes originated from experimental studies done by Forman[127] and Haas *et al.*[128]. They prepared a W substrate with Ba-O monolayer and an activated impregnated cathode, then recorded and compared the Auger spectra of the two samples, and found that the Auger spectra from the activated cathode surface were identical to those obtained from the Ba-O monolayer on W substrate. Although the exact positions of surface Ba and O cannot be determined, they proposed that the Ba-O dimers occupy fourfold hollow sites in either an upright or a coplanar geometry.

Vlahos *et al.*[11] investigated the stability and the work function of different surface structures for impregnated cathodes using DFT calculations. It was found that a tilted Ba-O dimer configuration is thermodynamically more stable than the previously proposed models, and the corresponding work function is ~1.9 eV depending on the coverage. However, if off-stoichiometry was allowed, the $Ba_{0.25}O$ surface structure was found to be the most stable, which also possesses a significantly lower work function of 1.29 eV. Since experimentally measured work function for B-type cathodes is generally around 1.9 eV, this may suggest that a non-equilibrium steady state dominates the surface of activated B-type cathode. For Sc-containing surface structures, the most stable configuration was $Ba_{0.25}Sc_{0.25}O$, which can be regarded as a Sc-stabilized $Ba_{0.25}O$ structure. The work function of $Ba_{0.25}Sc_{0.25}O$ surface structure was calculated to be 1.16 eV, demonstrating good overall agreement with experimental results. These surface structures are shown in Figure 2.7.

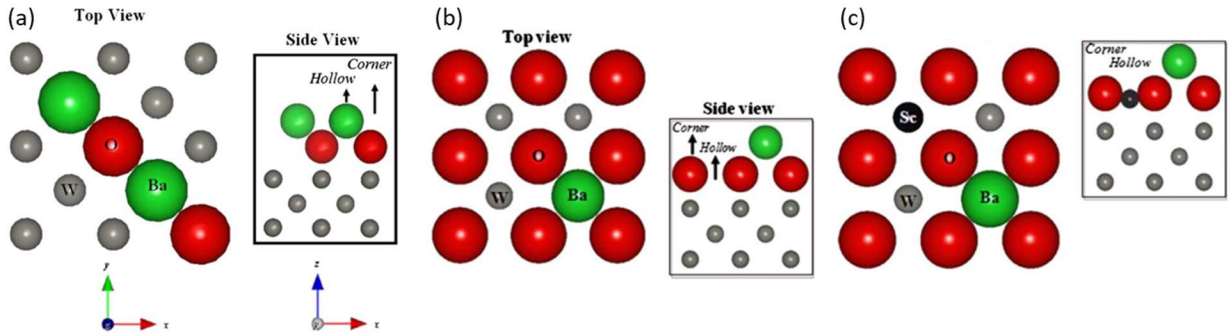

Figure 2.7: Top and side view of (a) tilted Ba-O dimer; (b) $Ba_{0.25}O$ surface; (c) $Ba_{0.25}Sc_{0.25}O$ surface (from ref[11]).

Zhou *et al.* also performed DFT studies on the $Ba_xSc_yO_z$ layer in scandate cathodes.[33] They explored a range of $Ba_xSc_yO_z$ layers on W (001), (110), and (112) surfaces, based on a previous experiment where a high-functioning scandate cathode consists of W grains exhibiting (001), (110), and (112) surfaces uniformly. Their results showed that the combination of $Ba_{0.50}O$-*top*/$W_{(001)}$, $Ba_{0.25}O$-*tri*/$W_{(110)}$, and $Ba_{0.50}O$-*top*/$W_{(112)}$ can reproduce the experimentally observed crystal shape, and such surface layers are stable at μ_O between -8.48 eV/at to -8.06 eV/at. Their results indicate that the role of Sc in scandate cathodes is to tune μ_O (note that there is no Sc in the stable surface layers) and the difficulties in manufacturing are probably due to the variability in the availability of O on the scandate cathode surface during activation and operation.

These Ba-containing surfaces are volatile, and thus limit the operating temperature of impregnated cathodes. For instance, the M cathode is the best commercial cathode which can produce a current density up to 5 A/cm^2 at 1020 °C for over 50,000 h. To produce higher current density (>10 A/cm^2), an elevated operating temperature of 1200 °C is required. However, the lifetime is reduced to 1,000 h due to accelerated Ba depletion at such high temperature.[9] For scandate cathodes, the surface has even more drawbacks: the emission surface cannot recover in

time under ion bombardment, resulting in emission degradation;[129] the work function distribution on scandate cathode surface is non-uniform, patches with high work function and patches with low work function coexist, creating significant patch field effect which suppresses the electron emission;[20], [130] and there are also problems in achieving sufficient lifetime and reproducible performance.[9]

3. Work function trends and new low work function boride and nitride materials

3.1. Introduction

Despite the success of LaB_6 as a commercial material, new monolithic electron emitters with lower work function are still desirable to further improve the performance of devices using electron emitters. Besides a low work function, monolithic materials that function as thermionic emitters need to have a high melting temperature (to facilitate high temperature stability) and high electrical conductivity (to facilitate adequate supply of electrons for emission). With these key properties in mind, there are additional interesting materials families beyond hexaborides that we explore in this work. These additional materials families consist of rare-earth tetraborides[131], [132] and transition metal nitrides (TMNs). We note here that transition metal carbides (TMCs) may also be interesting to explore, but previous computational studies on TMCs[77], [133] show work functions generally higher than 3 eV. Therefore, we do not perform further comprehensive studies on TMC work functions in our study.

Regarding rare earth tetraborides, some experimental studies on the thermionic emission properties of polycrystalline YB_4 and GdB_4 showed low work functions of 2.38 eV and 1.45 eV, respectively. However, these studies obtained the work function by fitting both the work function and Richardson constant in the RLD equation, where the resulting Richardson constants were quite small (0.1 and 10^{-3}, compared to the theoretical value of 120 $A \cdot cm^{-2} \cdot K^{-2}$) and only small current densities were observed, indicating they are likely inferior to LaB_6.[48] Despite these results indicating that YB_4 and GdB_4 are lower quality emitters than LaB_6, it is still possible that there exists a promising new cathode material among other tetraboride compositions. Regarding TMNs, these materials are also conductive and refractory,[134], [135] therefore, we further investigate

this class of materials to assess if any TMN materials have low work functions and are useful in electron emission applications. While previous computational studies showed that TMCs have work functions around 3 eV, to our knowledge there is no systematic study on TMNs. Qualitatively, we might expect TMNs to have lower work functions than TMCs because the Fermi level is elevated by doping of an extra electron from nitrogen compared to carbon. While some experimental measurements on TMN work functions did not yield low work functions,[100], [101] such experiments were carried out on TMNs with mixed (001) and (111) surfaces. Electron emitters with highly heterogeneous or patchy emitting surfaces may result in a measured work function higher than the desired low work function surface, so isolation of single (001) or (111) terminated TMNs may yield low work functions if either of these surfaces possesses a low work function.

As one of the main electron emitters used in numerous commercial applications, LaB_6 has remained essentially unchanged for decades. Despite the large number of studies on hexaboride emitters, they are often limited to one or a few hexaborides, and different studies adopt different sample preparation conditions and/or measurement methods. These differences can make one-to-one comparison of results difficult, and make chemical trends or effects of different surfaces challenging to discern. Importantly, to our knowledge there is no study which comprehensively evaluates and provides understanding of work function trends of the set of hexaboride, tetraboride, and TMN materials that are likely to form. Such a study would reveal trends of material composition with work function and enable understanding of coupling between composition, structure and work function. Knowledge of materials trends and understanding of the relationship between composition, structure and work function may suggest possible avenues toward designing new conductive, refractory, boride and nitride materials with lower work function than LaB_6.

In this chapter, we have conducted DFT simulations on the full rare earth series of pure hexaborides, along with select alkaline earth hexaborides and alloyed hexaborides. In addition, we have performed DFT simulations on all rare-earth tetraborides. Although Eu does not form EuB_4 due to its preference for divalent configuration[132], we still included it in our simulations for completeness and to help observe trends with composition. Finally, we have performed DFT simulations on a series of (001)- and (111)-surfaces of TMNs. From our results, LaB_6 has a work function of 2.01 eV, which is the lowest among all pure rare-earth hexaborides, and we find that the $La_{0.25}Ba_{0.75}B_6$ alloy has an even lower work function of 1.84 eV. In addition, we find the work function of tetraborides has a similar trend as that of hexaborides, but the work function of each tetraboride is higher than its hexaboride analogue, and thus tetraborides are likely less interesting for low work function electron emission applications. For TMNs, we find the relationship between the work functions of different surfaces or different transition metals is generally consistent with that in TMCs from previous studies. We also find that the (001) surface of HfN has a low work function of 2.16 eV and thus may also be an interesting material to further explore for possible emission applications.

3.2. Results and discussion

3.2.1. Review of hexaboride studies

Since its discovery in 1951, many experimental and computational studies have been performed on rare earth hexaborides, especially LaB_6, to study their work functions.[14], [15], [140]–[149], [16], [17], [115], [122], [136]–[139] Here, we review the available data from experimental studies from 1951 to present which aimed to measure LaB6 work function, as shown below in Figure 3.2.

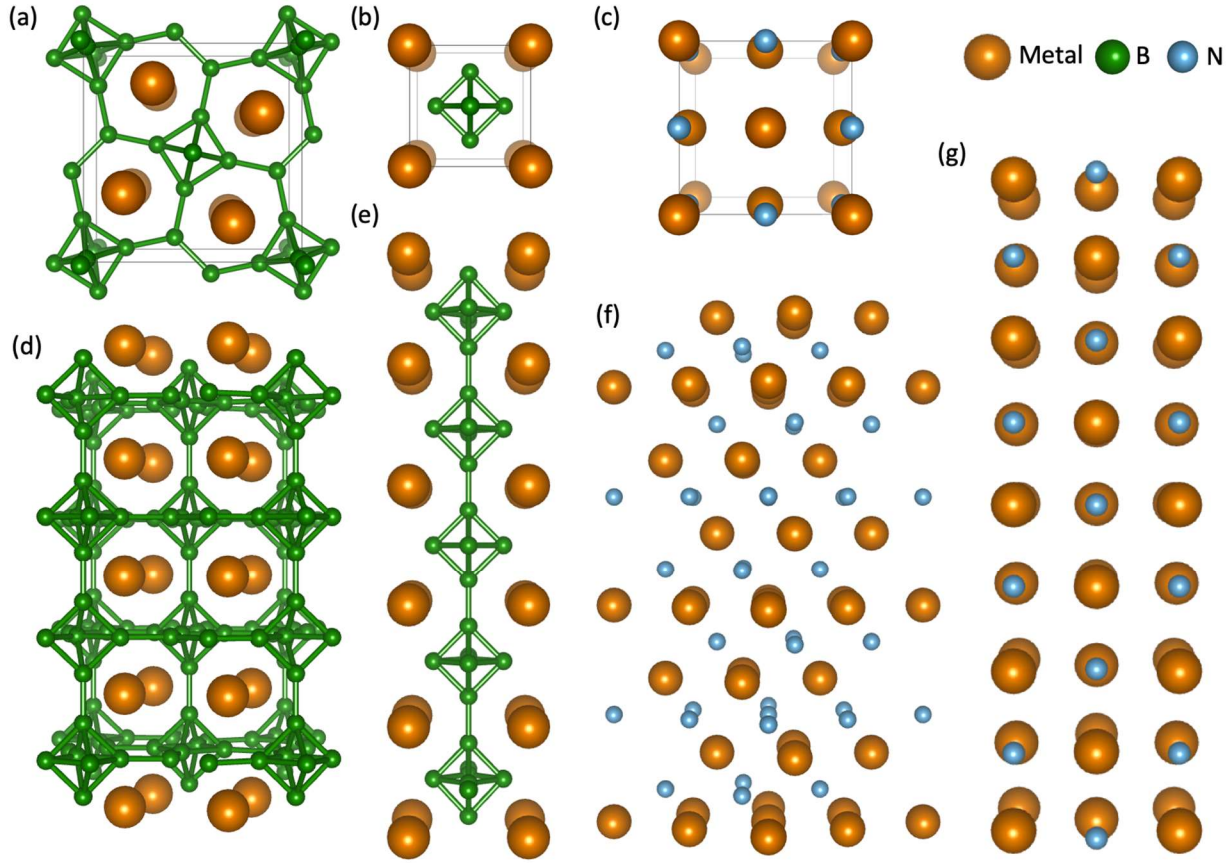

Figure 3.1: Supercells of bulk and slab hexaboride, tetraboride, and transition metal nitride used in our calculations. Bulk tetraboride, hexaboride, and TMN are shown in (a), (b), (c), respectively; (d) (001)-metal terminated tetraboride; (e) (001)-metal terminated hexaboride; (f) (111)-metal terminated TMN; (g) (001) terminated TMN.

In Figure 3.2(a) we summarize work function data which originate from different sample morphologies: polycrystalline LaB6 and (001) surface of single crystalline LaB6; and different measurement techniques: thermionic emission (denoted as TE), photoelectron emission (PE), or field emission (FE). In Figure 3.2(b), we condense the data from Figure 3.2(a) to provide averages and ranges of the work function data from different measurement methods. For thermionic emission, both polycrystal and single crystal averages are around 2.6 eV, although polycrystalline work functions seem to be more scattered, with a 0.8 eV range. This observed larger range for

polycrystalline work functions is mainly caused by a single work function measurement of 1.98 eV measured by Zhou *et al.*[147], which is notably lower than other measurements. In the study from Zhou *et al.*, the authors fitted both the Richardson constant A and the work function in the RLD equation, resulting in a small $A = 1.24\ \mathrm{A \cdot cm^{-2} \cdot K^{-2}}$. The authors performed another fit using the theoretical $A = 120\ \mathrm{A \cdot cm^{-2} \cdot K^{-2}}$, and the corresponding work function was 2.69 eV, very close to the average reported thermionic work function shown in Figure 3.2(b). We therefore believe that the very low A and work function values from Zhou *et al.* are a result of uncertainty in the fitting and a strong coupling between these two variables which can occur during fitting, leading to both values being quite far off and yet fitting well to physical emission data. We believe that Zhou *et al.*'s work function obtained from their fit with the theoretical A value is likely more accurate. In Figure 3.2(b), the average work function values from multiple studies are in very good agreement between thermionic emission of polycrystals, thermionic emission of single crystals, and field emission measurements, all of which give an average value of about 2.6 eV. The photoelectron emission measured averaged work function at 2.3 eV is generally lower than the work functions from other measurements, but the range of reported values overlaps with the range of values from both thermionic and field emission measurements, again indicating overall good agreement with other experiments.

In addition to the experimental LaB_6 work function data, there are also computational studies on LaB_6 predicting work functions of 2.07 eV[75] and 2.27 eV[76]. Given the observed spread in the experimental data, it is difficult to make one-to-one comparisons between calculation and experiment, however the computational results are generally lower than the experimental results. The origin of this discrepancy is not clear but discussed further in Sec. 3.3.2. LaB_6 surfaces other than the (001) surface have also been studied. While one study showed the (011) surface has

an even lower work function (2.68 eV) than (001) surface (2.86 eV),[142] there is historically more evidence both from experiments and computations to suggest that the (001) surface has the lowest work function.[14], [75], [115] There are also studies on other hexaboride compositions, including BaB_6, YB_6, CeB_6, PrB_6, NdB_6, SmB_6, EuB_6, and GdB_6, and their alloys with rare-earth or transition metals in search of better emitters.[48], [49], [116]–[122] However, none of them achieved higher current density than LaB_6.

3.2.2. Hexaboride work function trends and effects of alloying

The work functions of (001)-metal-terminated rare earth hexaborides from our calculations are shown in Figure 3.3, along with experimental work function values for each material, where available. For the most studied hexaboride, LaB_6, our DFT-calculated work function is generally lower than experimentally measured values, and the work function of LaB_6 from our calculation (2.01 eV) is consistent with previous computational studies, which found values of 2.07 eV[75] and 2.27 eV[76]. The observed discrepancy between calculated and experimental LaB_6 work function may be caused by factors related to measurement method or method of data analysis (e.g. fitting work function or work function and Richardson constant in thermionic emission experiments), or materials-related factors such as different stoichiometries, defect concentrations, and surface conditions determined by sample preparation. In addition, it is possible that errors in DFT play a role, as previous studies benchmarking the accuracy of DFT calculated work functions suggest DFT-GGA level work functions are ~0.3 eV lower than experimental values for metals,[73], [74] and a separate study of DFT-HSE level work functions have a ~0.2 eV deviation on average from experiments for $SrTiO_3$.[87] With this combination of factors, it is difficult here to judge whether DFT or experimental measurement is more accurate, or to fully understand the origin of the observed discrepancies between the calculated and experimental work functions in

Figure 3.3. Nevertheless, it is apparent that the trend of work function with composition is qualitatively the same between experiment and DFT. Therefore, we believe that the agreement between experiments and DFT is close enough that DFT guidance on trends is likely to be relevant for the performance of real materials.

In Figure 3.3, we also plot the average experimental values for each composition for which data was available. We find that the average (standard deviation) shift between our DFT calculated work functions and the experimental values is 1.11 (0.45) eV, mainly due to the large spread in experimental data for less-studied materials, particularly NdB_6 and EuB_6. If we restrict our comparison between DFT and experiment to the most studied hexaborides (i.e. LaB_6, CeB_6, PrB_6, and SmB_6), the deviation between DFT and experiment is 0.88 eV on average, and is 0.65 eV on average if one considers the most recent measurement of SmB_6 by Waldhauser *et al.*[122] to be the most reliable. In this latter comparison, the average error between DFT and experiment of 0.65 eV is reasonably uniform across the compositions considered, providing an approximate average error between DFT and experiment for the most-studied hexaboride materials. Again we note that although our calculated work functions appear to be lower than experiments, the accuracy of the trends suggests that a new material may still be a promising emitter if our calculations yield a work function lower than our calculated value for LaB_6.

From our calculations, LaB_6 has the lowest work function among all pure rare-earth hexaborides, and the work function increases as the parent rare-earth metal moves from the left to the right on the periodic table. These results can be rationalized by assuming the work function value is being governed by the electronegativity of the parent metal, which increases when proceeding from left to right on the periodic table. Parent metals that are less electronegative (i.e. more electropositive) will bind electrons less strongly, possibly resulting in both weaker overall

binding of electrons in the bulk of the material and a stronger positive surface dipole which acts to produce a low work function (recall the (001) surface of hexaborides is a layer of metal atoms, which will be positively charged). This observed trend also makes sense as a positive correlation between work function and electronegativity has been reported and validated for elements[150] and binary compounds[151]. Therefore, according to our results, it makes sense that LaB_6 has the lowest work function among all pure rare-earth hexaborides.

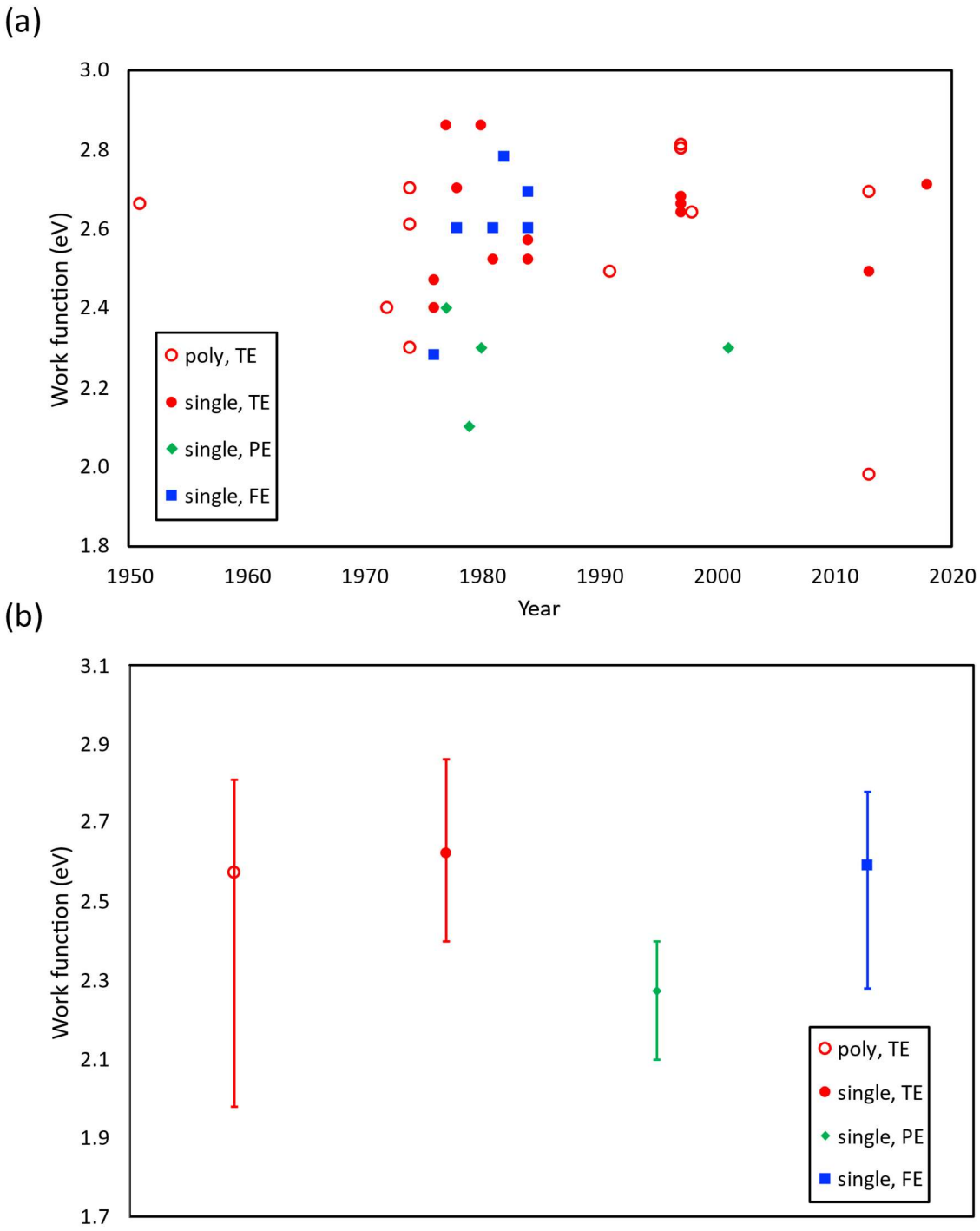

Figure 3.2: Experimental work functions of LaB_6 from different studies.[14], [15], [140]–[149], [16], [17], [115], [122], [136]–[139] (a) TE denotes thermionic emission, PE denotes photoelectron emission, and FE denotes field emission. Measurements on single crystals are all from (001) surface. (b) Error bars denote the ranges of the work function data, derived from taking the difference between the maximum and minimum values measured in experiments.

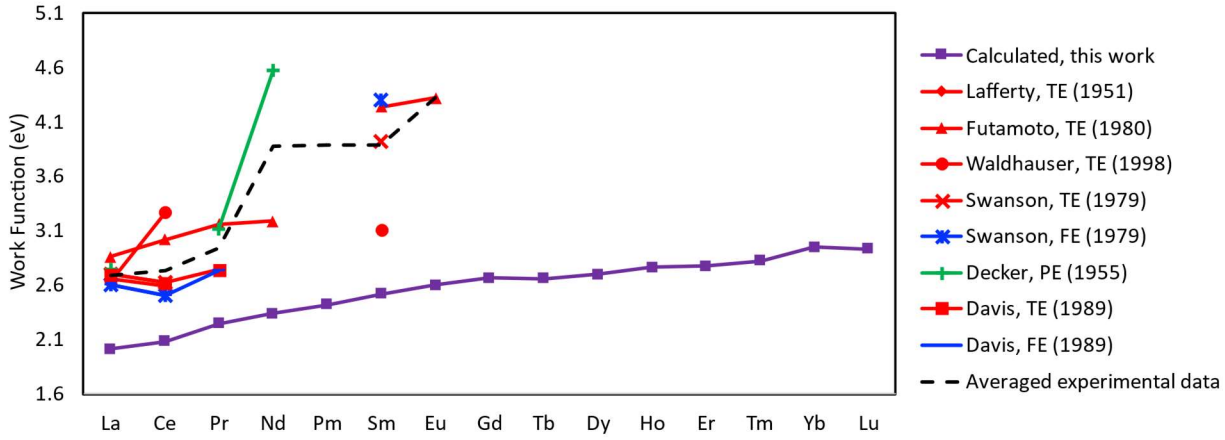

Figure 3.3: DFT-calculated work functions of hexaborides, comparing to experimental work functions. Thermionic emission data are in red, photoelectron emission data are in green, field emission data are in blue, and averaged experimental data are denoted as black dashed line.

There have also been experimental studies that attempted to alloy LaB_6 with other rare-earth or transition metals, but most such experiments of alloyed hexaborides did not yield higher current density than LaB_6. From our electronegativity arguments made above, it would seem plausible that hexaboride alloys incorporating some fraction of alkaline earth metal, as opposed to other rare earth or transition metals, may yield a lower work function and thus result in higher emitted current densities than the parent rare earth hexaboride. To test this hypothesis, we choose to alloy Ba into LaB_6, as Ba is the most electropositive stable alkaline earth metal, and calculate the work functions of a series of $La_xBa_{1-x}B_6$ alloys.

We consider seven different $La_xBa_{1-x}B_6$ alloys (x = 0.125, 0.25, 0.375, 0.6, 0.625, 0.75 and 0.875). The structures of the slabs of these compounds are shown in Figure 3.4, where $La_{0.125}Ba_{0.875}B_6$ and $La_{0.875}Ba_{0.125}B_6$ have two possible terminations, both of which are included in our calculations. The calculated work functions of these $La_xBa_{1-x}B_6$ alloys are shown in Figure 3.5. As we hypothesized, most of these alloys have work functions lower than pure LaB_6, where $La_{0.25}Ba_{0.75}B_6$ has the lowest work function of 1.84 eV, which is about 0.2 eV lower than pure

LaB_6. From examining the relaxed surface structure, we find that the lower work function from Ba alloying can be attributed to the different surface relaxation comparing to pure LaB_6 or BaB_6. As shown in Figure 3.4, due to the misfit between La and Ba atomic radii, the $La_{0.25}Ba_{0.75}B_6$ surface has more rumpling, with Ba atoms protruding outward, forming a larger surface dipole that facilitates electron emission. If one were relying on the argument of metal electronegativity alone, this would suggest that BaB_6 should have the lowest work function. However, we find that pure BaB_6 does not have a lower work function than the $La_xBa_{1-x}B_6$ alloys. This fact indicates that relying on metal electronegativity alone is not sufficient to understand the work function of hexaborides, where, for alloyed cases, the size mismatch between the alloyed metal atoms also plays an important role.

In addition to the work function of alloyed hexaborides, we examine a basic measure of alloy stability by calculating the mixing energies of alloying LaB_6 and BaB_6:

$$x\mathrm{LaB_6} + (1-x)\mathrm{BaB_6} \rightarrow \mathrm{La_xBa_{1-x}B_6} \qquad 3.1$$

Based on our calculations, the mixing energies of various concentrations of $La_xBa_{1-x}B_6$ are all quite close to zero, and slightly negative for the La range of 12.5-50%, which is the range of lowest alloy work functions. We speculate the mixing energies are near zero or weakly negative because the metal atoms are isolated from each other by the large boron frames, and thus have little interaction between them. If one further considers the effect of the mixing entropy, these results predicts it should be possible to experimentally synthesize such alloys, consistent with the results of Hasan *et al.*[49] who successfully synthesized a series of $La_xBa_{1-x}B_6$ at different concentrations, some of which formed stable alloys.

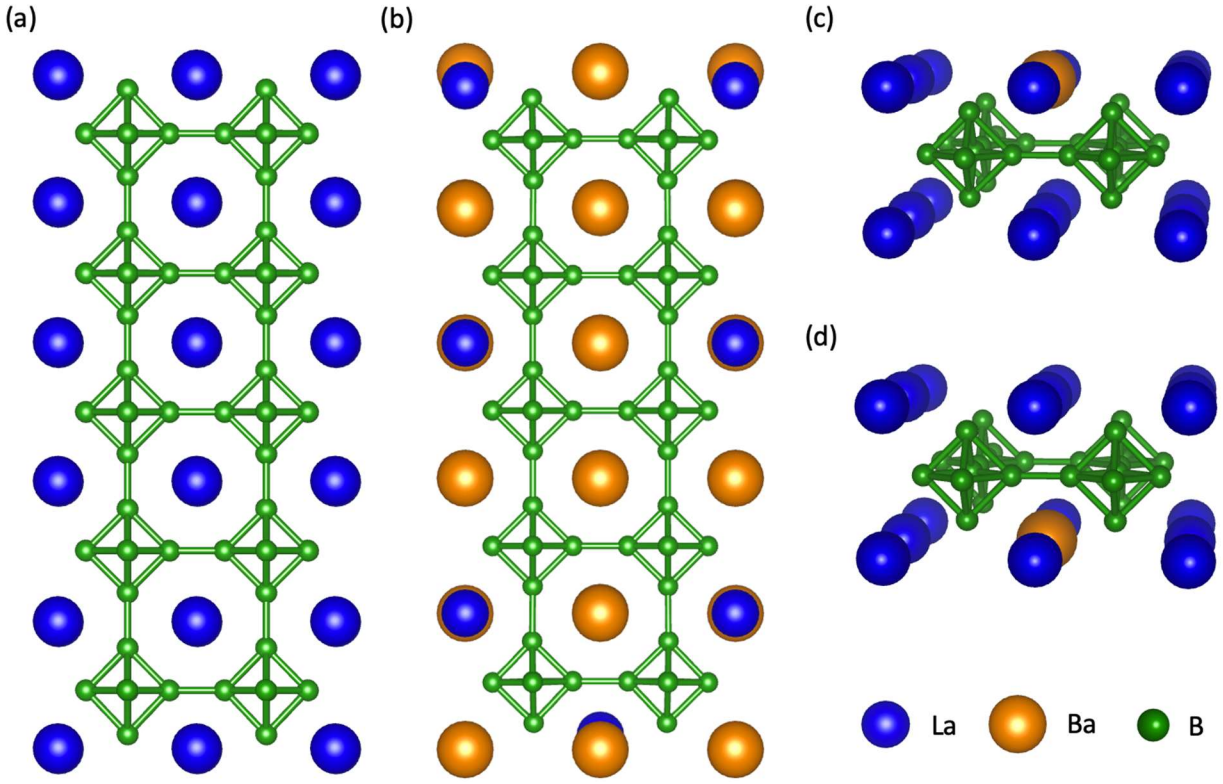

Figure 3.4: Relaxed structures of LaB_6 and $La_{0.25}Ba_{0.75}B_6$ slabs, and $La_{0.875}Ba_{0.125}B_6$ surfaces showing two possible configurations. (a) relaxed LaB_6 slab; (b) relaxed $La_{0.25}Ba_{0.75}B_6$ slab exhibiting surface rumpling; top three layers of $La_{0.875}Ba_{0.125}B_6$ slabs with (c) Ba rich termination, and (d) La rich termination.

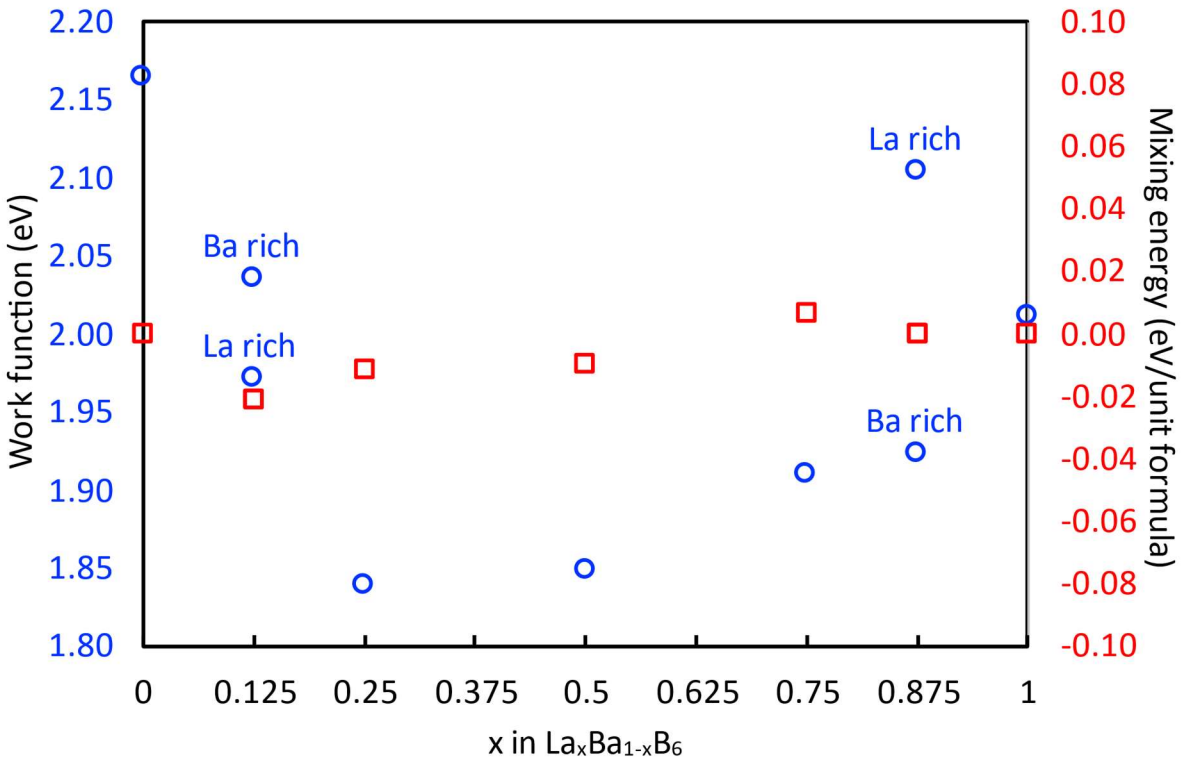

Figure 3.5: Work functions and mixing energies of $La_xBa_{1-x}B_6$.

Hasan *et al.* measured their lowest work function for $La_{0.31}Ba_{0.69}B_6$, very close in composition to the lowest work function we found, which was for $La_{0.25}Ba_{0.75}B_6$. Hasan *et al.* found the work function of $La_{0.31}Ba_{0.69}B_6$ to be 1.03 eV, accompanied with an extremely low Richardson constant of $A = 8.44\times10^{-6}$ A·cm^{-2}·K^{-2}. If the theoretical $A = 120$ A·cm^{-2}·K^{-2} was assumed, the work function would become ~3 eV. This result makes sense, considering the emission current density at $T = 1534$ K was ~10^{-2} A/cm^2, compared to ~0.2 A/cm^2 for pure LaB_6 at the same temperature from ref[113]. From these results, it appears at first glance that alloying LaB_6 with Ba results in a higher work function. However, the hexaboride material that underwent thermionic emission test in the work of Hasan *et al.* was actually a composite mixture of polycrystalline $La_{0.31}Ba_{0.69}B_6$, LaB_6, and BaB_6. The emitter surface is thus a heterogeneous mixture

of different materials which may result in domains of quite different work functions and associated patch field effects. These patch field effects are electric field interactions between low and high work function domains, and result in suppression of emission from the low work function surfaces, leading to an extracted thermionic work function that is higher than the work function of the most emissive, low work function material.[152] The very low Richardson constant for this composite material supports the fact that this emitter is highly heterogeneous, with limited surface area that was actively emitting. While these experiments do not demonstrate that $La_xBa_{1-x}B_6$ has a lower work function than LaB_6 or BaB_6, it also does not strongly suggest that it has a higher work function than these pure hexaborides, and thus may be consistent with our computational predictions. It is also possible that there is significant surface segregation in these materials, which we have not explored in the DFT studies. Overall, these experiments support the feasibility of $La_xBa_{1-x}B_6$ synthesis, and our present DFT results suggest that additional study with both DFT and experiments would be reasonable to assess if a low work function can be obtained with this alloyed material.

3.2.3. Tetraboride work function trends, comparison with hexaborides

Rare-earth tetraborides have similar crystal structure to hexaborides, where both contain rare-earth metals separated by large boron (B_6) octahedral cages. For tetraborides, there are also boron dimers linking the boron cages, resulting in a different boron structural framework than hexaborides, as shown in Figure 3.1. Following the same procedure as in hexaborides, we study the composition trends of work functions of (001)-metal terminated tetraborides. Like the case of hexaborides, this metal terminated surface is expected to have the lowest work function compared to B termination as it has a positive dipole pointing out of the surface. Our DFT-calculated work functions of rare-earth tetraborides are shown in Figure 3.6, and, for ease of comparison,

hexaboride work functions are also provided. Like the trend of hexaborides with composition, for tetraborides the work function tends to increase when progressing from left to right on the periodic table. This trend can again be understood in terms of metal electronegativity trends. Compared to the hexaboride trend, the changes in work function for tetraborides across the periodic table are smaller, and largely flat for Eu through Lu. The most striking difference between the hexaboride and tetraboride work functions is that the tetraboride values are higher for all compositions. From our analysis, in tetraborides we find the bonding between metal and boron to be less ionic than in hexaborides, i.e. fewer electrons are transferred from metal to boron. This lower ionicity for tetraborides makes the magnitude of the surface dipole smaller (i.e. less positive), resulting in a higher work function for tetraboride materials compared to hexaboride materials. Although Kudintseva *et al.* reported low work functions for YB_4 and GdB_4, the small reported Richardson constants and the fact that these materials showed lower current densities than their hexaboride counterparts[48] at the same temperature indicate that hexaborides are likely better electron emitters. In view of this, rare earth tetraborides are unlikely to be promising candidates for low work function electron emission cathode materials.

3.2.4. Transition metal nitride work function trends, effect of surface termination

Similar to hexaborides and tetraborides, transition metal nitrides (TMNs) and transition metal carbides (TMCs) show combined properties of high melting temperature (i.e. they are refractory) and high electrical conductivity, which make them potential candidates for electron emission materials. Since experimental studies and chemical intuition suggest that TMNs possess lower work function than TMCs, here we focus on further evaluating the work function trends only for TMNs.[153]

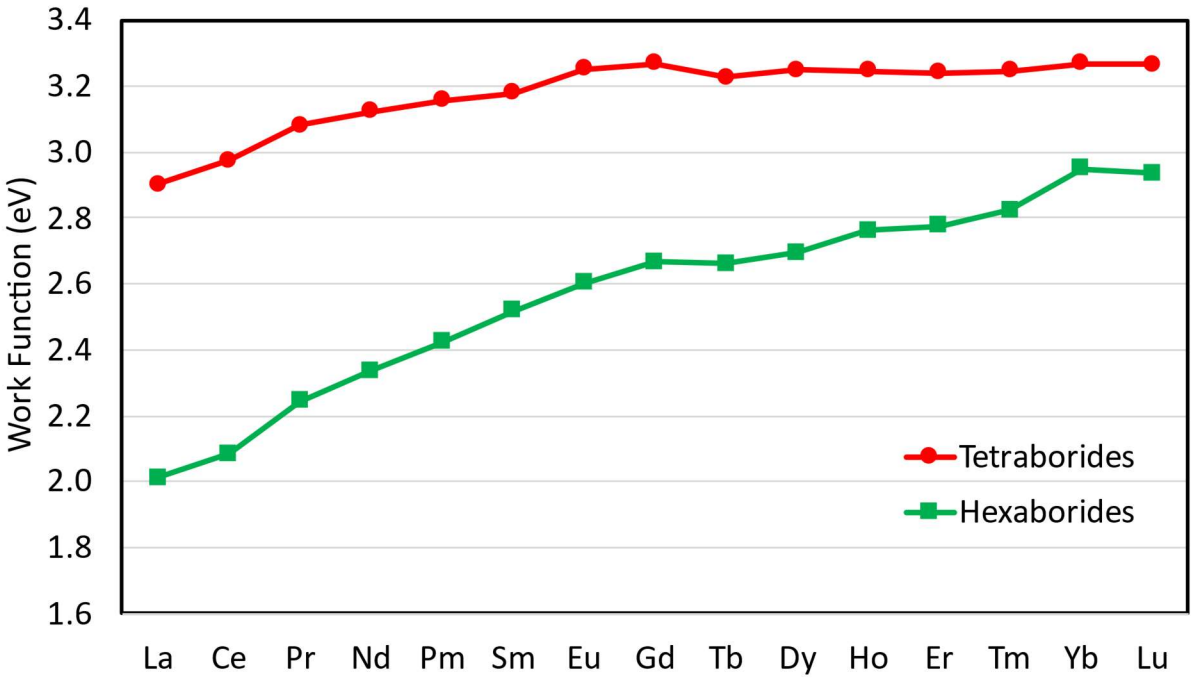

Figure 3.6: The work functions of rare-earth tetraborides, for comparison, the work functions of hexaborides are also provided.

We consider two low-index surfaces, (001) and (111), which are experimentally known to be stable at room temperature and over 500 °C.[100], [101] For the (111) surface, it is possible to have surfaces terminated by either all metal atoms or nitrogen atoms, as shown in Figure 3.1. Previous computational studies suggest substantial amount of charge transfer from metal to nitrogen.[154] Considering surface dipole effects, we expect the metal terminated (111) surface to have lower work function. Calculations on select TMNs confirmed that the metal terminated (111) surface indeed has a lower work function than the nitrogen termination, therefore, we focus on metal terminated (111) surfaces and (001) surfaces for evaluating work function trends of TMNs.

In Figure 3.7(a) we show our calculated work functions of TMNs from Sc to Ni, for both (001) and (111)-metal terminations. For all TMNs in our calculations, we find that the (001) surface has lower work functions than the (111) surface. The work functions of both surfaces

generally increase moving from left to right in the transition metal series, again in qualitative agreement with trends of metal electronegativity. For the (001) surface, the minimum value appears at TiN (Ti^{3+} has a $3d^1$ configuration) and the maximum appears at CoN (Co^{3+} has a $3d^6$ configuration). Previous computational work on 4*d* TMC work functions from Hugosson[133] showed a similar trend where NbC (Nb^{4+} has a $4d^1$ configuration) had the lowest work function and PdC (Pd^{4+} has a $4d^6$ configuration) had the maximum value. Since nitrogen contributes one more electron than carbon, it is thus plausible that TMN work functions instead have a minimum for TiN and maximum for CoN.

TMNs formed by early transition metals are more stable and they also have lower work functions based on our calculations. Therefore, we further calculated the work functions of ZrN, HfN and NbN, TaN to analyze the trend in work functions between the 3*d*, 4*d*, and 5*d* TMN materials. These nitrides are stable and have been experimentally synthesized.[134] The results are shown in Figure 3.7(b), where TMNs of higher period have lower work functions, with HfN having the lowest work function (2.16 eV) among all the TMNs considered in our calculations. We believe the trend of lower TMN work function when progressing from 3*d* to 5*d* series can be understood as both being due to the lower electronegativity of metal elements when progressing from 3*d* to 5*d* series for these materials and the larger atomic radius of the metal atom facilitating an enhanced positive surface dipole, resulting in lower work function. With a work function of 2.16 eV, which is comparable to LaB_6, we propose HfN as a potential new electron emission material worthy of further study. Gotoh *et al.*[100] measured the work function of HfN thin film to be 4.7 eV by Kelvin probe, which is ~2.5 eV higher than our calculated value for (001) surface. This substantial discrepancy can be attributed to the thin film largely exposing (111) surface, which has much higher work function than (001) surface.

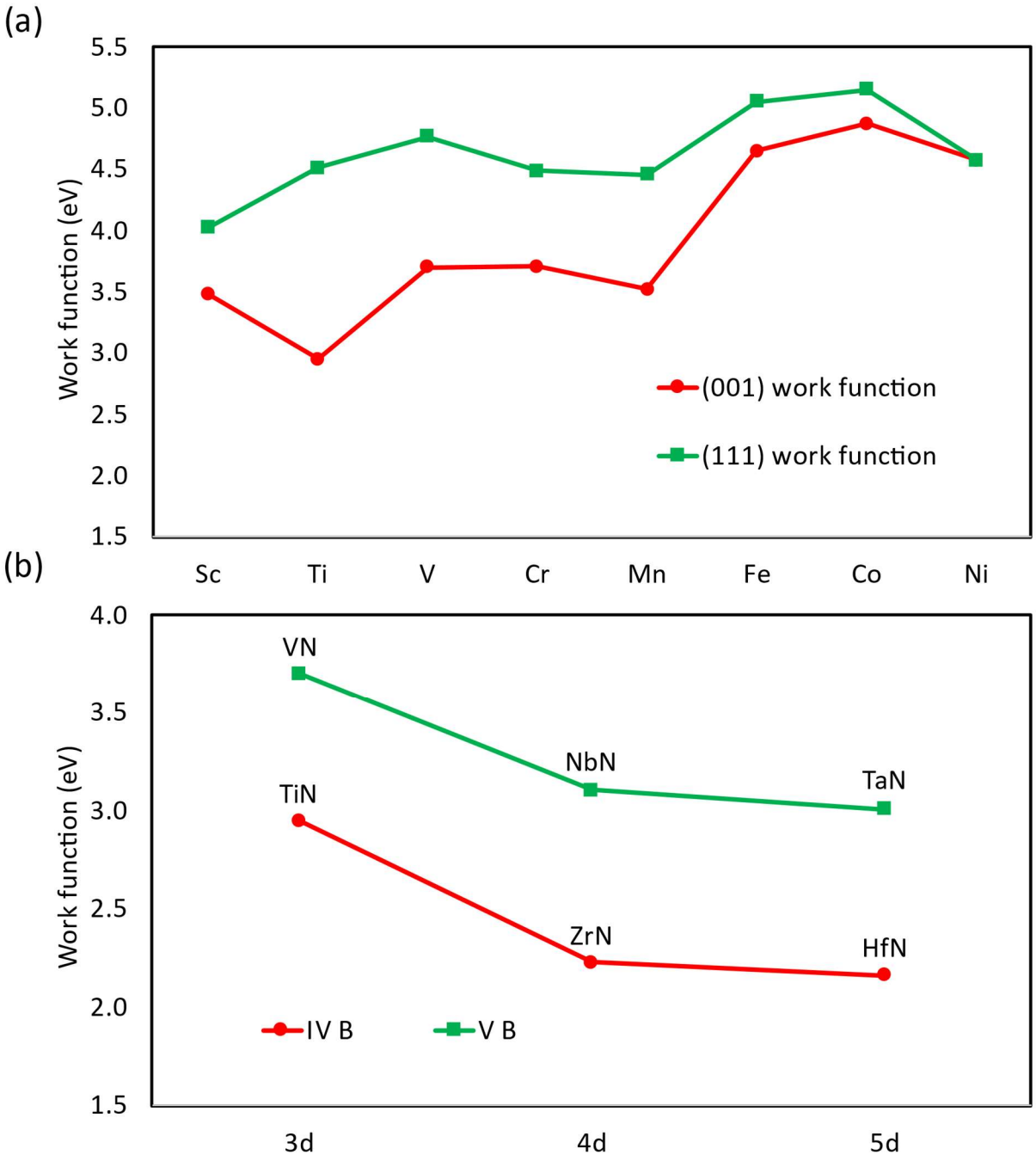

Figure 3.7: The work functions of TMNs from Sc to Ni, and TMNs of IVB and VB groups.

3.3. Summary and conclusions

In this chapter, we have used DFT calculations to systematically study the work function trends of rare-earth and alloyed hexaborides, rare-earth tetraborides, and transition metal nitrides (TMNs). From our results, we observed increasing work functions from LaB_6 to LuB_6, and confirmed that LaB_6 has the lowest work function in pure rare-earth hexaborides. This trend can be understood based on the trend in electronegativity of rare-earth metals. We then explored several $La_xBa_{1-x}B_6$ alloys and found they can possess lower work functions than either BaB_6 or LaB_6. The reduced work functions of $La_xBa_{1-x}B_6$ compared to the LaB_6 and BaB_6 endmembers originate from more significant surface relaxations induced by the misfit in atomic radius of the two metal species. We thus believe $La_xBa_{1-x}B_6$ alloys are a promising electron emission material that may offer improvements compared to commercial LaB_6, and is worth further investigation.

Our study of rare-earth tetraboride work function trends resulted in a similar trend to hexaboride work functions. However, tetraboride work functions are all higher than their hexaboride counterparts, which we understand on the basis of differences in bonding ionicity and resulting surface dipoles between these two boride families. Due to their higher work functions, it is unlikely that tetraborides will be suitable for low work function electron emission applications.

Finally, our computational analysis of TMNs found that TMNs containing early transition metals have lower work functions (e.g. TiN) than TMNs with late transition metals (e.g. CoN). We further found that when progressing from the 3d to 5d transition metal series for early transition metals (i.e. TiN-ZrN-HfN) resulted in lower work functions progressing down the periodic table. We understand these trends as being due both to metal electronegativity trends and the influence of larger metal atomic sizes on the resulting surface dipole. These calculations resulted in the

suggestion that HfN is a promising electron emission material with a low work function of 2.16 eV.

4. Benchmark the accuracy of DFT-calculated work function and the effect of typical surface structures

4.1. Introduction

The work function values of pure metals have been well-studied[155] both experimentally and computationally. Experimentally, the work functions of single- and poly-crystalline metals have been measured and tabulated. For example, the classic work from Michaelson[155] provides a database of metal work functions collected from many studies, and sheds light on the range of work function of a particular metal as a function of surface orientation, showing that for metals, the work functions of different crystalline faces vary by up to about half an eV.[156] Historically, DFT has been the computational method of choice to calculate the work function of materials. In Section 2.2.4 we have demonstrated that DFT-calculated work functions for elemental metals and LaB_6 show good agreement with experimental values, with a typical deviation of ~0.3 eV.

Contrary to the generally weak dependence of the work function on surface orientation for metals, for oxides the work function can show much stronger dependence on surface orientation and termination.[37],[38] For example, while the work functions of two metal orientations may vary by a couple hundred meV[155], Jacobs *et al.*[37] and Zhong and Hansmann[38] found the work function difference between the AO- and BO_2-terminated (001) perovskite surfaces is predicted to be on the scale of a few eV.[37], [38] This large difference is the result of different perovskite surfaces exhibiting large changes in polarity, which has a direct and large effect on the electronic surface dipole and thus the work function. In addition to the effect of various surface terminations and orientations on oxide work functions, surface adsorbates, point defects, interfacial capping layers,[38] surface reconstructions,[82]–[86] and bulk doping or composition modification resulting in shifts to the Fermi level can change the work function. In particular, the

occurrences of adsorbates, surface defects and reconstructions are environment- and processing-dependent. This dependence between processing and resulting structure can make the one-to-one comparison between simulation and experiment difficult as experimental knowledge of the atomic-level surface structure and corresponding work function for the same surface are not commonly reported in a single study.

There are challenges associated with comparing experimental and DFT-calculated work functions for oxides. As an example, Hong *et al.* reported the work functions of polycrystalline perovskite materials $LaMO_3$ (M=Cr, Mn, Fe, Co, Ni) from XPS measurements.[157] While the work functions of these polycrystals followed the same trend with composition as found from DFT, the quantitative values differed from the DFT values on the scale of an eV or more.[37] The source of such discrepancy is not rigorously known but could be due to the DFT values being reported for clean (001) AO- and BO_2-terminated surfaces, whereas the experimental samples likely contained adsorbed surface species as they were calcined in air and may have contained a number of surface orientations, terminations, or reconstructions, as the samples were polycrystalline and the atomic-level surface structure was not characterized. Similar challenges have made quantitative work function comparisons between experiment and DFT on oxides very limited and uncertain. Recently, Chambers and Sushko combined photoemission experiments and DFT calculations to investigate the work function and surface chemistry of SrO- and TiO_2-terminated $Nb:SrTiO_3$ (001) surfaces. They found good agreement between DFT-calculated and experimentally measured work function for clean TiO_2-terminated $Nb:SrTiO_3$ (001).[79] The authors also found excellent agreement with their calculated work function of 3.6-3.7 eV for SrO-terminated STO with 25% Sr vacancies and other surface adsorbates, and their measured work function of 3.6 eV.

The previous works of Jacobs *et al.*[37] and Zhong and Hansmann[38] both reported DFT-calculated work functions of $SrTiO_3$. The work of Jacobs *et al.* performed HSE-level calculations of clean SrO- and TiO_2-terminated pure $SrTiO_3$ and reported work functions without shifting the Fermi level to reflect finite-temperature or doping effects. Thus, the reported values for $SrTiO_3$ from Jacobs *et al.* are effectively ionization potentials. The work of Zhong and Hansmann used GGA-PBE calculations and shifted the Fermi level to reside at the conduction band minimum. This shift to the Fermi level was performed to mimic n-type doping of Nb into $SrTiO_3$, so the work functions reported by Zhong and Hansmann most closely reflect the work function of Nb:$SrTiO_3$ instead of pure $SrTiO_3$. While both of these previous studies made attempts to compare their calculated $SrTiO_3$ work functions with select experimental values, it is not clear from these studies alone what the best practices are for using DFT methods to obtain work functions that agree with experimental values.

Given the widespread importance of understanding and controlling the work function of oxide materials, in this chapter we perform a detailed study of $SrTiO_3$ as a first step toward validating DFT-calculated work functions of complex oxides and understanding the scale of the effect of common surface structure features (e.g. steps, defects, and reconstructions) on the work function. We have used $SrTiO_3$ as a case study example material because it has been extensively studied, thus making available prior experimental work on both the atomic-level surface structure characterization and corresponding work function[102], [158] to enable one-to-one validation. In addition, the work function of $SrTiO_3$ is of interest in its own right, as it is a ubiquitous substrate material for complex oxide thin film growth used for a variety of applications.

4.2. Results and discussion

4.2.1. Survey of experiments and validation of DFT-calculated work function for ideal surfaces

In this section, we aim to directly compare DFT-calculated work functions with experimental values for clean, undefected, and unreconstructed surfaces (which we call “ideal” surfaces). To aid in this and later comparisons the work function data and corresponding surface morphologies collected from the literature are shown in Table 4.1. It is worth noting that in some studies, the experimental work functions are reported while the surface structure is not precisely known. In this section, we restrict ourselves to using experimental work from studies where both the work function and surface structure are known, ensuring that the comparison between experimentally measured and DFT-calculated work functions is based on the same surface.

Table 4.1: Summary of $SrTiO_3$ work function values from experiments.

Material system	Surface orientation and termination	Experimental WF (eV)	Measurement technique	Reference
STO	(001) SrO	2.7	*In situ* Kelvin probe	[104]
Nb:STO	(001) SrO	3.86	UPS	[159]
Nb:STO	(001) SrO	3.6	UPS	[79]
STO	(001) TiO_2	4.2	UPS	[160]
STO	(001) TiO_2	4.3	*In situ* Kelvin probe	[104]
Nb:STO	(001) TiO_2	4.4	Retarding potential	[161]
Nb:STO	(001) TiO_2	4.08	UPS	[159]
Nb:STO	(001) TiO_2	3.8	*In situ* Kelvin probe	[104]
Nb:STO	(001) TiO_2	4.0	*In situ* Kelvin probe	[103]
Nb:STO	(001) TiO_2	4.3-4.8	*In situ* Kelvin probe	[105]
Nb:STO	(001) TiO_2	4.7	UPS	[79]
STO	(001) unknown	4.2	UPS	[162]
STO	(001) unknown	3.48	KPFM	[163]
STO	(111) unknown	3.4; 4.0; 5.2	UPS	[164]
Nb:STO	(4×1) reconstruction	4.47	XPS	[106]
Nb:STO	(2×5) reconstruction	4.05	XPS	[106]
Nb:STO	Polycrystalline	4.10 - 4.35	XPEEM	[165]
Nb:STO	SrO + 14% Sr vacancies	-1.10*	Kelvin force spectroscopy	[102]
Nb:STO	TiO_2 + 14% Sr adatoms	-1.88*	Kelvin force spectroscopy	[102]
STO	(√5×√5) reconstruction	3.12	KPFM	[158]
STO	(2×1)	n/a	n/a	[83]
Nb:STO	(2×2) A	n/a	n/a	[84]
Nb:STO	(2×2) C	n/a	n/a	[84]
STO	c(4×2)	n/a	n/a	[82]

*These are measured local contact potential differences, not absolute work functions.

The calculated work functions of SrO- and TiO_2-terminated (shown in Figure 4.1) pure STO from this work are 4.2 eV and 6.0 eV, respectively (i.e. Fermi level is positioned at the VBM). After correcting for thermal effects (see Computational methods in Section 2.2.5) the corrected work functions for SrO- and TiO_2-terminated pure STO become 2.6 eV and 4.8 eV, respectively (see Table 4.2). This correction use the DFT-calculated band gaps of SrO- and TiO_2-terminated slabs, which are 3.2 eV and 2.3 eV, respectively. While the SrO-terminated slab band gap of 3.2 eV matches the calculated (and experimental) bulk STO value, the reduced band gap for the TiO_2-terminated slab is the result of the presence of surface states characterized by undercoordinated O 2*p* orbitals on the surface.[166] This reduced band gap for the TiO_2-terminated surface is consistent with numerous previous computational studies employing both semilocal and hybrid functionals.[167]–[171] However, this reduced band gap for the TiO_2-terminated surface is not consistent with recent experimental work from Chambers and Sushko,[79] where the authors found, using XPS, that the band gap of both SrO- and TiO_2-terminated STO is equal to the bulk value. The reason for this discrepancy is not clear, and additional study may be warranted.

From Table 4.1, by using *in situ* Kelvin probe measurement, Susaki *et al.* reported the experimental work function values of SrO- and TiO_2-terminated pure STO to be 2.7 eV and 4.3 eV[104], respectively. The authors used pulsed laser deposition to grow STO thin films with different terminations, followed by annealing in oxygen atmosphere to eliminate oxygen vacancies. Our DFT-calculated SrO termination work function of 2.6 eV matches extremely well with the experimental value, while our DFT-calculated TiO_2 termination work function of 4.8 eV is half an eV higher than the experimental value, resulting in a mean absolute error of 0.3 eV for pure STO.

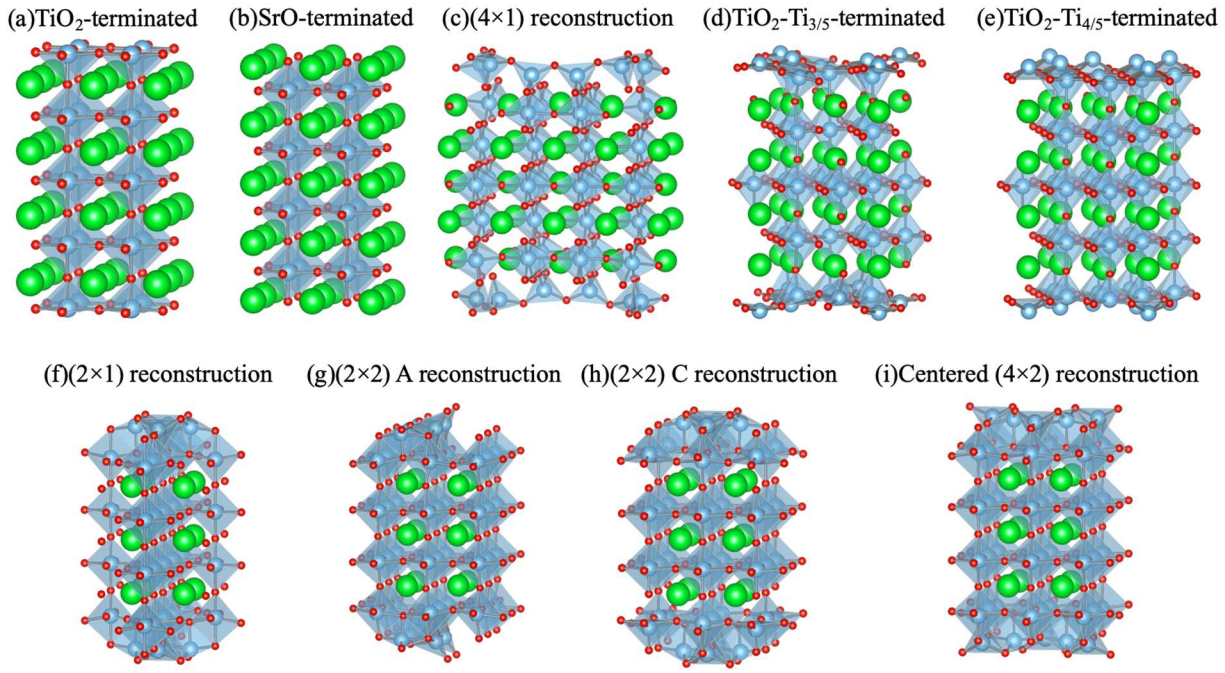

Figure 4.1: Structures of simulated slabs, (a) ideal TiO_2-terminated slab (b) ideal SrO-terminated slab (c) (4×1) reconstructed (011) surface (d) (√5×√5)R26.6° reconstruction with TiO_2-$Ti_{3/5}$ composition (e) (√5×√5)R26.6° reconstruction with TiO_2-$Ti_{4/5}$ composition (f) (2×1) reconstructed (001) surface (g) (2×2)A reconstructed (001) surface (h) (2×2)C reconstructed (001) surface (i) centered (4×2) reconstructed (001) surface.

For Nb-doped STO (Nb:STO), the calculated work functions of SrO and TiO_2 terminations are 1.2 eV and 3.8 eV, respectively. Examination of the calculated densities of states (DOS) of Nb:STO showed that Nb degenerately n-type dopes STO, causing the Fermi level to reside at the bottom of the conduction band, which is consistent with experimental behavior of Nb doping in STO (see Figure 4.2). Note that these calculated work functions are quantitatively consistent with the impact of Nb being almost entirely to shift the Fermi level and not alter the surface dipoles. Adding the calculated band gap of 3.2 eV to the calculated SrO-terminated Nb:STO work function of 1.2 eV results in an ionization potential of 4.4 eV, in good agreement with our calculated pure STO ionization potential of 4.2 eV. Similarly for the TiO_2 termination, adding the band gap of 2.3

eV to the calculated Nb:STO work function of 3.8 eV results in 6.1 eV, essentially the same value of the pure STO work function of 6.0 eV. Overall, it is clear that doping can have a large effect on the resulting work function, with the case of Nb doping resulting in reduction of the work function from the approximately half-band-gap upshift of the Fermi level. We note here that the presence of dopant species near the surface can also affect the work function by altering the surface dipole, however we have not treated surface doping here as our Nb is placed in the slab center (see Computational methods in Section 2.2.5). As might be expected from its simple role in shifting the Fermi level, we found there is little dependence of work function on Nb concentration.

For Nb:STO, the Nb dopant concentrations in experiments are equal to or lower than x_{Nb} = 1 at%, and the measured work functions of TiO_2-terminated Nb:STO are 3.8 eV[104], 4.0 eV[103], 4.3-4.8 eV[105], and 4.7 eV[79], resulting in a range of 1 eV. It is unclear at this time why the experimental range for this surface is approximately 1 eV. Our calculated work function of TiO_2-terminated Nb:STO is 3.8 eV (see Table 4.2), residing at the lower bound of these experimental values, and in good agreement with the reported values of 3.8 eV[104] and 4.0 eV.[103] We note that Chambers and Sushko obtained 4.7 eV from their GGA calculations, in excellent agreement with their measured values of 4.7 eV[79]. The large difference between their DFT value of 4.7 eV and our value of 3.8 eV is firstly due to our use of HSE vs. their use of GGA. When we use GGA we obtain a work function for TiO_2-terminated Nb:STO of 4.3 eV, much closer to their value. The remaining differences are likely due to our use of GGA-PBE vs. their use of GGA-PBEsol functionals, our use of Nb doping vs. their use of extra electron doping, and minor numerical issues in the calculation. Although for this termination, HSE and GGA results both reside in the experimental range (with HSE at the lower bound and GGA at the upper bound), we also checked

ideally truncated pure STO and other select reconstructions and found that HSE is more accurate in general.

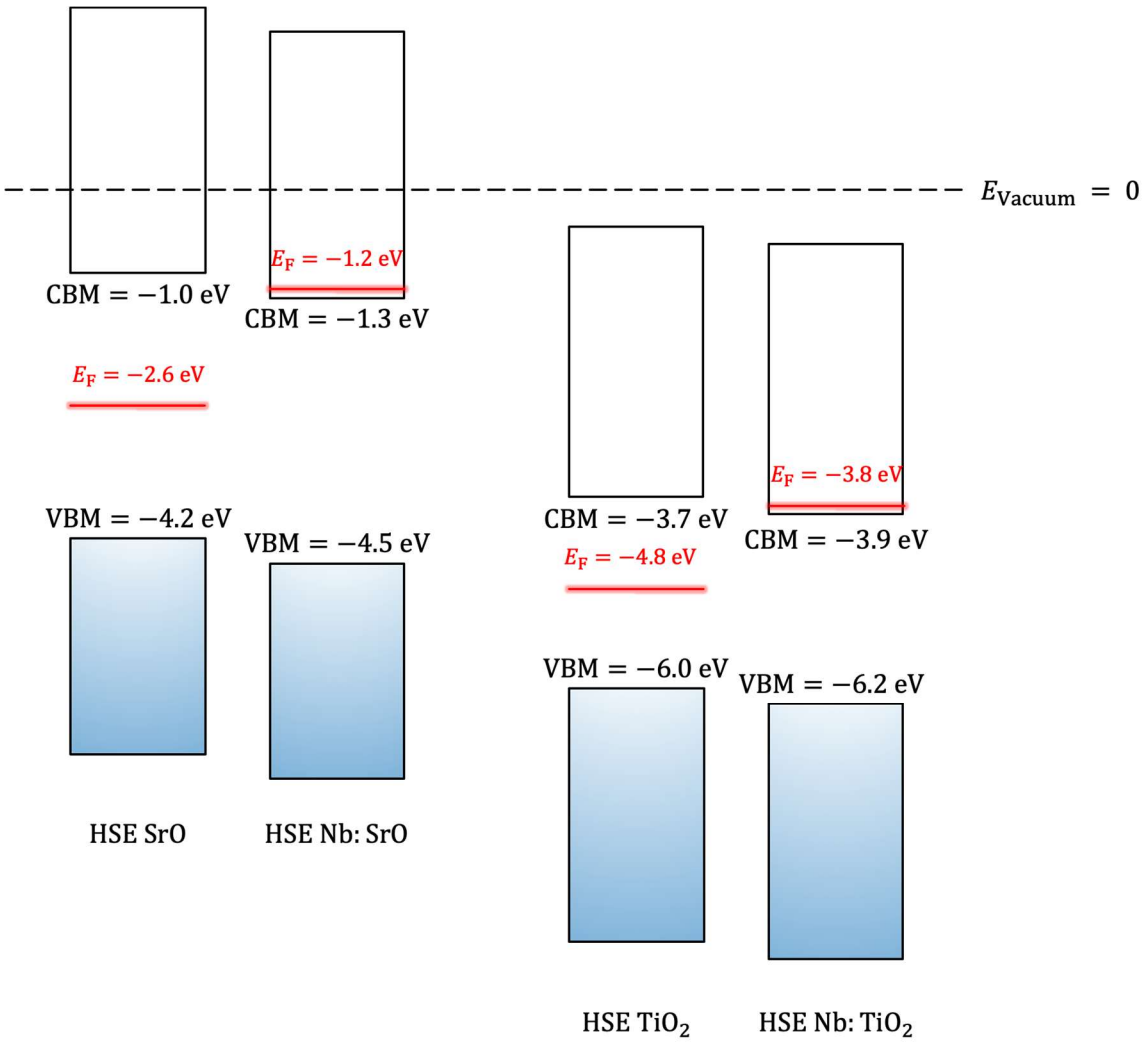

Figure 4.2: Band alignment of pure STO and Nb:STO for both SrO- and TiO_2-terminated surfaces. The Nb concentration is set at x = 6.25 at% (5 at%) for SrO- (TiO_2-) terminated slabs, respectively. Red lines denote Fermi levels. For Nb:SrO and Nb:TiO_2, the Fermi levels are elevated about 0.1 eV above the CBM due to HSE supercell size limitations creating a high doping concentration. For lower doping levels commensurate with experimental values, the Fermi level lies at the CBM.

To our knowledge, no experimental work function data has been reported for a clean and undefected SrO-terminated Nb:STO. However, Chambers and Sushko identified that their SrO-terminated Nb:STO had 25% surface Sr vacancies surface by XPS Ti 2*p* and Sr 3*d* core-level intensities, and measured the corresponding work function to be 3.6 eV.[79] We therefore compare our results to this defected SrO-terminated surface. Although we did not perform HSE calculations on this specific surface model, we did explore the influence of surface defects on the work function (see Section 4.2.3 and Figure 4.3), which we can use here to make an estimation of the work function using our methods. Introducing 25% Sr vacancies increases the work function by about 1.0 eV for the SrO termination, and adding this correction to the 2.6 eV work function of SrO-terminated pure STO results in a work function of 3.6 eV, in excellent agreement with the work of Chambers and Sushko. This estimation is made using pure STO instead of Nb:STO because, in the surface region under XPS investigation, it is likely the high concentration of 25% Sr vacancies will deplete the extra electrons introduced by Nb, which are present in a concentration of about 1%.

Overall, for the case of ideal STO and Nb:STO surfaces, our DFT calculated work functions of surfaces agree well with the lower bound of available experimental data, with expected DFT errors versus experiment on the scale of a couple hundred meV. In addition, we can compare the DFT-calculated work functions of this work and previous DFT calculations from Jacobs *et al.* and Zhong and Hansmann for SrO- and TiO_2-terminated STO. Zhong and Hansmann used DFT-GGA calculations on STO, and shifted their Fermi level to reside at the CBM, thus mimicking the behavior of Nb:STO. Comparison of their SrO- and TiO_2-terminated work functions (1.9 and 4.5 eV, respectively) with our DFT-GGA values of 1.9 and 4.3 eV shows very good agreement. Jacobs *et al.* used DFT-HSE calculations on STO and did not shift their Fermi

levels (i.e. their Fermi levels were at the VBM). Comparison of their SrO- and TiO_2-terminated work functions (3.2 and 6.3 eV, respectively) with our DFT-HSE values (unshifted) of 4.2 and 6.0 eV shows good agreement for the TiO_2-terminated surface and poor agreement for the SrO-terminated surface. We believe the reason for the discrepancy of the SrO-terminated values is because the previous study of Jacobs *et al.* used only a single *k*-point. We thus believe the values reported in the present work are more accurate than reported in Jacobs *et al*.

Finally, it is worth noting that if we use the experimental value for the TiO_2-terminated pure STO work function of 4.3 eV[104] and assume that Nb reduces the work function by approximately half the band gap (consistent with our calculations and simple intuitions), then the expected work functions for TiO_2-terminated Nb:STO is 3.1 eV (using our TiO_2-terminated slab band gap) or 2.7 eV (using the experimental or our calculated bulk band gap). Both of these values are at least 0.7 eV below the lowest measured value for the TiO_2-terminated Nb:STO work function. This suggests that the 4.3 eV[104] work function for TiO_2-terminated pure STO may be somewhat low. If we exclude that value from our comparison, the remaining comparisons possible for ideal surfaces including SrO-terminated pure STO and Nb:STO are within 0.1 eV.

4.2.2. Validation of DFT-calculated work function for select reconstructed surfaces

STO is known to undergo many different surface reconstructions as a result of different sample environments or processing paths[82]–[84], [106], [158]. In this section, we specifically simulate $(\sqrt{5}\times\sqrt{5})R26.6°$ reconstruction on (001) surface[158] and (4×1) reconstruction on (011) surface[106] at the HSE level, in order to compare with the results from recent studies where both atomic scale surface characterization and work function measurement of such reconstructed surfaces are available.

Wrana et al.[158] annealed STO at 1150 °C in low oxygen partial pressure for 1 h until the (√5×√5)R26.6° reconstruction was exposed. A work function of 3.12 eV was measured by Kelvin probe force microscopy (KPFM). There are two alternative explanations for the formation of the (√5×√5)R26.6° reconstruction, both of which occur on the (001) TiO_2 termination. The first explanation is that an extra Sr-adlayer contributes to the reconstruction[86] and the second explanation involves a Ti-adlayer with a composition of either TiO_2-$Ti_{3/5}$ or TiO_2-$Ti_{4/5}$[85]. A recent XPS study revealed that the (√5×√5)R26.6° reconstructed surface is Ti-enriched,[163] indicating the latter explanation above is more likely. Therefore, we simulate TiO_2-$Ti_{3/5}$ and TiO_2-$Ti_{4/5}$ models, whose detailed structures are shown in Figure 4.1.

From our DFT simulations, TiO_2-$Ti_{3/5}$- and TiO_2-$Ti_{4/5}$-terminated slabs are both metallic, which agrees with experimental conductivity measurements from Wrana *et al*. The DFT-calculated work functions of TiO_2-$Ti_{3/5}$ and TiO_2-$Ti_{4/5}$ terminations are 3.5 eV and 3.2 eV, respectively (see Table 4.2). These calculated values are slightly higher than the experimental work function of 3.12 eV and agree to the same level of error as the pure surfaces discussed above. However, in the experiment there were sparsely distributed Sr adatoms or O vacancies[158] at a concentration of about 1%, in addition to the known reconstructed surface structure. We can approximate that Sr adatoms (O vacancies) at this concentration would lower the work function by about 0.1 eV (0.05 eV) (see Section 4.2.3), resulting in DFT errors versus experiment in the range of roughly 0 eV (for TiO_2-$Ti_{4/5}$) to 0.3 eV (for TiO_2-$Ti_{3/5}$), once again indicating good agreement.

Riva et al.[106] obtained a reconstructed (4×1) surface on 1 at% Nb:STO (011) surface and measured the work function to be 4.47 eV from XPS. Such (4×1) surface consists of ten- and six-membered rings of corner-sharing TiO_2 tetrahedra[172], as shown in Figure 4.1. Our DFT-calculated work function of this (4×1) reconstruction on the (011) surface is 4.7 eV (see Table 4.2).

The small discrepancy of about 0.2 eV with the experimental value is again consistent with our previous comparisons. Furthermore, the discrepancy could be at least in part due to the presence of Sr adatoms[173] which occupy surface domain boundaries and appear every few nanometers.

Sokolović *et al.* recently cleaved 1 at% Nb:STO and obtained pristine (001) surfaces through a novel procedure.[102] STM/AFM measurements confirmed the presence of a reconstruction consisting of (14±2)% Sr vacancies on the SrO termination and complementary Sr adatoms on the TiO_2 termination with the same concentration. Using KPFM, the work function of the SrO (TiO_2) termination was measured to be 1.10 eV (1.88 eV) lower than that of the reference tip, resulting in a work function difference between the two terminations of $\Delta\Phi_{\mathrm{TiO_2-SrO}} = -1.88\ \mathrm{eV} - (-1.10\ \mathrm{eV}) = -0.78\ \mathrm{eV}$. It is interesting to note that typically the TiO_2 termination of STO has a higher work function, but here due to the presence of the reconstruction, the trend is reversed and the TiO_2 termination work function is 0.8 eV lower than that of SrO termination. This trend reversal is likely due to the Sr adatoms on the TiO_2 surface functioning as a layer of electropositive species, thus creating a positive surface dipole resulting in a work function lower than the SrO surface, whose work function is raised due to the Sr vacancies creating a more negative surface dipole.

We simulate both of these surface reconstructions with a slightly reduced concentration of Sr adatoms/Sr vacancies of 12.5%, which was necessary due to supercell size restrictions. From these simulations, the TiO_2 termination with 12.5% Sr adatoms is metallic and has a work function of 2.0 eV and the SrO termination with 12.5% Sr vacancies is insulating, which is consistent with the STS measurement in the experiments of Sokolović *et al*.[102] By setting the Fermi level to the middle of the band gap, the work function is 2.9 eV = 4.5 eV – 3.2 eV/2 (where 4.5 eV is the directly calculated work function and 3.2 eV is the band gap for the SrO-terminated cell with the

modeled reconstruction). The DFT-calculated work function difference is thus $\Delta\Phi_{\mathrm{Ti}_2-\mathrm{Sr}} = 2.0\ \mathrm{eV} - 2.9\ \mathrm{eV} = -0.9\ \mathrm{eV}$, which agrees well with the experimental result (see Table 4.2).

Table 4.2: Comparison of experimental and DFT-calculated work functions for ideal pure STO and Nb:STO and select reconstructed surfaces with experimentally known work functions. All DFT-calculated work functions are at the HSE level.

Material system	Experimental value (eV)	DFT calculated value (eV)
	Φ_{TiO2} = 3.8, 4.0, 4.3-4.8, 4.7	Φ_{TiO2} = 3.8
Nb:STO	$\Delta\Phi_{14\%\ Sr}$ = -0.78	$\Delta\Phi_{12.5\%\ Sr}$ = -0.9
	$\Phi_{(4\times1)}$ = 4.47	$\Phi_{(4\times1)}$ = 4.5
	Φ_{SrO} = 2.7	Φ_{SrO} = 2.6
Pure STO	Φ_{TiO2} = 4.3	Φ_{TiO2} = 4.8
	$\Phi_{(\sqrt{5}\times\sqrt{5})}$ = 3.12	$\Phi_{(\sqrt{5}\times\sqrt{5})}$ = 3.2

Finally, there are several reconstructed surfaces which have been structurally resolved from experiments, e.g. (2×1)[83], (2×2)[84], and centered (4×2)[82] (see Figure 4.1), but for which no experimental work functions are known. Together with the reconstructions discussed above, we can calculate the work functions of these additional reconstructions to further understand the scale of the effect of reconstructions on the work function. All of the (2×1), (2×2), and centered (4×2) reconstructions considered dramatically increase the work function relative to both pure STO and Nb:STO, typically on the scale of 1-2 eV (see Table 4.3). This increase in work function is reasonable considering the extra TiO_x layer introduced by these reconstructions, which functions as a negative dipole layer. Zhong and Hansmann also reported the work function of (2×1) reconstructed Nb:STO, which they found to be 6.18 eV[38] using the GGA-PBE functional. This

value is about 0.5 eV higher than our result of 5.7 eV for Nb:STO, which we use for the comparison here as the work of Zhong and Hansmann positioned the Fermi level at the conduction band minimum for $SrTiO_3$ (to mimic n-type STO). This result of GGA-PBE producing a higher n-type work function than HSE is consistent with our findings of GGA-PBE vs. HSE work functions of unreconstructed surfaces, where the use of GGA-PBE shrinks the band gap, making the CBM further below the vacuum level compared to HSE.

Table 4.3: DFT-calculated HSE work functions of reconstructed surfaces for which no experimental work functions are available. The ideal TiO_2-termination values are provided as a reference.

	Ideal TiO_2	**(2×1)**	**(2×2) A**	**(2×2) C**	**c(4×2)**
Pure STO	4.8 eV	7.2 eV	5.8 eV	6.3 eV	5.8 eV
Nb:STO	3.8 eV	5.7 eV	4.8 eV	5.0 eV	4.6 eV

4.2.3. Further understanding the role of surface defects on the work function

In this section, we seek to understand the effect on the work function of common intrinsic surface vacancies and adsorbates observed in the studies referenced in Table 4.1, specifically, O vacancies and O adsorbates on SrO and TiO_2 terminations, Sr vacancies on SrO terminations, and Sr adatoms on TiO_2 terminations. Figure 4.3 shows the DFT-calculated work functions for SrO- (Figure 4.3(a)) and TiO_2-terminated (Figure 4.3(b)) STO as a function of the surface coverage of these defects.

First, we consider O defects. O adsorbates increase the work functions of both terminations at all concentrations likely due to the electronegative O creating a negative surface dipole which impedes electron emission. Oxygen vacancies might *a priori* be expected to decrease work

function, as the removal of a negative charge near the surface might create a positive dipole. However, O vacancies increase the work function of SrO termination and reduce the work function of TiO_2 termination. The physical cause of this opposite and counterintuitive behavior of O vacancies between the SrO- and TiO_2-terminated work functions is not rigorously known at this time. However, we speculate it may be the result of different relaxations in the subsurface layer beneath the defected surface between these two terminations resulting in changes to the surface dipole. This is further evidenced by the fact that the DOS of the defected surfaces show almost no difference vs. undefected surfaces, indicating that it is unlikely that doping or other changes to the electronic structure are responsible for the observed work function changes, although additional focused study beyond the present work would be required to obtain a better understanding of this effect. Zhong and Hansmann also reported the work function of STO with 25% O vacancies. Our results are consistent with Zhong and Hansmann, where they also observed opposite work function changes on SrO- and TiO_2-terminations due to the presence of O vacancies. Further, our calculated work functions after introducing 25% O vacancies are 2.28 eV for SrO termination and 3.33 eV for TiO_2 termination, essentially the same as the results obtained by Zhong and Hansmann which are 2.26 eV for SrO termination and 3.39 eV for TiO_2 termination.

Next, we consider Sr defects. Sr vacancies on SrO termination increase the work function, which is expected as the vacancy is effectively a negative charge and increases the negative dipole at the surface. Sr adatoms on TiO_2 termination lower the work function, which is expected as the Sr is positively charged and makes a positive dipole on the surface. For non-interacting surface defects, one would expect a linear dependence of work function on surface coverage. However, in all cases except the Sr vacancy the trends with coverage are nonlinear and significantly flatten at higher coverages. This result is not surprising as such trends can involve complex coupling

between dipoles through relaxation, direct electronic interaction, and electrostatics (depolarization), but more analysis is outside the scope of this work. Overall, it is apparent that surface defects in very high concentrations like those depicted in Figure 4.3 have a large effect on the work function on the order of an eV or more. However, for more typically observed O and Sr surface vacancy concentrations of a few percent, the effect on the work function is likely on the scale of a couple tenths of an eV.

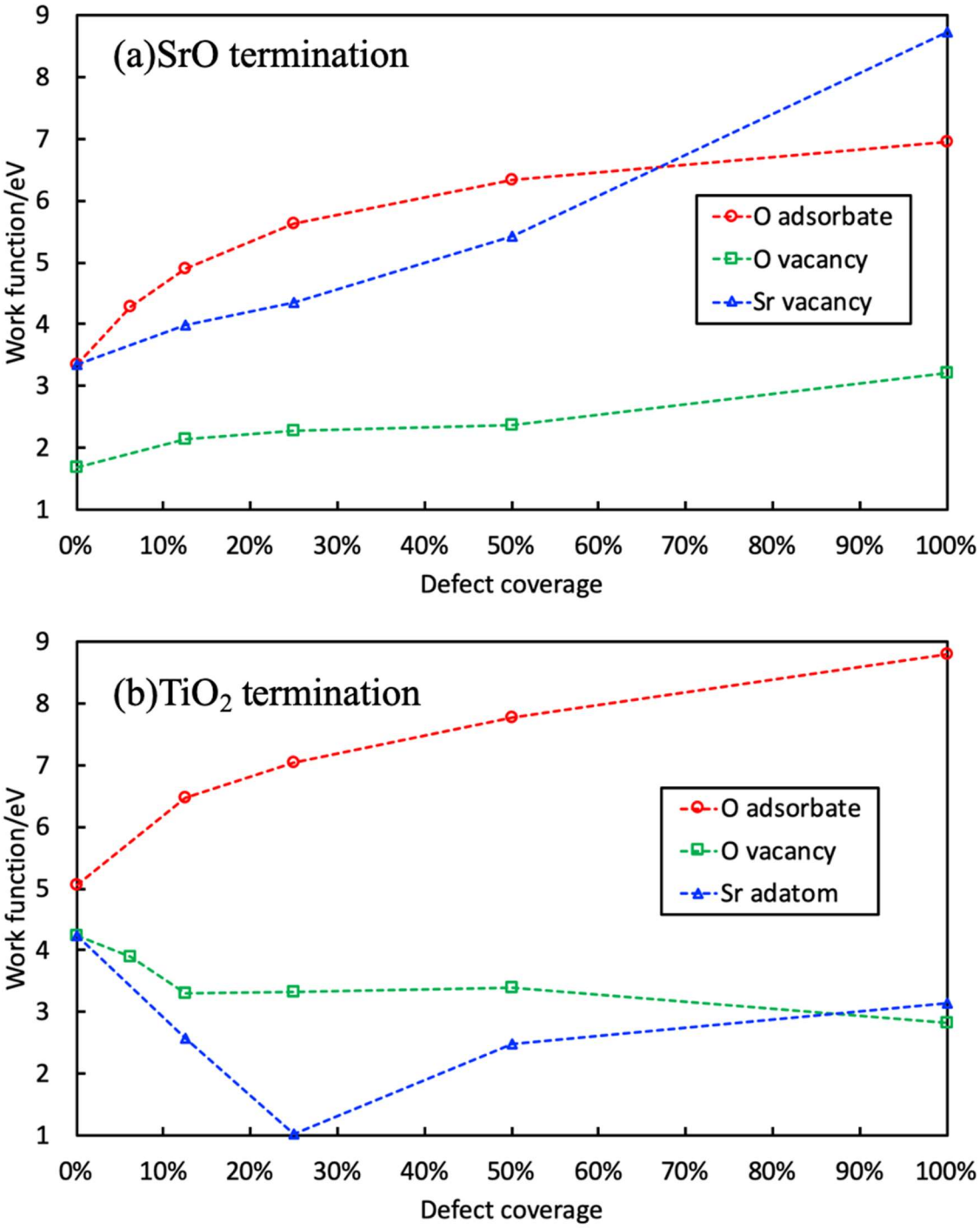

Figure 4.3: GGA work functions of defected STO with varying coverages of surface vacancies and adsorbates. (a) work functions of SrO termination with different defects (b) work functions of TiO_2 termination with different defects.

Typically, STO thin films and substrates contain surface steps arising from a miscut angle during preparation or termination of thin film growth planes. Here, we seek to understand the scale of effect of (001) surface steps on the work function. From experimental observations, surface steps mostly occur on the TiO_2 termination along <001> directions, with step heights that are integer multiples of the lattice constant[106], [174]; the SrO termination either appears as terrace on TiO_2 termination or requires extra-long time annealing to dominate.[175] Therefore, here we consider two different types of surface steps on TiO_2 termination, denoted as O-edged TiO_2 and Ti-edged TiO_2 (see Figure 4.4). As with surface defects, the impact of the steps on work function will depend on their concentration, or equivalently, their separation L. For the small cell sizes accessible in DFT we have to model unphysically small L values, and results for two L values as well as a linear extrapolation to infinite L value are shown in Figure 4.4. The GGA-level calculated work functions for ideal, O-edged and Ti-edged TiO_2 (with L = 0.39 nm ($1/L$ = 2.56 nm^{-1})) are found to be 4.7 eV, 5.2 eV, and 4.3 eV, respectively. These work function changes of 0.5 eV for O-edged TiO_2 and -0.4 eV Ti-edged TiO_2 are an extreme upper bound of the scale of the effect of steps due to the large simulated step concentration. The lines in Figure 4.4 indicate linear fits to these three data points (for each step type) with an intercept fixed at 4.65 eV, which is the work function of the ideal surface (i.e. no surface steps). The fits have high R^2 values suggesting a linear trend in work function with defect concentration. Assuming the defects are effectively non-interacting, impact the work function only through dipoles, and each contribute the same surface dipole, such linear behavior is expected, since the work function change is linear in the change in surface dipole. Thus it is reasonable to assume that the influence of dilute surface step concentrations on a work function will be linear in the defect concentration for low concentrations, and our fit will therefore scale accurately to realistic surface step concentrations. Considering a

more realistic step separation of L = 200 nm[106], [174], [175], a realistic step concentration in experiments is only about 1/500 of that in our simulations. At these physical concentrations our results show that surface steps will have a negligible effect on the work function, on the scale of approximately a few meV (see Figure 4.4). Even if our linear model is not perfectly correct it seems unlikely that some deviation from linearity would somehow lead to a significant work function modification for realistic step concentrations.

In addition to the defects and reconstructions to $SrTiO_3$ we have discussed above, the formation of interface heterostructures can also influence the work function of perovskites by doping and modification of the surface dipole. For example, the work of Zhong and Hansmann demonstrated that interfacing $SrTiO_3$ with $SrNbO_3$ results in charge transfer and interactions between the surface dipoles that can result in a work function of the interface material lower than either of the parent materials can obtain in isolation.[38] While the detailed examination of interfacial effects on the $SrTiO_3$ work function is beyond the scope of this study, using interfaces to achieve work function tuning is an interesting area for further research.

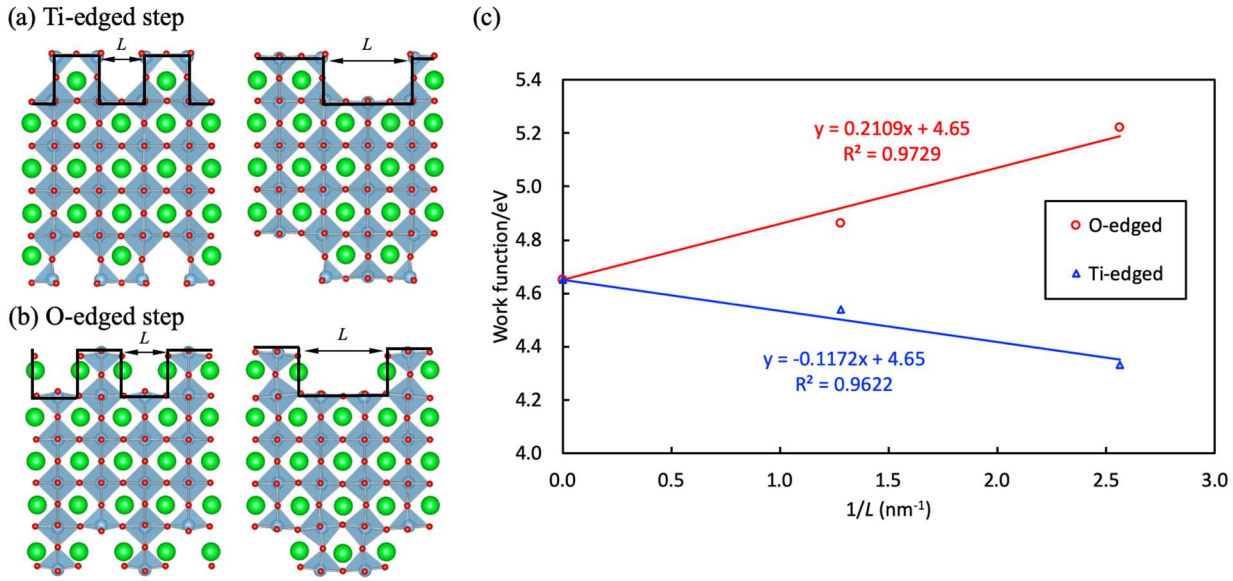

Figure 4.4: Simulation slabs showing geometry of (a) Ti-edged step and (b) O-edged step along <001>, with two different values of *L*. (c) The calculated GGA work functions for O-edged (red points) and Ti-edged (blue points) surface steps versus inverse step size. The solid lines denote linear fits to the calculated data with an intercept fixed at 4.65 eV, which is the work function of ideal surface (i.e. no surface steps).

4.3. Summary and conclusions

In this chapter, Density Functional Theory calculations were used to assess the accuracy of oxide work functions for which both the experimental surface structure and work function are known, using perovskite $SrTiO_3$ as a case study example. These results support that DFT-HSE methods can provide accurate work functions for at least one complex oxide system ($SrTiO_3$), and additional detailed comparisons are needed to assess if this agreement extends to other systems. From this work, a number of key facts have emerged which we believe are of general interest for modeling and understanding the work function of oxide materials: (1) DFT and experimental work functions for $SrTiO_3$ are in good agreement, typically within about 0.3 eV, provided the simulation and experiment are both measuring the same surface. (2) DFT calculations using HSE functionals yield more accurate work function values compared to the GGA-PBE functional. The lower

accuracy of GGA-PBE in this case stems from both the underestimation of the band gap and the incorrect positions of the valence and conduction band edges relative to vacuum. (3) The use of GGA-PBE seems to correctly capture the *changes* in work function of a given surface with the introduction of common surface defects such as steps and point defects, indicating that the use of GGA-PBE correctly captures the relative surface dipole electrostatics, at least in the case of $SrTiO_3$. In addition, we have assessed the scale of the effect of common bulk and surface modifications on the work function. Nb doping at typical concentrations of 1 at%, in the absence of any segregation to the surface, primarily elevates the Fermi level of $SrTiO_3$ to the CBM and does not significantly impact the surface dipole. Therefore, Nb doping reduces the undoped $SrTiO_3$ work function on the scale of half the band gap. The presence of surface steps has a negligible influence on the work function at typical concentrations, on the scale of just a few meV. Surface reconstructions and adsorbates can increase or reduce the work function on the scale of an eV or more. For surface vacancies, typical concentrations of up to a few percent likely result in work function changes of a couple tenths of an eV. The direction and magnitude of the work function change follows known chemical intuition of surface species electronegativities and resulting surface dipoles, except for O deficient SrO termination where subsurface relaxation alters the surface dipole. Overall, as a first step of the validation of DFT calculated work functions for complex oxides, this work suggests that DFT-calculated work functions of $SrTiO_3$ are accurate versus experiment to within a couple tenths of an eV, codifies the scale of effect of common surface defects on the work function, and sheds light on the quantitative work function values and physics of $SrTiO_3$, an essential oxide material with numerous technological applications.

5. Discovery and engineering of low work function perovskite materials

5.1. Introduction

Despite the commercial use of B- and M-type cathodes and decades of research on scandate cathodes, impregnated cathodes of all types have important shortcomings. Namely, these cathodes suffer from Ba depletion[25], [26] and surface degradation[19] as a result of the continual evaporation of Ba from the emitting surface during high temperature operation. This off-gassing of the work-function-lowering Ba species limits the cathode lifetime. In addition, impregnated cathodes can experience non-uniform Ba coverage, leading to device efficiency limits[27] and engineering challenges.[28] For the specific case of scandate cathodes, the previous shortcomings all apply, but scandate cathodes tend to require extra activation and have issues of manufacturing and performance repeatability.[24], [29]–[31] These above-mentioned issues all stem from the fact that impregnated cathodes realize their low work function through the formation of a volatile surface dipole layer believed to be comprised mainly of Ba and O.

To achieve low work function without such fragile surface layer, in this chapter we turn our attention to perovskite oxide materials ($A_{1-x}A_x'B_{1-y}B_y'O_3$ stoichiometry). This high degree of compositional flexibility enables perovskites to have a wide range of tunable properties, including tunable work function values. The recent studies of Jacobs *et al.*[37] and Zhong *et al.*[38] both demonstrated that the work function of perovskite materials can vary on the scale of several eV, and depends on the bulk material composition, the surface orientation (e.g. (001) versus (011)), and the surface termination (e.g. AO- versus BO_2-terminated (001) surface). These studies were the first to characterize the work functions of a representative set of perovskite oxides using Density Functional Theory (DFT) methods for applications in electron emission and heterojunction engineering, and suggest that perovskites with low work functions may be realized

by virtue of the polar (001) oriented surfaces of the perovskite structure.[37], [38] Jacobs *et al.* also identified an approximate linear correlation between (001) surface work function and the bulk O *p*-band center.[37] A recent study from Xiong *et al.*[176] used data-driven approach to analyze the electronic-structure factors controlling the work function of perovskites, and corroborated that the O *p*-band center is an effective work function descriptor. The O *p*-band center is the centroid of the oxygen-projected density of states, and can be calculated from a single DFT bulk structure relaxation run. This established correlation of surface work function with bulk O *p*-band center enables fast screening of perovskite work functions at a rate that is approximately two orders of magnitude faster than conducting computationally expensive HSE[65] hybrid functional calculations of perovskite surface slabs. Jacobs *et al.* specifically identified $SrVO_3$ as a promising cathode material with a calculated (001) SrO terminated work function of about 1.9 eV and predicted that Ba dopant impurities in $SrVO_3$ should segregated onto the (001) surface, creating a BaO-terminated (001) surface with a very low work function of 1.1 eV[37]. Meanwhile, $SrVO_3$ has been experimentally shown to be a good electronic conductor and stable under reducing conditions.[39], [40] These properties make $SrVO_3$ a promising electron emission cathode material worthy of further study. This naturally leads to the question: what other perovskite oxides might also have a low work function, good electrical conductivity, and good chemical stability, and thus be promising electron emission materials?

Motivated by these questions of materials discovery and design of low work function perovskites, we perform high-throughput screening using DFT methods to assess the predicted work function, thermodynamic stability under operating conditions, and conduction characteristics of 2913 perovskite oxide compositions. Our high-throughput screening results in the discovery of seven compounds predicted to have low (< 2.5 eV) AO-terminated (001) surface work functions.

Examples of promising compounds include $BaMoO_3$, $SrNb_{0.75}Co_{0.25}O_3$, $BaZr_{0.375}Ta_{0.5}Fe_{0.125}O_3$ and $BaZr_{0.375}Nb_{0.5}Fe_{0.125}O_3$, which are predicted to have work functions of 1.1 eV, 1.5 eV, 0.9 eV and 1.6 eV, respectively. In addition, the new HSE-level work function data obtained from this screening allowed us to further verify and refine the correlation between surface work function and bulk O *p*-band center first proposed in [37]. Finally, the large amount of data obtained from this computational search enable an enhanced understanding of the materials chemistry governing the work function of perovskite oxides. Specifically, we discover a qualitative empirical relationship between the work function and the number of *d* electrons, where materials with barely filled *d* bands (e.g. only one or two *d* electrons) result in the lowest work functions while insulators containing zero *d* electrons and late transition metal perovskites with nearly filled *d* bands result in the highest work functions.

5.2. Results and discussion

5.2.1. High-throughput materials screening procedure and elimination criteria

Figure 5.1 contains an overview of the high-throughput screening process and elimination criteria used in this work. The complete set of 2913 perovskite materials is obtained in part from a previous high-throughput screening study of perovskite oxides for the application of stable, high activity oxygen reduction catalysts for solid oxide fuel cells.[94] The remaining perovskite materials are simulated in this study with the aid of the MAterials Simulation Toolkit (MAST).[177] Additional details of the composition spaces explored and other computational details can be found in Section 2.2.5. Here, we list our chosen elimination criteria used to successively reduce the space of promising perovskite materials for use as low work function electron emitters. The subsequent sections provide our rationale for the choice of each of these elimination criteria, together with the

results of the screening analysis for each criterion. The first screening step uses the bulk O *p*-band center as a descriptor of the work function to eliminate materials with a predicted work function higher than 2.01 eV, which is the predicted value of $SrVO_3$ at the GGA level. The second screening step uses this down-selected pool of low predicted work function candidates further eliminated compounds expected to be less stable under typical thermionic cathode operating conditions than $SrVO_3$ based on convex hull analysis, i.e. materials with an energy above the convex hull greater than 43 meV/atom, the calculated stability value of $SrVO_3$ at the GGA+*U* level. The third screening step assesses the DFT-predicted electronic conductivities of the pool of predicted low work function, stable materials using HSE functional. In our screening process we eliminate materials that are predicted to have band gaps of 0.5 eV or greater, based on the expectation that they will be poor electrical conductors. Finally, the last screening step is to directly calculate the (001) AO-terminated work function at the HSE level and eliminate compounds with a work function of greater than 2.5 eV, therefore producing the set of new promising perovskite materials as low work function thermionic cathodes. We remark here that materials that are insulating but have low work function, while not promising for use as thermionic cathodes in high power VED applications, may still find use as field emission coatings. For example, the materials $Ba_{0.65}Sr_{0.35}TiO_3$[178], [179] and N-doped $SrTiO_3$[180], [181] have been successfully used as thin film, work-function-lowering field emission coatings on Si, as well as direct field emission from nanotips of $PbZr_xTi_{1-x}O_3$.[182] As the field emission process relies on a low work function and electron tunneling through the cathode surface, the use of an insulating material is less of a critical design issue.

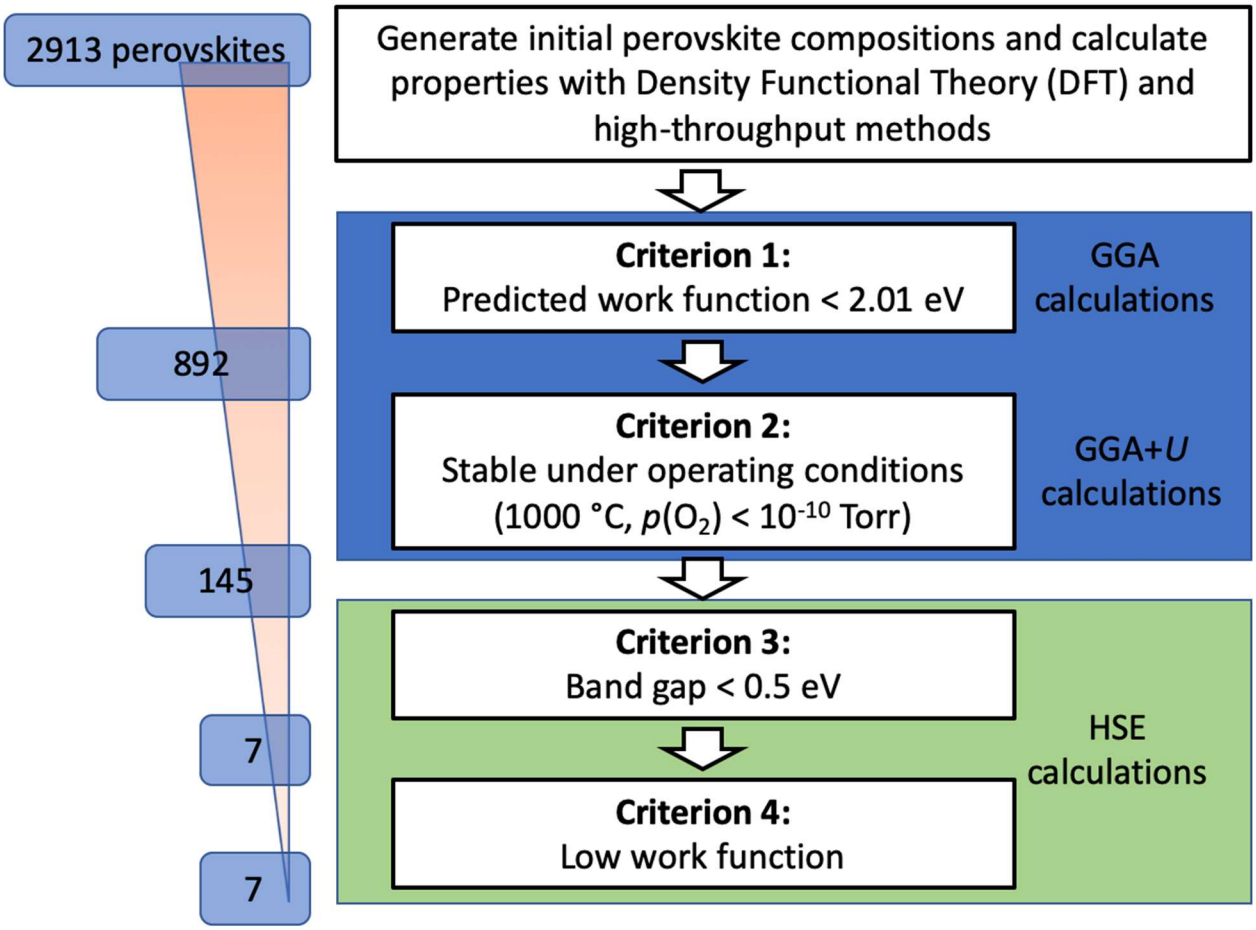

Figure 5.1: Diagram illustrating the DFT-based high-throughput screening process used in this chapter. At each step of the screening process, an elimination criterion is invoked to reduce the pool of potentially promising perovskite compounds.

5.2.2. Elimination criterion 1 (predicted work function)

Reference [37] demonstrated a linear relationship between the HSE-calculated work function (for both AO- and BO2-terminated (001) surfaces) and bulk HSE O *p*-band center. However, it is computationally intractable to screen the full set of 2913 perovskites in this study at the HSE level. Therefore, it is first necessary to verify this correlation persists at the GGA level. Here, we choose to evaluate the O *p*-band center trend at the GGA level as opposed to the GGA+*U* level based on recent findings that showed that GGA resulted in improved statistical correlations of numerous perovskite properties with the O *p*-band center compared to the use of GGA+*U*.[183]

Figure 5.2 contains a plot of the GGA-calculated AO work function of a representative set of 27 perovskites as a function of the bulk GGA O *p*-band center. We note here that in this chapter, all predicted and calculated work functions are for (001) oriented perovskites with the AO surface termination. This is chosen as the surface of interest based on work reported in [37], [38] that showed that these surfaces tend to have low work functions due to surface dipoles directed away from the terminating surface that lower the electrostatic barrier and the work function. The set of perovskites used to construct the correlation in Figure 5.2 includes: La(Sc, V, Cr, Mn, Fe, Ru, Co, Ni, Cu, Al, Ga)O_3, Sr(Ti, Zr, V, Nb, Cr, Mo, Mn, Fe, Ru, Co)O_3, and Ba(Ti, Zr, Hf, Mo, Nb, Sn)O_3. Figure 5.2 demonstrates there is a linear relationship between the GGA AO work function and GGA bulk O p-band center with an R^2 value of 0.83. This correlation is slightly higher although generally quite similar to that of AO work functions for metallic perovskites at the HSE level in ref[37] (R^2 = 0.77). By applying the correlation between work function and O *p*-band center in Figure 5.2, we eliminate candidate materials with predicted work function higher than 2.01 eV, the predicted work function of $SrVO_3$ at the GGA level. $SrVO_3$ is chosen as the reference system to ascertain whether other perovskites have a sufficiently low predicted work function to be interesting for two reasons: (1) $SrVO_3$ has already been simulated at the HSE level and shown to have a low (001) AO terminated HSE work function of about 1.9 eV,[37] thus making it a promising material, and (2) our choice of using a known promising material for the work function cutoff is a conservative one, which will likely minimize the number of false positive predictions. It is possible that we may have missed some compounds with slightly higher but still relevant work functions of 2-2.5 eV (i.e. about 0.5 eV higher than the HSE-calculated value for $SrVO_3$). However, these DFT calculations make many assumptions including perfect, defect-free microstructures. Therefore, we applied the more conservative 2.01 eV cutoff criteria to increase

the likelihood that the identified low work function candidates will have low work functions in practice and thereby justify further, in-depth experimental assessment.

The results in Figure 5.2 are fit to line to yield the following relationship between the GGA (001) AO-terminated work function and the bulk O *p*-band center:

$$\Phi_{\mathrm{AO,pred}}^{\mathrm{GGA}} = 0.52 \times \mathrm{O}_{p-\mathrm{b}} \quad + 3.90 \qquad 5.1$$

Using this relationship between predicted GGA work function and O *p*-band center, we calculated the predicted work function of all 2913 simulated perovskites. In this screening step, 892 perovskites have a predicted work function lower than the $SrVO_3$ predicted GGA value of 2.01 eV.

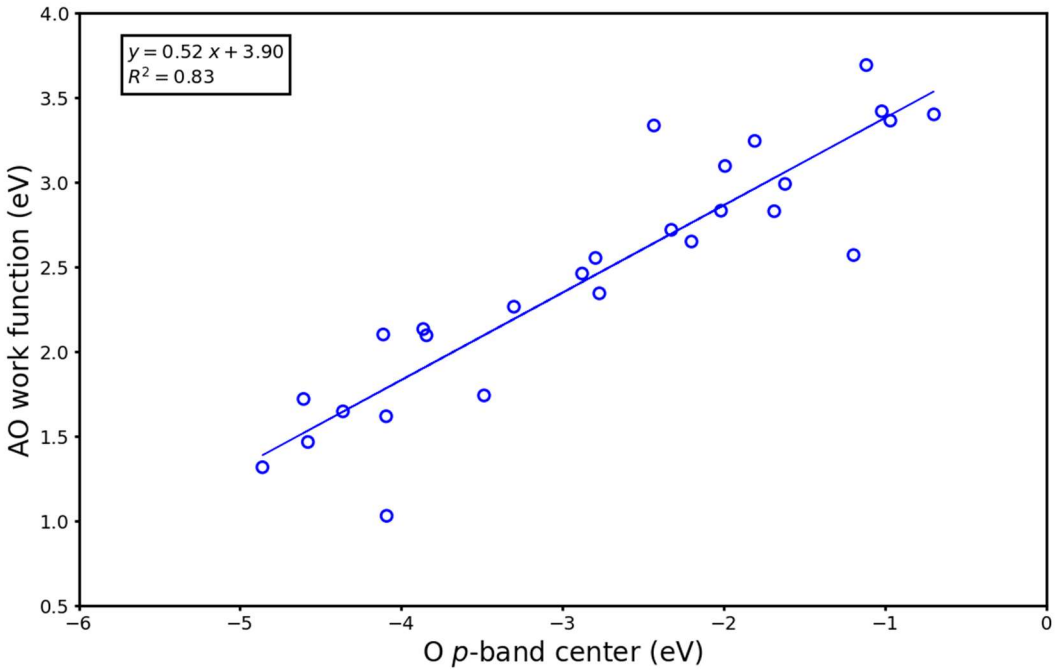

Figure 5.2: Calculated GGA AO surface work functions of a representative set of 27 different perovskites with respect to their bulk GGA O *p*-band centers.

5.2.3. Elimination criterion 2 (stability under operating conditions)

Next, we choose to exclude perovskites that are calculated to be unstable in a typical thermionic cathode operating environment of high temperature and ultra-high vacuum corresponding to T = 1000 ˚C and $p(O_2) = 10^{-10}$ Torr. We use the energy above the convex hull (E_{hull}) as a measure of material stability. E_{hull} measures the decomposition energy of a material into the set of most stable phases, with a value of zero indicating the material under investigation resides on the convex hull and is formally stable. Recent studies have shown that there are numerous materials that are calculated from DFT to reside above the convex hull, yet can be routinely synthesized and used in functional applications. These studies have found that a more realistic cutoff of material stability may be up to about 50 meV/atom above the hull.[184]–[186] From our analysis, we found that $SrVO_3$ has an E_{hull} value of 42 meV/atom under thermionic cathode operating conditions. This value is within the E_{hull} range of materials found to be readily synthesizable, and $SrVO_3$ has been experimentally made and used in applications ranging from oxide electronics to anodes for solid oxide fuel cells.[39], [187]–[189] Therefore, to focus on a smaller set of materials with even higher probability of good stability, we use the E_{hull} value of 42 meV/atom as the stability elimination criterion.

Figure 5.3 contains a plot of the predicted work function (calculated from the O *p*-band center descriptor trend in Figure 5.2) as a function of the calculated E_{hull} values for all materials analyzed in this study. In the scatterplot of Figure 5.3, the data are grouped according to the number of *d*-band electrons, as determined by electron counting rules assuming completely ionic bonding. Figure 5.3 illustrates that materials with zero *d*-band electrons have high predicted work functions while materials with a low, but nonzero, number of *d*-band electrons (greater than zero but less than or equal to three) have the lowest predicted work functions. Materials with *d*-band electron

counts greater than three but less than or equal to ten have a spread in work function values, but their predicted work functions are similar to materials with zero *d*-band electrons, i.e., consistently higher than the materials with few (but nonzero) *d*-band electrons. These trends are discussed in more detail in Section 5.2.7. Applying our stability screening, the previous pool of 892 candidate materials is reduced to 145 materials.

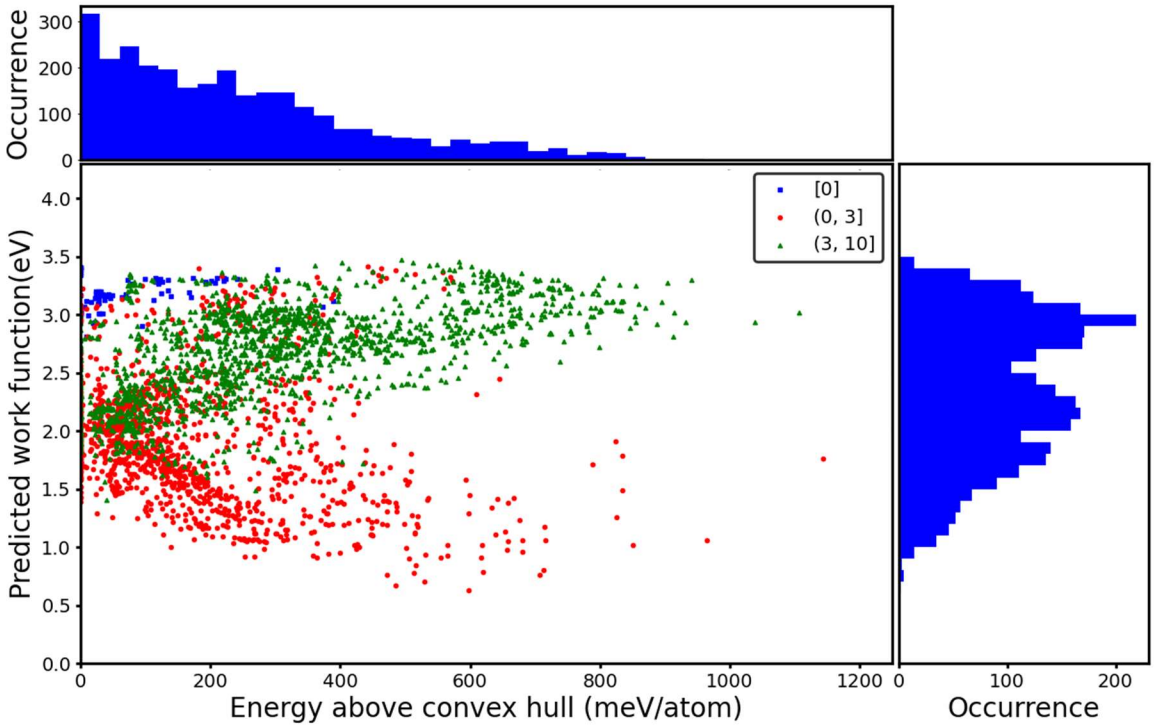

Figure 5.3: Plot of predicted work functions calculated using the O *p*-band center descriptor as a function of E_{hull} under typical thermionic cathode operating conditions for all materials in this study. The two histograms along *x*- and *y*-axis demonstrate the distribution of energies above convex hull and the distribution of predicted work functions, respectively. The blue, red and green symbols denote perovskites with n electrons in the *d*-band ($n = 0$, $0 < n \leq 3$, $3 < n \leq 10$, respectively), based on electron counting rules assuming completely ionic bonding.

5.2.4. Elimination criterion 3 (electrical conductivity)

The third step of our screening process is to remove candidate materials that are unlikely to be sufficiently electrically conductive for use as thermionic electron emitters. It is necessary for

a thermionic emitter material to be electrically conductive in order to realize the desired high current emission densities required in modern vacuum electronic devices. We assume that only examining materials with zero band gap is too stringent a cutoff. The perovskites examined in this work typically contain transition metals in high oxidation states (e.g. Co^{4+}). Consequently, additional physics of these materials may occur at the high operating temperatures of thermionic cathodes that could produce a reduction in the bandgap compared to the zero temperature DFT-calculated HSE band gap. These physics could include: magnetic transitions[190], formation of oxygen vacancies[191], or small structural changes (e.g. Jahn-Teller distortion[190]) that would influence the electronic structure without resulting in a large structural change. While it is difficult to quantify the energy scale of these effects on the band gap in a general way, we assume a reasonable upper bound of 0.5 eV. Therefore, we use a band gap of 0.5 eV as the threshold value, and eliminate compounds with an HSE-calculated band gap greater than 0.5 eV. As aforementioned, such insulating materials may find use in field emission applications, but are not in the scope of this chapter.

From our last screening step, 145 materials pass the predicted work function and stability elimination criteria. In this screening step, we calculate the bulk HSE-level band gaps of 25 of these 145 compounds which have the lowest predicted work functions according to the linear correlation depicted in Figure 5.2, based on their O *p*-band centers. The results are tabulated in Table 5.1. Based on this analysis of 25 compounds, 4 compounds are predicted to have band gaps less than 0.5 eV while the remaining 21 compounds are predicted to have band gaps higher than 0.5 eV, or insulating, and thus not useful as vacuum electronic cathodes. We therefore choose to focus our remaining analyses on the four low band gap, (probably) conductive compounds: $Sr_{0.5}La_{0.5}MoO_3$, $Ba_{0.25}Ca_{0.75}MoO_3$, $SrMoO_3$ and $BaZr_{0.375}Ta_{0.5}Fe_{0.125}O_3$.

Table 5.1: Summary of the predicted work functions, calculated stabilities, and HSE band gaps of perovskites passing the first two elimination criteria.

Composition	Predicted work function (eV)	E_{hull} (meV/atom)	HSE band gap (eV)
$La_{0.75}Y_{0.25}MoO_3$	1.29	25	1.47
$Ca_{0.25}La_{0.75}MoO_3$	1.39	0	0.66
$LaMn_{0.125}Ga_{0.875}O_3$	1.41	41	3.25
$La_{0.5}Y_{0.5}MoO_3$	1.42	0	1.51
$La_{0.75}Gd_{0.25}VO_3$	1.43	0	2.20
$Sr_{0.5}La_{0.5}MoO_3$	1.43	0	0.47
$Gd_{0.5}Y_{0.5}MoO_3$	1.45	24	1.48
$Ca_{0.5}La_{0.5}MoO_3$	1.47	0	1.16
$La_{0.5}Gd_{0.5}VO_3$	1.47	0	2.18
$LaTi_{0.5}Fe_{0.5}O_3$	1.50	31	2.95
$LaMg_{0.125}V_{0.875}O_3$	1.51	0	1.33
$Pr_{0.5}Gd_{0.5}VO_3$	1.52	0	2.18
$Pr_{0.5}Gd_{0.5}MoO_3$	1.52	0	1.40
$LaV_{0.5}Fe_{0.5}O_3$	1.56	38	2.01
$YMoO_3$	1.58	0	1.71
$Pr_{0.75}Gd_{0.25}VO_3$	1.58	0	2.19
$CaMoO_3$	1.58	0	0.55
$Ba_{0.25}Ca_{0.75}MoO_3$	1.59	14	0.02
$Gd_{0.25}Y_{0.75}MoO_3$	1.59	0	1.36
$SrMoO_3$	1.59	0	0.03
$GdVO_3$	1.60	25	2.26
$Gd_{0.5}Y_{0.5}VO_3$	1.60	0	2.28
$LaMg_{0.25}V_{0.75}O_3$	1.61	0	1.39
$BaZr_{0.375}Ta_{0.5}Fe_{0.125}O_3$	1.62	41	0.38
$LaCrO_3$	1.63	0	0.76

5.2.5. Elimination criterion 4 (quantitative work function calculation)

Table 5.2 summarizes the E_{hull}, HSE-calculated band gaps, and HSE-calculated work functions, for the four materials obtained from the band gap screening step. In addition, it includes another three materials, outside of the top 25 predicted low work function materials listed in Table 5.1, which also passed the band gap screening step. These three materials were found to be promising from an earlier version of our screening analysis. We included them in Table 5.2 for completeness because they passed all screening criteria conducted thus far. Our calculations show that for these seven materials, all of them have HSE-calculated work functions below 2.5 eV. These materials include $BaMoO_3$ and $Sr_{0.5}La_{0.5}MoO_3$, which have very low work functions of 1.1 eV and 1.3 eV, respectively. Overall, we have found seven perovskite materials that emerge as promising, new, stable, low work function, conductive materials for further exploration as thermionic electron emitters.

Table 5.2: Summary of HSE-calculated work functions for all materials passing elimination criteria 1-3, and the most promising compounds identified in this chapter.

Composition	E_{hull} (meV/atom)	HSE bandgap (eV)	HSE work function (eV)
$SrMoO_3$	0	0.03	1.93
$BaMoO_3$	24	0.38	1.06
$Sr_{0.5}La_{0.5}MoO_3$	0	0.47	1.86
$Ba_{0.25}Ca_{0.75}MoO_3$	14	0.02	1.68
$SrNb_{0.75}Co_{0.25}O_3$	37	0.03	1.51
$BaZr_{0.375}Ta_{0.5}Fe_{0.125}O_3$	41	0.38	0.93
$BaZr_{0.375}Nb_{0.5}Fe_{0.125}O_3$	21	0.41	1.56

5.2.6. Refinement and validation of O *p*-band center as a work function descriptor

We have used these seven work function values in Table 5.2 and the original 20 work function values from ref[37] to refine the trends of HSE-calculated AO surface work functions versus the bulk HSE O *p*-band center previously revealed in [37]. In addition, as a further test of this correlation, we choose a select group of perovskites found to have very low O *p*-band centers that are lower in value than the materials comprising the original trend, and also include the calculated HSE work functions of these materials. These test materials are chosen solely based on their low O *p*-band center values, regardless of their stability or band gap values. These additional test materials consisted of: $BaNbO_3$, $SrNbO_3$, $PrHfO_3$, $BaTaO_3$, $Ca_{0.5}Ba_{0.5}Ta_{0.5}Nb_{0.5}O_3$, $La_{0.5}Ba_{0.5}Ta_{0.5}Nb_{0.5}O_3$, $La_{0.5}Ba_{0.5}NbO_3$, $Ba_{0.5}La_{0.25}Rb_{0.25}NbO_3$ ($La_{0.5}Ba_{0.5}O$- and $La_{0.5}Ba_{0.25}Rb_{0.25}O$-terminated AO surfaces), and $La_{0.5}Rb_{0.5}NbO_3$.

Figure 5.4 shows the HSE-calculated AO surface work function versus the HSE bulk O *p*-band center values for materials from [37], the promising materials from the screening conducted in this work, as well as the above-discussed test set of very low predicted work function materials. In comparison to the trend of GGA work function and O *p*-band center values in Figure 5.2, the linear correlation between work function and O *p*-band center in Figure 5.4 splits into two trend lines. Consistent with the results and explanation from [37], these two distinct trendlines are the result of differences in the electronic structure of these two sets of materials. The materials comprising the top trend line are either band or Mott-Hubbard insulators with a nonzero HSE-calculated band gap and the materials comprising the bottom trend line are correlated metals.[37]

Now that many more perovskite materials have been included in the trends displayed in Figure 5.4, some comparisons can be drawn between the trends in Figure 5.4 and the original trends presented in ref[37]. In ref[37], the insulator and metal trend lines had R^2 values of 0.78 and

0.77, respectively. In Figure 5.4, the updated lines of best fit show the insulator and metal trend lines have R^2 values of 0.47 and 0.80, respectively. It is evident the inclusion of more data results in a significantly worse correlation for insulating compounds, but a similar correlation for metallic compounds. Regarding insulating compounds, the poor correlation is expected as the calculated work functions for (001) AO surfaces of insulating perovskites are limited to a small range between about 2.5-3.5 eV so even a spread in the work function values of a few tenths of an eV relative to the trend line results in a low R^2 value. Regarding metallic compounds, the consistent correlation despite our inclusion of new data spanning a larger domain of O *p*-band center values and a larger dynamic range of (001) AO work functions between about 0.8-3.3 eV is encouraging. For the metallic compounds, the corresponding RMSE/σ = 0.45, much smaller than the insulator case (RMSE/σ = 0.73), indicating a statistically more robust fit to the metallic compound work functions.

Although the O *p*-band center is a reasonably accurate descriptor of HSE work functions for metallic perovskites, one disadvantage of employing this bulk descriptor is it cannot capture the effect of different surface dipoles yielding different work functions for a particular material. As a concrete example, Figure 5.4 shows the work functions of $Ba_{0.5}La_{0.25}Rb_{0.25}NbO_3$ with two different surface terminations: the $Ba_{0.5}La_{0.5}O$ surface (work function of 0.99 eV) and the $Ba_{0.5}La_{0.25}Rb_{0.25}O$ surface (work function of 0.79 eV). $Ba_{0.5}La_{0.25}Rb_{0.25}NbO_3$ has a single bulk O *p*-band center value, yet has AO work functions that differ by 0.2 eV. Calculations by Lee *et al.* examining the trends of oxygen reduction and intermediate species' binding energies on perovskite (001) AO and BO_2 surfaces using the O *p*-band center demonstrated that the use of the subsurface O *p*-band center (instead of the bulk value) could resolve the binding energy difference of the AO and BO_2 surfaces for a single perovskite material.[192] A similar approach used to discern work

function differences arising from differences in surface dipoles may work for the materials investigated here, but doing so would lose the advantage of using a bulk descriptor to enable accelerated predictions of work function.

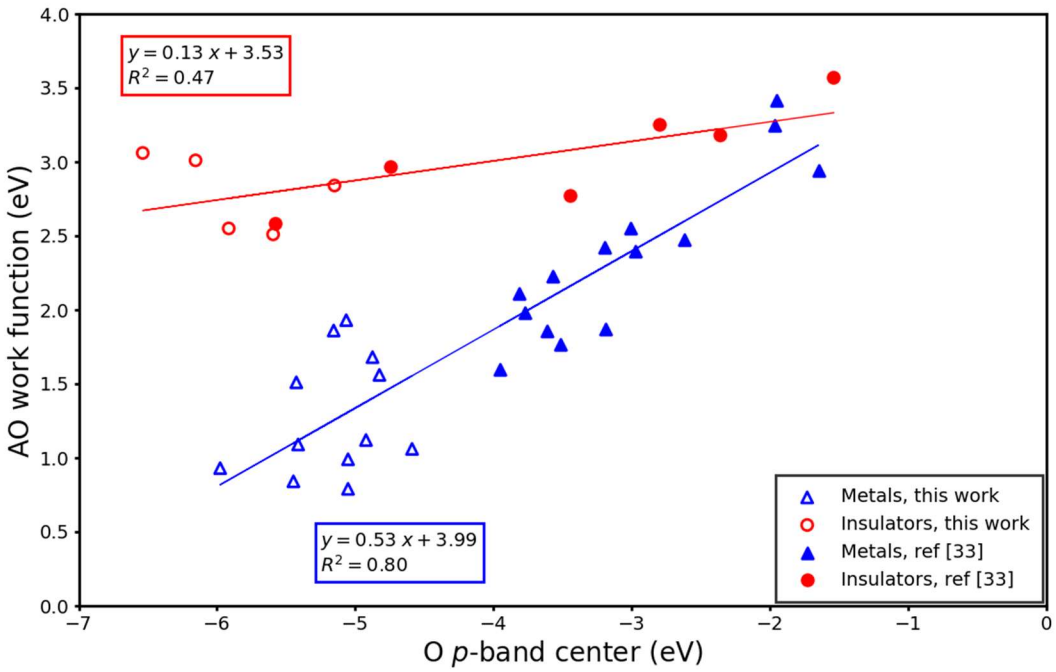

Figure 5.4: Refined correlation of the HSE (001) AO-terminated work functions as a function of bulk HSE O *p*-band center including original data from the work of Jacobs *et al.* (filled red and blue circles),[37] promising materials identified from the screening procedure employed in this chapter (empty red and blue triangles), and select tests of very low O *p*-band center materials predicted from elimination criterion 1 in this chapter (empty red and blue squares).

5.2.7. Materials electronic structure principles to rationalize low and high work function perovskites

Based on the analysis of predicted work function and stability discussed in Section 5.2.3 and shown qualitatively in Figure 5.3, we notice that the number of *d*-band electrons in these perovskites has a significant impact on determining their work functions. Materials with zero *d*-band electrons have a high predicted work function, materials with a low number of *d*-band electrons (less than three but greater than zero) have the lowest work functions,

while materials with higher number of *d*-band electrons (greater than three and less than a full *d*-band of 10) also have high work functions, in the same range as the materials with zero *d*-band electrons. In Figure 5.5 we have taken all of the data from Figure 5.3 and produced a bar chart histogram of the fraction of perovskites with a particular predicted work function, grouped by the number of *d*-band electrons. Figure 5.5 shows that materials with zero *d*-band electrons have the highest average predicted work function of 3.17 eV with a standard deviation 0.13 eV; materials with more than zero but less than or equal to three *d*-band electrons have an average predicted work function of 1.92 eV with a standard deviation of 0.54 eV; materials with more than three but less than or equal to ten *d*-band electrons have an average predicted work function of 2.67 eV with a standard deviation of 0.41 eV, which is qualitatively similar to the results for materials with zero *d*-band electrons. These trends in Figure 5.5 agree with the electronic structure and bonding trends discussed in the work of [37], which discussed the physical basis for these trends from the interplay of bonding ionicity, O *p*-band center position, and the resulting work function value for different types of perovskites. For example, $LaScO_3$ with 0 *d*-band electrons has a high work function, $SrVO_3$ with few *d*-band electrons has a low work function, and $LaNiO_3$ with a nearly full *d*-band also has a high work function.[37]

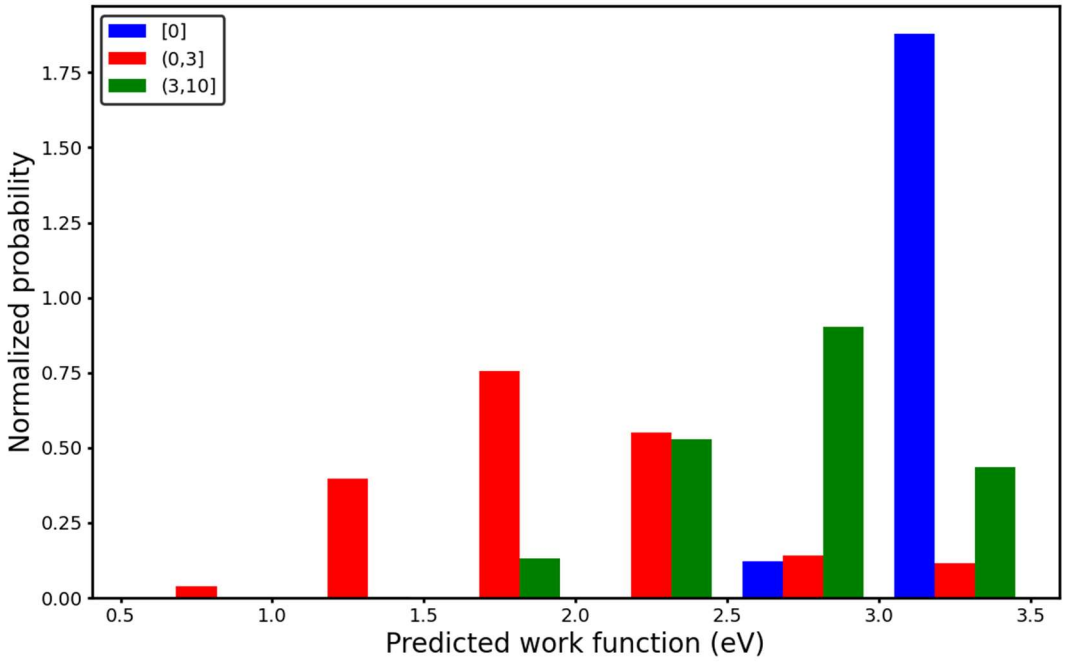

Figure 5.5: Bar chart histogram showing the distribution of predicted work functions, grouped by the number of *d*-band electrons.

5.2.8. Engineering $SrVO_3$ stability and work function through alloying

In this section, we summarize our findings about how different alloy elements affect the stability and predicted work function of $SrVO_3$. We choose to study the effect of alloying on $SrVO_3$ since $SrVO_3$ has been extensively studied previously [38, 40] and is under current experimental investigation.[193], [194] It therefore provides a convenient reference material for additional refined investigations, such as these alloying effects.

Figure 5.6 contains bar plots showing the effect of alloying on the stability and predicted work function when various elements are alloyed on the A-site, B-site, and combined A- and B-sites of $SrVO_3$. From our DFT calculations, the addition of Nb and Ta on the B-site for a range of compositions is expected to enhance the stability, and the alloying of La on the A-site, Nb and Ta on the B-site, and combined alloying of La/Nb and La/Ta on the A-/B-sites is expected to reduce

the work function. Overall, these results suggest that the alloyed systems $SrV_{1-x}Nb_xO_3$, $SrV_{1-x}Ta_xO_3$, as well as these systems doped with La, deserve further exploration as stable, low work function perovskites. We note that recent studies have shown that $SrV_{1-x}Nb_xO_3$ alloys with different Nb content can be synthesized, with promising application as anodes for solid oxide fuel cells.[189], [195]

5.3. Summary and conclusions

In this chapter, our goal is to discover new stable, low work function perovskite compounds for use as thermionic electron emission cathodes using high-throughput DFT methods. From a pool of 2913 compounds, we successively down-select sets of materials that are found have a low predicted work function, be stable under typical thermionic cathode operating conditions, be sufficiently conductive by virtue of a small electronic bandgap, and finally, possess a low work function (001) AO-terminated surface. From our initial pool of about 2913 compounds, 145 compounds are found to have a low predicted work function and be stable under operating conditions. Of these 145 materials, seven of them are found to be sufficiently conductive and have a low work function. These promising materials consist of $SrMoO_3$, $BaMoO_3$, $Sr_{0.5}La_{0.5}MoO_3$, $Ba_{0.25}Ca_{0.75}MoO_3$, $SrNb_{0.75}Co_{0.25}O_3$, $BaZr_{0.375}Ta_{0.5}Fe_{0.125}O_3$, and $BaZr_{0.375}Nb_{0.5}Fe_{0.125}O_3$. These new compounds, together with $SrVO_3$, constitute the set of most promising materials for new thermionic electron emission cathodes for use in high frequency, high power vacuum electronic devices and potentially as emissive layers in thermionic and photon-enhanced thermionic energy converters.

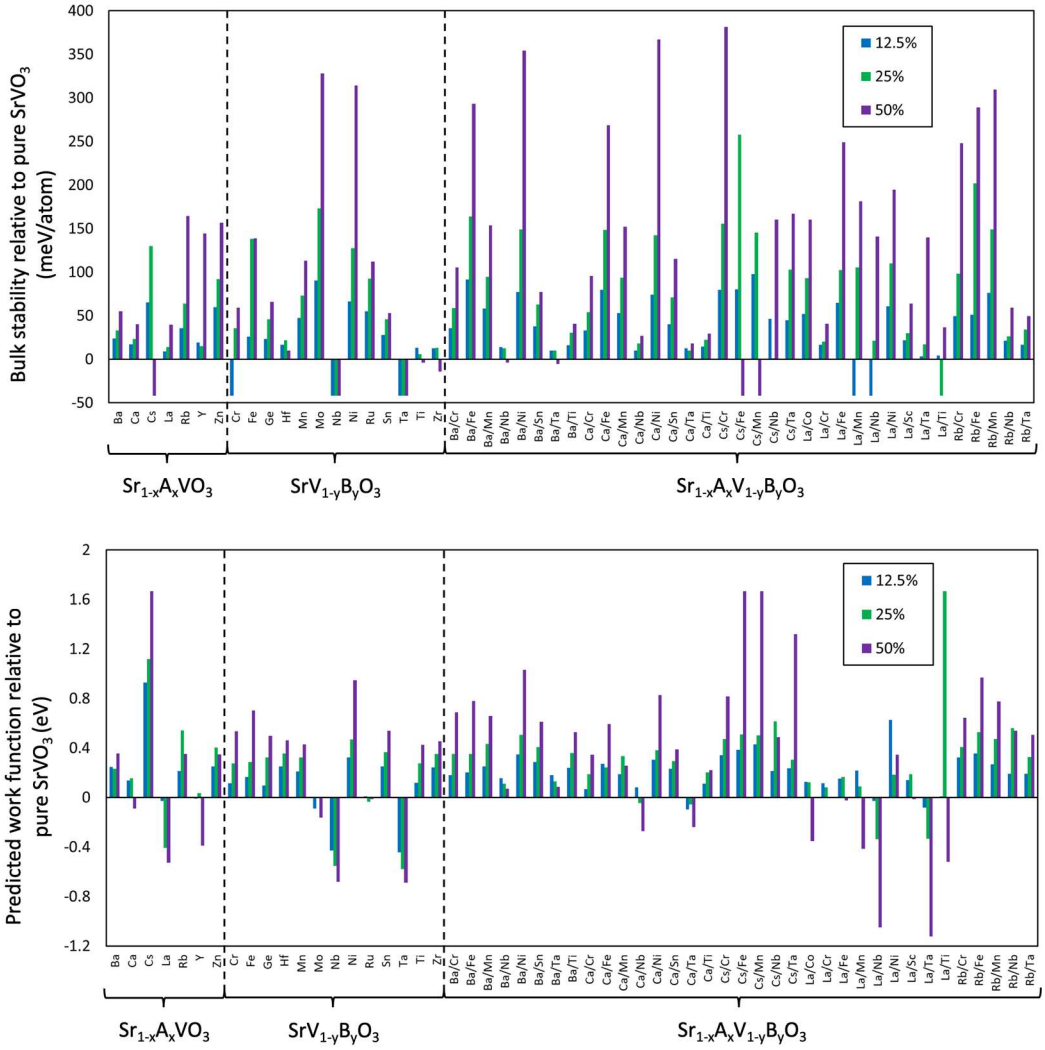

Figure 5.6: Effect of stability and predicted work function from alloying $SrVO_3$ with various dopants on the A-site (e.g. $Sr_{1-x}A_xVO_3$), the B-site (e.g. $SrV_{1-y}B_yO_3$) and both the A- and B-site together (e.g. $Sr_{1-x}A_xV_{1-y}B_yO_3$). In both plots, the blue, green, and purple bars denote site fraction alloying of 12.5%, 25% and 50%, respectively. (a) and (b): alloying effect on stability and work function of $SrVO_3$, respectively. The values of stability and predicted work function are given relative to the pure compound, therefore negative values indicate enhanced stability and reduced work function relative to the unalloyed material.

The large amount of perovskite data analyzed in this chapter enables the understanding of what qualitatively governs the work function of a perovskite based on simple empirical electron counting rules. Here, we found that materials with a small number of electrons (e.g. 1 to 3) in the

d-band tend to result in the lowest predicted work functions, while insulating compounds with 0 *d*-band electrons and materials containing late transition metals with highly occupied *d*-bands tend to result in much higher predicted work functions. These trends in materials chemistry provide a simple foundation for qualitatively identifying whether particular perovskite compounds may be expected to have a low or high work function value for a given application.

This chapter provides a basis for further computational and experimental study of perovskite work functions. Computationally, further study of the promising materials discovered here may involve assessing effects on the stability and work function, such as: cation and oxygen off-stoichiometry, the stability and work function of different surface orientations with and without adsorbed species, and high temperature perovskite structural transitions (e.g. orthorhombic to cubic transitions). Experimentally, the synthesis, characterization, work function measurement and high temperature emission properties of the promising materials discovered here is critical to assessing the quality of these materials as thermionic electron emitters. Finally, the expanded data set of HSE-level perovskite work function calculations in this study may find use in design of perovskite heterojunctions where knowledge of electronic band offsets and dipole engineering approaches are critical.

6. Concluding remarks

6.1. Summary

The research contained in chapter 3 through chapter 5 regarding DFT-calculated work function values and work function trends for rare-earth hexaborides, rare-earth tetraborides, transition metal nitrides (TMNs), and perovskite oxides is summarized in this section.

In this dissertation, we have established a systematic work function dataset for hexaborides, tetraborides, and TMNs, the work function trends of these compounds can be understood based on atomic properties such as electronegativity and atomic radius. We have benchmarked the accuracy of DFT-calculated work function for $SrTiO_3$ and have suggested best practices for using DFT to obtain work functions of complex oxides. We also investigated the effect of common surface features on oxide work function. Through our work, we proposed $La_xBa_{1-x}B_6$, HfN, and seven perovskites as promising cathode materials with low work functions.

6.2. Future directions

6.2.1. Data-driven method of predicting work function

Xiong *et al.* examined over 1000 perovskites and identified the factors that determine their work functions using machine learning analysis. [176] They used atomic properties of each element as input features. From our works, it is obvious that the work function is highly dependent on surface geometry, which is determined by all surface atoms. To better utilize the correlation between the work function and surface geometry, explicitly adding combinations of atomic descriptors of all surface atoms which are relevant to the surface relaxation (e.g., the difference in atomic radius of A and B atoms) to the input features may enhance the machine learning model. Such combinations can be manually determined according to physical intuitions, or can be

identified by another machine learning task which performs regression on surface geometry parameters (e.g. deviations between surface and bulk atoms). With our data set of nearly 3000 perovskites, such task should not be difficult.

6.2.2. Quantitative surface dipole calculations

Surface dipole can directly modulate the work function, in our works, we have qualitatively analyzed surface dipole based on the electronegativity and atomic radius of the surface atoms. However, a quantitative surface dipole would be more helpful to analyze and understand work function trends in different materials or in various terminations of the same material. A commonly adopted equation to calculate the surface dipole of a slab is

$$p = \int_{z_0}^{c/2} z\rho_t(z)\mathrm{d}z \tag{6.1}$$

where $\rho_t(z)$ is the average charge density over xy plane, $c/2$ is the center of the vacuum region, and z_0 is the midpoint between the first two layers that are deep in the bulk. Although the choice of z_0 is somewhat arbitrary, the surface dipole change calculated from this equation is independent of z_0 and should be accurate:

$$\Delta p = \int_{z_0}^{c/2} z\Delta\rho_t(z)\mathrm{d}z \tag{6.2}$$

As long as the number of electrons is conserved:

$$\int_{z_0}^{c/2} \Delta\rho_t(z)\mathrm{d}z = 0 \tag{6.3}$$

Equation 6.1 has been used to calculate the surface dipoles of strained W (001) surface with a monolayer of different types of atoms, and showed good consistency with the work function trends.[196] Probably it is worthy testing if this equation can also be applied to complex oxides.

6.2.3. Other surfaces and terminations

In our works, we mainly focused on (001)-AO terminated perovskites. And although we performed stability analyses based on bulk calculations, we lacked thermodynamics of different surfaces and terminations. Since polycrystals are generally easier to fabricate, and sometimes it is difficult to make a cathode of special shape from single crystal material (e.g., the hollow cylindrical cathode in magnetron), it would be helpful to calculate the stability of different surfaces/terminations and corresponding work functions, and make predictions based on comprehensive evaluations of all terminations.

6.2.4. Defected and reconstructed surfaces

For ideal surfaces, (001)-AO termination has lower work function than (001)-BO_2 termination due to positive surface dipole. But surface dipole, and thus the work function, is highly sensitive to surface conditions. From chapter 4 we can see, after introducing defects, such order can be reversed (SrO termination with Sr vacancies has higher work function than TiO_2 termination with Sr adatoms); and surface reconstructions can also significantly alter the work function. Therefore, calculations on defected and reconstructed surfaces would greatly improve DFT predicted emission performance. However, determining possible surface defects and reconstructions solely from DFT calculations requires a large number of calculations. More targeted calculations based on experimental surface characterizations may be a practical way.

6.2.5. Experimental investigations on promising candidates

Since we have proposed several promising low work function materials, further work can be focused on the synthesis and characterization of those materials. And the feedbacks from experimental results can be used to guide on more targeted calculations of possible defects, reconstructions, and other terminations.

References

[1] R. H. Fowler and L. Nordheim, "Electron Emission in Intense Electric Fields," *Proc. R. Soc. A Math. Phys. Eng. Sci.*, vol. 119, no. 781, pp. 173–181, May 1928.

[2] C. Herring and M. H. Nichols, "Thermionic Emission," *Rev. Mod. Phys.*, vol. 21, no. 2, p. 185, 1949.

[3] D. R. Whaley, B. M. Gannon, V. O. Heinen, K. E. Kreischer, C. E. Holland, and C. A. Spindt, "Experimental demonstration of an emission-gated traveling-wave tube amplifier," *IEEE Trans. Plasma Sci.*, vol. 30, no. 3 I, pp. 998–1008, 2002.

[4] E. A. Gelvich, L. M. Borisov, Y. V Zhary, D. Zakurdayev, A. S. Pobedonostsev, and V. I. Poognin, "The New Generation of High-Power Multiple-Beam Klystrons," *IEEE Trans. Microw. Theory Tech.*, vol. 41, no. 9204035, pp. 15–19, 1993.

[5] M. Y. Glyavin, A. G. Luchinin, and G. Y. Golubiatnikov, "Generation of 1 . 5-kW , 1-THz Coherent Radiation from a Gyrotron with a Pulsed Magnetic Field," *Phys. Rev. Lett.*, vol. 100, pp. 1–3, 2008.

[6] S. Gilmour, *Principles of Traveling Wave Tubes*. Boston: Artech House, 1994.

[7] J. H. Booske, "Plasma physics and related challenges of millimeter-wave-to-terahertz and high power microwave generation," *Phys. Plasmas*, vol. 15, no. 5, p. 055502, 2008.

[8] S. Yamamoto, "Fundamental physics of vacuum electron sources," *Reports Prog. Phys.*, vol. 69, no. 1, p. 181, 2005.

[9] D. M. Kirkwood *et al.*, "Frontiers in Thermionic Cathode Research," *IEEE Trans. Electron Devices*, vol. 65, no. 6, pp. 2061–2071, 2018.

[10] E. S. Rittner, W. C. Rutledge, and R. H. Ahlert, "On the Mechanism of Operation of the Barium Aluminate Impregnated Cathode," *J. Appl. Phys.*, vol. 28, p. 1468, 1957.

[11] V. Vlahos, J. H. Booske, and D. Morgan, "Ab initio investigation of barium-scandium-oxygen coatings on tungsten for electron emitting cathodes," *Phys. Rev. B*, vol. 81, no. 5, p. 054207, 2010.

[12] A. Taran, D. Voronovich, S. Plankovskyy, V. Paderno, and V. Filipov, "Review of LaB6, Re-W dispenser, and BaHfO3-W cathode development," *IEEE Trans. Electron Devices*, vol. 56, no. 5, pp. 812–817, 2009.

[13] J. M. Lafferty, "Boride cathodes," *J. Appl. Phys.*, vol. 22, no. 3, pp. 299–309, Mar. 1951.

[14] R. Nishitani *et al.*, "Surface structures and work functions of the LaB6 (100), (110) and (111) clean surfaces," *Surf. Sci.*, vol. 93, no. 2–3, pp. 535–549, Mar. 1980.

[15] L. W. Swanson, M. A. Gesley, and P. R. Davis, "Crystallographic dependence of the work function and volatility of LaB6," *Surf. Sci.*, vol. 107, no. 1, pp. 263–289, May 1981.

[16] L. W. Swanson and T. Dickinson, "Single-crystal work-function and evaporation

measurements of LaB6," *Appl. Phys. Lett.*, vol. 28, no. 10, pp. 578–580, May 1976.

[17] H. Ahmed and A. N. Broers, "Lanthanum hexaboride electron emitter," *J. Appl. Phys.*, vol. 43, no. 5, pp. 2185–2192, May 1972.

[18] K. Harada, H. Nagata, and R. Shimizu, "〈310〉 Single-Crystal LaB6 as Thermal Field Emitter of High Brightness Electron Source," *J. Electron Microsc. (Tokyo).*, vol. 40, no. 1, pp. 1–4, Feb. 1991.

[19] N. Mita, "Degradation of Coated Impregnated Cathode's Surface Coating," *IEEE Trans. Electron Devices*, vol. 38, no. November, pp. 2554–2557, 1991.

[20] G. Gartner and P. Geittner, "Emission properties of top-layer scandate cathodes prepared by LAD," *Appl. Surf. Sci.*, vol. 111, pp. 11–17, 1997.

[21] Y. Wang, J. Wang, W. Liu, X. Zhang, and L. Li, "Emission mechanism of high current density scandia-doped dispenser cathodes Emission mechanism of high current density scandia-doped dispenser," *J. Vac. Sci. Technol. B*, vol. 29, p. 1, 2011.

[22] Y. Wang, J. Wang, W. Liu, L. Li, Y. Wang, and X. Zhang, "Correlation Between Emission Behavior and Surface Features of Scandate Cathodes," *IEEE Trans. Electron Devices*, vol. 56, no. 5, pp. 776–785, May 2009.

[23] Q. Zheng *et al.*, "Single-phase (Ba,Ca)2ScAlO5 impregnant for dispenser cathodes with enhanced thermionic emission performance," *Ceram. Int.*, vol. 47, no. 2, pp. 1632–1639, Jan. 2021.

[24] B. Vancil, W. L. Ohlinger, M. C. Green, C. Osborne, V. Schmidt, and A. Vancil, "New Findings on Powder Synthesis for Scandate Cathode Matrices," *IEEE Trans. Electron Devices*, vol. 65, no. 6, pp. 2077–2082, 2018.

[25] J. M. Roquais, F. Poret, R. Le Doze, J. L. Ricaud, A. Monterrin, and A. Steinbrunn, "Barium depletion study on impregnated cathodes and lifetime prediction," *Appl. Surf. Sci.*, vol. 215, no. 1–4, pp. 5–17, 2003.

[26] G. Gaertner and D. Barratt, "Life-limiting mechanisms in Ba-oxide, Ba-dispenser and Ba-Scandate cathodes," *Appl. Surf. Sci.*, vol. 251, no. 1–4, pp. 73–79, 2005.

[27] R. Advani *et al.*, "Experimental investigation of a 140-GHz coaxial gyrotron oscillator," *IEEE Trans. Plasma Sci.*, vol. 29, no. 6, pp. 943–950, Dec. 2001.

[28] J. P. Anderson, S. E. Korbly, R. J. Temkin, M. A. Shapiro, K. L. Felch, and S. Cauffman, "Design and emission uniformity studies of a 1.5-MW gyrotron electron gun," *IEEE Trans. Plasma Sci.*, vol. 30, no. 6, pp. 2117–2123, Dec. 2002.

[29] S. Sasaki, T. Yaguchi, Y. Nonaka, S. Taguchi, and M. Shibata, "Surface coating influence on scandate cathode performance," *Appl. Surf. Sci.*, vol. 195, no. May, pp. 214–221, 2002.

[30] J. Wang, L. Li, W. Liu, Y. Wang, Y. Wang, and M. Zhou, "Sc2O3–W matrix impregnated cathode with spherical grains," *J. Phys. Chem. Solids*, vol. 69, pp. 2103–2108, 2008.

[31] B. Vancil, I. Brodie, J. Lorr, and V. Schmidt, "Scandate dispenser cathodes with sharp

transition and their application in microwave tubes," *IEEE Trans. Electron Devices*, vol. 61, no. 6, pp. 1754–1759, 2014.

[32] R. M. Jacobs, J. H. Booske, and D. Morgan, "Electron Emission Energy Barriers and Stability of Sc 2 O 3 with Adsorbed Ba and Ba−O," *J. Phys. Chem. C*, vol. 118, no. 34, pp. 19742–19758, 2014.

[33] Q. Zhou, X. Liu, T. Maxwell, B. Vancil, T. J. Balk, and M. J. Beck, "Ba x Sc y O z on W (0 0 1), (1 1 0), and (1 1 2) in scandate cathodes: Connecting to experiment via μ O and equilibrium crystal shape," *Appl. Surf. Sci.*, vol. 458, pp. 827–838, Nov. 2018.

[34] R. Jacobs, D. Morgan, and J. Booske, "Work function and surface stability of tungsten-based thermionic electron emission cathodes Work function and surface stability of tungsten-based thermionic electron emission cathodes," *APL Mater.*, vol. 5, p. 116105, 2017.

[35] Q. Zhou, T. J. Balk, M. J. Beck, Q. Zhou, T. J. Balk, and M. J. Beck, "Interplay of composition , structure , and electron density of states in W-Os cathode materials and relationship with thermionic emission," *J. Vac. Sci. Technol. A*, vol. 35, p. 021601, 2017.

[36] M. A. Peña and J. L. G. Fierro, "Chemical structures and performance of perovskite oxides," *Chem. Rev.*, vol. 101, no. 7, pp. 1981–2017, 2001.

[37] R. Jacobs, J. Booske, and D. Morgan, "Understanding and Controlling the Work Function of Perovskite Oxides Using Density Functional Theory," *Adv. Funct. Mater.*, vol. 26, no. 30, pp. 5471–5482, 2016.

[38] Z. Zhong and P. Hansmann, "Tuning the work function in transition metal oxides and their heterostructures," *Phys. Rev. B*, vol. 93, p. 235116, 2016.

[39] J. A. Moyer, C. Eaton, and R. Engel-herbert, "Highly Conductive SrVO3 as a Bottom Electrode for Functional Perovskite Oxides," *Adv. Mater.*, vol. 25, pp. 3578–3582, 2013.

[40] S. Hui and A. Petric, "Conductivity and stability of SrVO3 and mixed perovskites at low oxygen partial pressures," *Solid State Ionics*, vol. 143, no. 3–4, pp. 275–283, Jul. 2001.

[41] R. J. Temkin, "Vacuum electron devices for applications in 'big science,'" in *2006 IEEE International Vacuum Electronics Conference held jointly with 2006 IEEE International Vacuum Electron Sources, IVEC/IVESC 2006*, 2006, pp. 7–10.

[42] J. W. Schwede *et al.*, "Photon-enhanced thermionic emission from heterostructures with low interface recombination," *Nat. Commun.*, vol. 4, no. 1, pp. 1–6, 2013.

[43] J. W. Schwede *et al.*, "Photon-enhanced thermionic emission for solar concentrator systems," *Nat. Mater.*, vol. 9, no. 9, p. 762, 2010.

[44] G. Greczynski and L. Hultman, "Compromising Science by Ignorant Instrument Calibration—Need to Revisit Half a Century of Published XPS Data," *Angew. Chemie*, vol. 132, no. 13, pp. 5034–5038, Mar. 2020.

[45] O. W. Richardson, *The emission of electricity from hot bodies*. Longmans, Green and Company, 1921.

[46] C. D. Child, “Discharge from hot CaO,” *Phys. Rev. (Series I)*, vol. 32, no. 5, pp. 492–511, May 1911.

[47] I. Langmuir, “The effect of space charge and initial velocities on the potential distribution and thermionic current between parallel plane electrodes,” *Phys. Rev.*, vol. 21, no. 4, pp. 419–435, Apr. 1923.

[48] G. A. Kudintseva, G. M. Kuznetsova, V. P. Bondarenko, N. F. Selivanova, and V. Y. Shlyuko, “Preparation and emissive properties of some yttrium and gadolinium borides,” *Sov. Powder Metall. Met. Ceram.*, vol. 7, no. 2, pp. 115–120, Feb. 1968.

[49] M. M. Hasan, D. Cuskelly, H. Sugo, and E. H. Kisi, “Low temperature synthesis of low thermionic work function (LaxBa1-x)B6,” *J. Alloys Compd.*, vol. 636, pp. 67–72, Jul. 2015.

[50] V. S. Fomenko, *Handbook of Thermionic Properties*, 1st ed. Springer, Boston, MA, 1966.

[51] X. Lu, Q. Yang, W. Chen, C. Xiao, and A. Hirose, “Field electron emission characteristics of diamond films with different grain morphologies,” *J. Vac. Sci. Technol. B Microelectron. Nanom. Struct.*, vol. 24, no. 6, p. 2575, Oct. 2006.

[52] S. Klassen, “The Photoelectric Effect: Reconstructing the Story for the Physics Classroom,” *Science and Education*, vol. 20, no. 7. Springer, pp. 719–731, 10-Jul-2011.

[53] D. Cahen and A. Kahn, “Electron Energetics at Surfaces and Interfaces: Concepts and Experiments,” *Adv. Mater.*, vol. 15, no. 4, pp. 271–277, Feb. 2003.

[54] M. Born and R. Oppenheimer, “Zur Quantentheorie der Molekeln,” *Ann. Phys.*, vol. 389, no. 20, pp. 457–484, Jan. 1927.

[55] E. Schrödinger, “An undulatory theory of the mechanics of atoms and molecules,” *Phys. Rev.*, vol. 28, no. 6, pp. 1049–1070, Dec. 1926.

[56] P. Hohenberg and W. Kohn, “Inhomogeneous electron gas,” *Phys. Rev.*, vol. 136, no. 3B, p. B864, Nov. 1964.

[57] W. Kohn and L. J. Sham, “Self-consistent equations including exchange and correlation effects,” *Phys. Rev.*, vol. 140, no. 4A, p. A1133, Nov. 1965.

[58] J. P. Perdew, K. Burke, and Y. Wang, “Generalized gradient approximation for the exchange-correlation hole of a many-electron system,” *Phys. Rev. B*, vol. 54, no. 23, pp. 16533–16539, Dec. 1996.

[59] J. P. Perdew, K. Burke, and M. Ernzerhof, “Generalized Gradient Approximation Made Simple,” *Phys. Rev. Lett.*, vol. 77, no. 18, p. 3865, 1996.

[60] A. Janotti and C. G. Van De Walle, “Fundamentals of zinc oxide as a semiconductor,” *Reports Prog. Phys.*, vol. 72, no. 12, p. 126501, Oct. 2009.

[61] C. G. Van De Walle and J. Neugebauer, “First-principles calculations for defects and impurities: Applications to III-nitrides,” *Journal of Applied Physics*, vol. 95, no. 8. American Institute of PhysicsAIP, pp. 3851–3879, 15-Apr-2004.

[62] A. Janotti, D. Segev, and C. G. Van De Walle, “Effects of cation d states on the structural and electronic properties of III-nitride and II-oxide wide-band-gap semiconductors,” *Phys. Rev. B*, vol. 74, no. 4, p. 045202, Jul. 2006.

[63] J. L. Lyons, A. Janotti, and C. G. Van De Walle, “Why nitrogen cannot lead to p -type conductivity in ZnO,” *Appl. Phys. Lett.*, vol. 95, no. 25, p. 252105, Dec. 2009.

[64] V. I. Anisimov, F. Aryasetiawan, and A. I. Lichtenstein, “First-principles calculations of the electronic structure and spectra of strongly correlated systems: The LDA+U method,” *J. Phys. Condens. Matter*, vol. 9, no. 4, pp. 767–808, 1997.

[65] J. Heyd, G. E. Scuseria, and M. Ernzerhof, “Hybrid functionals based on a screened Coulomb potential,” *J. Chem. Phys.*, vol. 118, no. 18, pp. 8207–8215, May 2003.

[66] A. Alkauskas, P. Broqvist, and A. Pasquarello, “Defect energy levels in density functional calculations: Alignment and band gap problem,” *Phys. Rev. Lett.*, vol. 101, no. 4, p. 046405, Jul. 2008.

[67] P. Deák, B. Aradi, T. Frauenheim, E. Janzén, and A. Gali, “Accurate defect levels obtained from the HSE06 range-separated hybrid functional,” *Phys. Rev. B*, vol. 81, no. 15, p. 153203, Apr. 2010.

[68] H. P. Komsa and A. Pasquarello, “Assessing the accuracy of hybrid functionals in the determination of defect levels: Application to the As antisite in GaAs,” *Phys. Rev. B*, vol. 84, no. 7, p. 075207, Aug. 2011.

[69] E. Fermi, “Sulla quantizzazione del gas perfetto monoatomico,” *Rend. Lincei*, vol. 145, 1926.

[70] P. A. M. Dirac, “On the theory of quantum mechanics,” *Proc. R. Soc. London. Ser. A, Contain. Pap. a Math. Phys. Character*, vol. 112, no. 762, pp. 661–677, Oct. 1926.

[71] G. Kresse and J. Furthmüller, “Software VASP, vienna (1999),” *Phys. Rev. B*, vol. 54, no. 11, p. 169, 1996.

[72] C. J. Fall, N. Binggeli, and A. Baldereschi, “Deriving accurate work functions from thin-slab calculations,” *J. Phys. Condens. Matter*, vol. 11, pp. 2689–2696, 1999.

[73] S. De Waele, K. Lejaeghere, M. Sluydts, and S. Cottenier, “Error estimates for density-functional theory predictions of surface energy and work function,” *Phys. Rev. B*, vol. 94, p. 235418, 2016.

[74] R. Tran, X.-G. Li, J. H. Montoya, D. Winston, K. A. Persson, and S. P. Ong, “Anisotropic work function of elemental crystals,” *Surf. Sci.*, vol. 687, pp. 48–55, 2019.

[75] M. Uijttewaal, G. De Wijs, and R. De Groot, “Ab Initio and Work Function and Surface Energy Anisotropy of LaB 6,” *J. Phys. Chem. B*, vol. 110, no. 37, pp. 18459–18465, 2006.

[76] K. M. Schmidt, S. T. Misture, O. A. Graeve, and V. R. Vasquez, “Metal Hexaboride Work Functions: Surface Configurations and the Electrical Double Layer from First-Principles,” *Adv. Electron. Mater.*, vol. 5, no. 3, p. 1800074, Mar. 2019.

[77] M. G. Quesne, A. Roldan, N. H. De Leeuw, and C. R. A. Catlow, “Bulk and surface properties of metal carbides: Implications for catalysis,” *Phys. Chem. Chem. Phys.*, vol. 20, no. 10, pp. 6905–6916, Mar. 2018.

[78] Z. Zhong and P. Hansmann, “Tuning the work function in transition metal oxides and their heterostructures,” *Phys. Rev. B*, vol. 93, no. 23, pp. 1–9, 2016.

[79] S. A. Chambers and P. V. Sushko, “Influence of crystalline order and defects on the absolute work functions and electron affinities of Ti O2 - And SrO-terminated n-SrTi O3(001),” *Phys. Rev. Mater.*, vol. 3, no. 12, p. 125803, Dec. 2019.

[80] B. Wang, S. Günther, J. Wintterlin, and M. L. Bocquet, “Periodicity, work function and reactivity of graphene on Ru(00001) from first principles,” *New J. Phys.*, vol. 12, no. 4, p. 043041, Apr. 2010.

[81] G. Giovannetti, P. A. Khomyakov, G. Brocks, V. M. Karpan, J. Van Den Brink, and P. J. Kelly, “Doping graphene with metal contacts,” *Phys. Rev. Lett.*, vol. 101, no. 2, p. 026803, Jul. 2008.

[82] N. Erdman, O. Warschkow, M. Asta, K. R. Poeppelmeier, D. E. Ellis, and L. D. Marks, “Surface Structures of SrTiO 3 (001): A TiO 2-rich Reconstruction with a c(4 × 2) Unit Cell,” *J. Am. Chem. Soc.*, vol. 125, no. 33, pp. 10050--10056, 2003.

[83] N. Erdman, K. R. Poeppelmeier, M. Asta, O. Warschkow, D. E. Ellis, and L. D. Marks, “The structure and chemistry of the TiO 2-rich surface of SrTiO 3 (001),” *Nature*, vol. 419, no. 6902, p. 55, 2002.

[84] Y. Lin, A. E. Becerra-Toledo, F. Silly, K. R. Poeppelmeier, M. R. Castell, and L. D. Marks, “The (2 × 2) reconstructions on the SrTiO3 (001) surface: A combined scanning tunneling microscopy and density functional theory study,” *Surf. Sci.*, vol. 605, no. 17–18, pp. L51–L55, Sep. 2011.

[85] J. M. P. Martirez, E. H. Morales, W. A. Saidi, D. A. Bonnell, and A. M. Rappe, “Atomic and Electronic Structure of the BaTiO 3 (001)(5$\times$ 5) R 26.6° Surface Reconstruction,” *Phys. Rev. Lett.*, vol. 109, no. 25, p. 256802, 2012.

[86] T. Kubo and H. Nozoye, “Surface Structure of SrTiO 3,” *Phys. Rev. Lett.*, vol. 86, no. 9, p. 1801, 2001.

[87] T. Ma, R. Jacobs, J. Booske, and D. Morgan, “Understanding the interplay of surface structure and work function in oxides: A case study on SrTiO3,” *APL Mater.*, vol. 8, no. 7, p. 071110, Jul. 2020.

[88] A. V. Krukau, O. A. Vydrov, A. F. Izmaylov, and G. E. Scuseria, “Influence of the exchange screening parameter on the performance of screened hybrid functionals,” *J. Chem. Phys.*, vol. 125, no. 22, 2006.

[89] G. Kresse and D. Joubert, “From ultrasoft pseudopotentials to the projector augmented-wave method,” *Phys. Rev. B*, vol. 59, no. 3, pp. 1758–1775, 1999.

[90] H. J. Monkhorst and J. D. Pack, “Special points for Brillouin-zone integrations,” *Phys.*

Rev. B, vol. 13, no. 12, p. 5188, 1976.

[91] A. Jain *et al.*, “Commentary: The Materials Project: A materials genome approach to accelerating materials innovation,” *APL Mater.*, vol. 1, no. 1, p. 011002, 2013.

[92] C. Franchini, “Hybrid functionals applied to perovskites,” *J. Phys. Condens. Matter*, vol. 26, no. 25, p. 253202, Jun. 2014.

[93] J. He and C. Franchini, “Screened hybrid functional applied to 3d0 → 3d8 transition-metal perovskites LaMO3 (M=Sc–Cu): Influence of the exchange mixing parameter on the structural, electronic, and magnetic properties,” *Phys. Rev. B*, vol. 86, p. 235117, 2012.

[94] R. Jacobs, T. Mayeshiba, J. Booske, and D. Morgan, “Material Discovery and Design Principles for Stable, High Activity Perovskite Cathodes for Solid Oxide Fuel Cells,” *Adv. Energy Mater.*, vol. 8, no. 11, pp. 1–27, 2018.

[95] T. Yorisaki, A. Tillekaratne, Y. Moriya, C. Oshima, S. Otani, and M. Trenary, “Vibrational spectroscopy of oxygen on the (100) and (111) surfaces of lanthanum hexaboride,” *Surf. Sci.*, vol. 604, no. 13–14, pp. 1202–1207, Jul. 2010.

[96] T. Nagaki, Y. Inoue, I. Kojima, and I. Yasumori, “Catalytic activity of lanthanum hexaboride for hydrogen-deuterium equilibration,” *J. Phys. Chem.*, vol. 84, no. 15, pp. 1919–1925, 1980.

[97] J. S. Ozcomert and M. Trenary, “Atomically resolved surface structure of LaB6(100),” *Surf. Sci.*, vol. 265, no. 1–3, pp. L227–L232, Apr. 1992.

[98] N. Yamamoto *et al.*, “Oxygen adsorption sites on the PrB6(100) and LaB6(100) surfaces,” *Surf. Sci.*, vol. 348, no. 1–2, pp. 133–142, Mar. 1996.

[99] N. Tadaaki, K. Kazuo, I. Yoshitaka, O. Chuhei, and S. Otani, “Surface phonons of LaB6(100): deformation of boron octahedra at the surface,” *Surf. Sci.*, vol. 290, no. 3, pp. 436–444, Jun. 1993.

[100] Y. Gotoh, H. Tsuji, and J. Ishikawa, “Measurement of work function of transition metal nitride and carbide thin films,” *J. Vac. Sci. Technol. B Microelectron. Nanom. Struct. Process.*, vol. 21, p. 1607, 2003.

[101] G. M. Matenoglou, L. E. Koutsokeras, and P. Patsalas, “Plasma energy and work function of conducting transition metal nitrides for electronic applications,” *Appl. Phys. Lett*, vol. 94, p. 152108, 2009.

[102] I. S. Sokolovi´c, M. Schmid, U. Diebold, and M. Setvin, “Incipient ferroelectricity: A route towards bulk-terminated ${\rm SrTiO}_3$,” *Phys. Rev. Mater.*, vol. 3, p. 34407, 2019.

[103] T. Susaki, N. Shigaki, K. Matsuzaki, and H. Hosono, “Work function modulation in MgO/Nb: SrTiO3 by utilizing highly nonequilibrium thin-film growth,” *Phys. Rev. B*, vol. 90, no. 3, p. 035453, 2014.

[104] T. Susaki, A. Makishima, and H. Hosono, “Work function engineering via LaAlO3/SrTiO3 polar interfaces,” *Phys. Rev. B*, vol. 84, no. 11, p. 115456, 2011.

[105] T. Susaki, A. Makishima, and H. Hosono, “Tunable work function in MgO/Nb:SrTiO3 surfaces studied by Kelvin probe technique,” *Phys. Rev. B*, vol. 83, no. 11, p. 115435, 2011.

[106] M. Riva *et al.*, “Influence of surface atomic structure demonstrated on oxygen incorporation mechanism at a model perovskite oxide,” *Nat. Commun.*, vol. 9, no. 1, p. 3710, 2018.

[107] L. Gaines, *Insoluble Monolayers at Liquid-Gas Interfaces*. New York: Wiley-Interscience, 1966.

[108] J. Hölzl and F. K. Schülte, *Work Function of Metals*. Berlin: Springer-Verlag, 1979.

[109] S. Ping Ong *et al.*, “Python Materials Genomics (pymatgen): A robust, open-source python library for materials analysis,” *Comput. Mater. Sci.*, vol. 68, pp. 314–319, 2013.

[110] R. Jacobs, B. Zheng, B. Puchala, P. M. Voyles, A. B. Yankovich, and D. Morgan, “Counterintuitive Reconstruction of the Polar O-Terminated ZnO Surface with Zinc Vacancies and Hydrogen,” *J. Phys. Chem. Lett*, vol. 7, p. 45, 2016.

[111] R. M. Jacobs, J. H. Booske, and D. Morgan, “Intrinsic defects and conduction characteristics of Sc2O3 in thermionic cathode systems,” *Phys. Rev. B*, vol. 86, no. 5, p. 054106, 2012.

[112] J. T. Cahill and O. A. Graeve, “Hexaborides: A review of structure, synthesis and processing,” *Journal of Materials Research and Technology*, vol. 8, no. 6. Elsevier Editora Ltda, pp. 6321–6335, 01-Nov-2019.

[113] J. M. Lafferty, “Boride Cathodes,” *J. Appl. Phys.*, vol. 22, no. 3, pp. 299–309, Mar. 1951.

[114] A. N. Broers, “Some experimental and estimated characteristics of the lanthanum hexaboride rod cathode electron gun,” *J. Phys. E.*, vol. 2, no. 3, pp. 273–276, Mar. 1969.

[115] L. W. Swanson, M. A. Gesley, and P. R. Davis, “Crystallographic dependence of the work function and volatility of LaB6,” *Surf. Sci.*, vol. 107, no. 1, pp. 263–289, May 1981.

[116] T. Aida, Y. Honda, S. Yamamoto, and U. Kawabe, “Preparation, vapor pressure, and thermionic emission properties of BaB 6 powder,” *J. Appl. Phys.*, vol. 52, p. 1022, 1981.

[117] P. R. Davis, M. A. Gesley, G. A. Schwind, L. W. Swanson, and J. J. Hutta, “Comparison of thermionic cathode parameters of low index single crystal faces of LaB6, CeB6 and PrB6,” *Appl. Surf. Sci.*, vol. 37, no. 4, pp. 381–394, 1989.

[118] R. W. Decker and D. W. Stebbins, “Photoelectric Work Functions of the Borides of Lanthanum, Praseodymium, and Neodymium,” *J. Appl. Phys.*, vol. 26, p. 1004, 1955.

[119] G. V. Samsonov, A. I. Kondrashov, L. N. Okhremchuk, I. A. Podchernyaeva, N. I. Siman, and V. S. Fomenko, “Thermionic emission from complex alloys containing lanthanum hexaboride,” *Sov. Powder Metall. Met. Ceram.*, vol. 16, no. 1, pp. 16–22, Jan. 1977.

[120] L. W. Swanson and D. R. McNeely, “Work functions of the (001) face of the hexaborides of Ba, La, Ce and Sm,” *Surf. Sci.*, vol. 83, no. 1, pp. 11–28, Apr. 1979.

[121] M. Futamoto, M. Nakazawa, and U. Kawabe, “Thermionic emission properties of hexaborides,” *Surf. Sci.*, vol. 100, no. 3, pp. 470–480, Nov. 1980.

[122] W. Waldhauser, C. Mitterer, J. Laimer, and H. Störi, “Sputtered thermionic hexaboride coatings,” *Surf. Coatings Technol.*, vol. 98, no. 1–3, pp. 1315–1323, Jan. 1998.

[123] T. C. Back *et al.*, “Work function characterization of directionally solidified LaB6–VB2 eutectic,” *Ultramicroscopy*, vol. 183, pp. 1339–1351, Dec. 2017.

[124] G. Gärtner, P. Geittner, H. Lydtin, and A. Ritz, “Emission properties of top-layer scandate cathodes prepared by LAD,” *Appl. Surf. Sci.*, vol. 111, pp. 11–17, Feb. 1997.

[125] S. Yamamoto, S. Taguchi, I. Watanabe, and S. Kawase, “ Impregnated cathode coated with tungsten thin film containing Sc 2 O 3 ,” *J. Vac. Sci. Technol. A Vacuum, Surfaces, Film.*, vol. 5, no. 4, pp. 1299–1302, Jul. 1987.

[126] S. Taguchi, T. Aida, and S. Yamamoto, “Investigation of Sc2O3 Mixed-Matrix Ba-Ca Aluminate-Impregnated Cathodes,” *IEEE Trans. Electron Devices*, vol. 31, no. 7, pp. 900–903, 1984.

[127] R. Forman, “A proposed physical model for the impregnated tungsten cathode based on Auger surface studies of the Ba-O-W system,” *Appl. Surf. Sci.*, vol. 2, no. 2, pp. 258–274, Jan. 1979.

[128] G. A. Haas, A. Shih, and C. R. K. Marrian, “Interatomic Auger analysis of the oxidation of thin Ba films. II. Applications to impregnated cathodes,” *Appl. Surf. Sci.*, vol. 16, no. 1–2, pp. 139–162, May 1983.

[129] S. Yamamoto, I. Watanabe, S. Sasaki, and T. Yaguchi, “Work function and microstructure of a monoatomic order surface layer grown on a (WSc2W3O12)-coated impregnated cathode,” *Vacuum*, vol. 41, no. 7–9, pp. 1759–1762, Jan. 1990.

[130] S. Yamamoto, I. Watanabe, S. Taguchi, S. Sasaki, and T. Yaguchi, “Formation mechanism of a monoatomic order surface layer on a sc-type impregnated Cathode,” *Jpn. J. Appl. Phys.*, vol. 28, no. 3 R, pp. 490–494, Mar. 1989.

[131] Z. Fisk, A. S. Cooper, P. H. Schmidt, and R. N. Castellano, “Preparation and lattice parameters of the rare earth tetraborides,” *Mater. Res. Bull.*, vol. 7, no. 4, pp. 285–288, Apr. 1972.

[132] Z. P. Yin and W. E. Pickett, “Rare-earth-boron bonding and 4f state trends in R B4 tetraborides,” *Phys. Rev. B - Condens. Matter Mater. Phys.*, vol. 77, no. 3, p. 035135, Jan. 2008.

[133] H. W. Hugosson, O. Eriksson, U. Jansson, A. V. Ruban, P. Souvatzis, and I. A. Abrikosov, “Surface energies and work functions of the transition metal carbides,” *Surf. Sci.*, vol. 557, no. 1–3, pp. 243–254, May 2004.

[134] J. G. Chen, “Carbide and Nitride Overlayers on Early Transition Metal Surfaces: Preparation, Characterization, and Reactivities,” *Chem. Rev.*, vol. 96, no. 4, pp. 1477–1498, 1996.

[135] C. C. Wang, S. A. Akbar, W. Chen, and V. D. Patton, “Electrical properties of high-temperature oxides, borides, carbides, and nitrides,” *J. Mater. Sci.*, vol. 30, no. 7, pp. 1627–1641, Jan. 1995.

[136] G. I. Kuznetsov and E. A. Sokolovsky, “Dependence of effective work function for LaB6 on surface conditions,” *Phys. Scr. T*, vol. 71, no. T71, pp. 130–133, 1997.

[137] S. Hosoki, S. Yamamoto, K. Hayakawa, and H. Okano, “Surface condition and thermionic emission of LaB6,” *Jpn. J. Appl. Phys.*, vol. 13, no. S1, pp. 701–704, 1974.

[138] C. Oshima, S. Horiuchi, and S. Kawai, “Thin film cathodes of lanthanum hexaboride (LaB6),” *Jpn. J. Appl. Phys.*, vol. 13, no. S1, pp. 281–284, 1974.

[139] M. Futamoto, M. Nakazawa, K. Usami, S. Hosoki, and U. Kawabe, “Thermionic emission properties of a single-crystal LaB_6 cathode,” *J. Appl. Phys.*, vol. 51, no. 7, pp. 3869–3876, 1980.

[140] M. Gesley and L. W. Swanson, “A determination of the low work function planes of LaB6,” *Surf. Sci.*, vol. 146, no. 2–3, pp. 583–599, Nov. 1984.

[141] H. Yamauchi, K. Takagi, I. Yuito, and U. Kawabe, “Work function of LaB6,” *Appl. Phys. Lett.*, vol. 29, no. 10, pp. 638–640, Nov. 1976.

[142] C. Oshima, E. Bannai, T. Tanaka, and S. Kawai, “Thermionic work function of LaB6 single crystals and their surfaces,” *J. Appl. Phys.*, vol. 48, no. 9, pp. 3925–3927, Sep. 1977.

[143] M. Aono, R. Nishitani, C. Oshima, T. Tanaka, E. Bannai, and S. Kawai, “Direct observation of LaB6(001) surface at high temperatures by x-ray and ultraviolet photoelectron spectroscopy, low-energy electron diffraction, Auger electron spectroscopy, and work-function measurements,” *J. Appl. Phys.*, vol. 50, no. 7, pp. 4802–4807, Jul. 1979.

[144] M. Aono, T. Tanaka, E. Bannai, and S. Kawai, “Structure and initial oxidation of the LaB6 (001) surface,” *Appl. Phys. Lett.*, vol. 31, no. 5, pp. 323–325, Sep. 1977.

[145] S. A. Chambers, P. R. Davis, L. W. Swanson, and M. A. Gesley, “Cesium and oxygen coadsorption on LaB6, single crystal surfaces. I. Work function change,” *Surf. Sci.*, vol. 118, no. 1–2, pp. 75–92, Jun. 1982.

[146] H. Kawanowa *et al.*, “Interaction of O2 with LaB6(0 0 1) surfaces as studied with MIES and UPS,” in *Surface Science*, 2001, vol. 482–485, no. PART 1, pp. 250–253.

[147] S. Zhou, J. Zhang, D. Liu, Q. Hu, and Q. Huang, “The effect of samarium doping on structure and enhanced thermionic emission properties of lanthanum hexaboride fabricated by spark plasma sintering,” *Phys. status solidi*, vol. 211, no. 3, pp. 555–564, Mar. 2014.

[148] S. Y. Ning *et al.*, “Enhanced thermionic emission performance of LaB6 by Ce doping,” *J. Alloys Compd.*, vol. 760, pp. 1–5, Sep. 2018.

[149] V. Katsap, “LaB6 cathode workfunction evaluation,” in *14th IEEE International Vacuum*

Electronics Conference, IVEC 2013 - Proceedings, 2013.

[150] W. Gosdy and W. J. Orville Thomas, "Electronegativities of the elements," *J. Chem. Phys.*, vol. 24, no. 2, pp. 439–444, Feb. 1956.

[151] S. Yamamoto, K. Susa, and U. Kawabe, "Work functions of binary compounds," *J. Chem. Phys.*, vol. 60, no. 10, pp. 4076–4080, May 1974.

[152] N. Bundaleski, J. Trigueiro, A. G. Silva, A. M. C. Moutinho, and O. M. N. D. Teodoro, "Influence of the patch field on work function measurements based on the secondary electron emission," *J. Appl. Phys.*, vol. 113, no. 18, p. 183720, May 2013.

[153] M. Yoshitake, "Generic trend of work functions in transition-metal carbides and nitrides," *J. Vac. Sci. Technol. A*, vol. 32, p. 61403, 2014.

[154] A. Neckel, P. Rastl, R. Eibler, P. Weinberger, and K. Schwarz, "Results of self-consistent band-structure calculations for ScN, ScO, TiC, TiN, TiO, VC, VN and VO," *J. Phys. C Solid State Phys.*, vol. 9, no. 4, pp. 579–592, Feb. 1975.

[155] H. B. Michaelson, "The work function of the elements and its periodicity," *J. Appl. Phys.*, vol. 48, no. 11, pp. 4729–4733, 1977.

[156] R. Smoluchowski, "Anisotropy of the Electronic Work Function of Metals," *Phys. Rev.*, vol. 60, no. 9, p. 661, 1941.

[157] W. T. Hong, K. A. Stoerzinger, B. Moritz, T. P. Devereaux, W. Yang, and Y. Shao-Horn, "Probing LaMO3 Metal and Oxygen Partial Density of States Using X-ray Emission, Absorption, and Photoelectron Spectroscopy," *J. Phys. Chem. C*, vol. 119, no. 4, pp. 2063–2072, 2015.

[158] D. Wrana, K. Cieślik, W. Belza, C. Rodenbücher, K. Szot, and F. Krok, "Kelvin probe force microscopy work function characterization of transition metal oxide crystals under ongoing reduction and oxidation," *Beilstein J. Nanotechnol*, vol. 10, pp. 1596–1607, 2019.

[159] M. Minohara, R. Yasuhara, H. Kumigashira, and M. Oshima, "Termination layer dependence of Schottky barrier height for La 0.6 Sr 0.4 MnO 3 Õ Nb: SrTiO 3 heterojunctions," *Phys. Rev. B*, vol. 81, no. 23, p. 235322, 2010.

[160] W. Maus-Friedrichs, M. Frerichs, A. Gunhold, S. Krischok, V. Kempter, and G. Bihlmayer, "The characterization of SrTiO3(0 0 1) with MIES, UPS(HeI) and first-principles calculations," *Surf. Sci.*, vol. 515, no. 2–3, pp. 499–506, Sep. 2002.

[161] I. Rastegar Alam, "Growth and Characterization of Transition Metal Oxide Heterostructures with a Tailored Work Function," 2018.

[162] Y. W. Chung and W. B. Weissbard, "Surface spectroscopy studies of the SrTiO3 (100) surface and the platinum-SrTiO3 (100) interface," *Phys. Rev. B*, vol. 20, no. 8, pp. 3456–3461, 1979.

[163] D. Wrana, C. Rodenbücher, W. Bełza, K. Szot, and F. Krok, "In situ study of redox processes on the surface of SrTiO3 single crystals," *Appl. Surf. Sci.*, vol. 432, pp. 46–52, Feb. 2018.

[164] W. J. Lo and G. A. Somorjai, “Temperature-dependent surface structure, composition, and electronic properties of the clean SrTiO3(111) crystal face: Low-energy-electron diffraction, Auger-electron spectroscopy, electron energy loss, and ultraviolet-photoelectron spectroscopy studies,” *Phys. Rev. B*, vol. 17, no. 12, pp. 4942–4950, 1978.

[165] L. F. Zagonel *et al.*, “Related content Orientation-dependent work function of in situ annealed strontium titanate,” *J. Phys. Condens. Matter*, vol. 21, p. 5, 2009.

[166] J. Padilla and D. Vanderbilt, “Ab initio study of SrTiO3 surfaces,” *Surf. Sci.*, vol. 418, no. 1, pp. 64–70, Nov. 1998.

[167] Z.-Q. Li, J.-L. Zhu, C. Q. Wu, Z. Tang, and Y. Kawazoe, “Relaxations of TiO2-and SrO-terminated SrTiO3 (001) surfaces,” *Phys. Rev. B*, vol. 58, no. 12, p. 8075, 1998.

[168] R. C. Hatch *et al.*, “Surface electronic structure for various surface preparations of Nb-doped SrTiO3 (001) ,” *J. Appl. Phys*, vol. 114, no. 10, p. 103710, 2013.

[169] R. A. Evarestov, A. V. Bandura, and V. E. Alexandrov, “Hybrid HF-DFT comparative study of SrZrO3 and SrTiO3 (001) surface properties,” *phys. stat. sol.*, vol. 243, no. 12, pp. 2756–2763, 2006.

[170] S. Piskunov, E. A. Kotomin, E. Heifets, J. Maier, R. I. Eglitis, and G. Borstel, “Hybrid DFT calculations of the atomic and electronic structure for ABO3 perovskite (001) surfaces,” *Surf. Sci.*, vol. 575, no. 1–2, pp. 75–88, Jan. 2005.

[171] E. Heifets, R. I. Eglitis, E. A. Kotomin, J. Maier, and G. Borstel, “First-principles calculations for SrTiO3(100) surface structure,” *Surf. Sci.*, vol. 513, no. 1, pp. 211–220, Jul. 2002.

[172] Z. Wang *et al.*, “Transition from Reconstruction toward Thin Film on the (110) Surface of Strontium Titanate,” *Nano Lett*, vol. 16, no. 4, pp. 2407–2412, 2016.

[173] Z. Wang *et al.*, “Strain-Induced Defect Superstructure on the SrTiO3 (110) Surface,” *Phys. Rev. Lett.*, vol. 111, no. 5, p. 056101, 2013.

[174] D. Wrana, K. Cieślik, W. Belza, C. Rodenbücher, K. Szot, and F. Krok, “Kelvin probe force microscopy work function characterization of transition metal oxide crystals under ongoing reduction and oxidation,” *Beilstein J. Nanotechnol*, vol. 10, pp. 1596–1607, 2019.

[175] R. Bachelet, F. Sánchez, F. J. Palomares, C. Ocal, and J. Fontcuberta, “Atomically flat SrO-terminated SrTiO3(001) substrate,” *Appl. Phys. Lett.*, vol. 95, no. 14, p. 141915, Oct. 2009.

[176] Y. Xiong, W. Chen, W. Guo, H. Wei, and I. Dabo, “Data-driven analysis of the electronic-structure factors controlling the work functions of perovskite oxides,” *Phys. Chem. Chem. Phys.*, 2021.

[177] T. Mayeshiba *et al.*, “The MAterials Simulation Toolkit (MAST) for atomistic modeling of defects and diffusion,” *Comput. Mater. Sci.*, vol. 126, pp. 90–102, 2017.

[178] X. F. Chen, H. Lu, W. G. Zhu, and O. K. Tan, “Enhanced field emission of silicon tips coated with sol–gel-derived (Ba0.65Sr0.35)TiO3 thin film,” *Surf. Coatings Technol.*, vol.

198, no. 1–3, pp. 266–269, Aug. 2005.

[179] X. F. Chen *et al.*, “Si field emitter arrays coated with thin ferroelectric films,” *Ceram. Int.*, vol. 34, pp. 971–977, 2008.

[180] H. J. Bian *et al.*, “Electron emission from SrTiO3-coated silicon-tip arrays,” *J. Vac. Sci. Technol. B*, vol. 25, no. 3, pp. 817–821, 2007.

[181] X. Chen, H. Lu, H. Bian, W. Zhu, C. Sun, and O. K. Tan, “Electron emission of silicon field emitter arrays coated with N-doped SrTiO3 film,” *J. Electroceramics*, vol. 16, no. 4, pp. 419–423, Jul. 2006.

[182] P. C. Fletcher, V. K. R. Mangalam, L. W. Martin, W. P. King, and P. C. Fletcher, “Field emission from nanometer-scale tips of crystalline PbZrxTi1 − xO3 Field emission from nanometer-scale tips of crystalline PbZr x Ti 1 2 x O 3,” vol. 021805, no. 2013, pp. 0–6, 2015.

[183] R. Jacobs, J. Hwang, Y. Shao-Horn, and D. Morgan, “Assessing Correlations of Perovskite Catalytic Performance with Electronic Structure Descriptors,” *Chem. Mater.*, vol. 31, no. 3, pp. 785–797, Feb. 2019.

[184] J. E. Saal, S. Kirklin, M. Aykol, B. Meredig, and C. Wolverton, “Materials design and discovery with high-throughput density functional theory: The open quantum materials database (OQMD),” *JOM*, vol. 65, no. 11, pp. 1501–1509, 2013.

[185] W. Sun *et al.*, “The thermodynamic scale of inorganic crystalline metastability,” *Sci. Adv.*, vol. 2, pp. 1–8, 2016.

[186] Y. Wu, P. Lazic, K. Persson, and G. Ceder, “First principles high throughput screening of oxynitrides for water-splitting photocatalysts,” *Energy Environ. Sci.*, vol. 6, pp. 157–168, 2013.

[187] S. Hui and A. Petric, “Conductivity and stability of SrVO3 and mixed perovskites at low oxygen partial pressures,” *Solid State Ionics*, vol. 143, pp. 275–283, 2001.

[188] Y. C. Lan, X. L. Chen, and M. He, “Structure, magnetic susceptibility and resistivity properties of SrVO3,” *J. Alloys Compd.*, vol. 354, pp. 95–98, 2003.

[189] J. Macias, A. A. Yaremchenko, and J. R. Frade, “Enhanced stability of perovskite-like SrVO3-based anode materials by donor-type substitutions,” *J. Mater. Chem. A*, vol. 4, pp. 10186–10194, 2016.

[190] Y.-L. Lee, J. Kleis, J. Rossmeisl, and D. Morgan, “Ab initio energetics of LaBO3 (001) (B = Mn, Fe, Co, and Ni) for solid oxide fuel cell cathodes,” *Phys. Rev. B*, vol. 80, no. 22, p. 224101, 2009.

[191] J. Wang *et al.*, “Oxygen Vacancy Induced Band-Gap Narrowing and Enhanced Visible Light Photocatalytic Activity of ZnO,” *ACS Appl. Mater. \& interfaces*, vol. 4, no. 8, pp. 4024–4030, 2012.

[192] Y. Lee, M. J. Gadre, Y. Shao-horn, and D. Morgan, “Ab initio GGA+U study of oxygen evolution and oxygen reduction electrocatalysis on the (001) surfaces of lanthanum

transition metal perovskites $LaBO_3$ (B = Cr, Mn, Fe, Co and Ni)," *Phys. Chem. Chem. Phys.*, vol. 17, pp. 21643–21663, 2015.

[193] R. Jacobs *et al.*, "Perovskite electron emitters: Computational prediction and preliminary experimental assessment of novel low work function cathodes," in *2018 IEEE International Vacuum Electronics Conference, IVEC 2018*, 2018, pp. 37–38.

[194] V. Katsap, "Low temperature, high-brightness, cathode," 2020.

[195] J. Macias, A. A. Yaremchenko, D. P. Fagg, and J. R. Frade, "Structural and defect chemistry guidelines for Sr(V,Nb)O3-based SOFC anode materials," *Phys. Chem. Chem. Phys.*, vol. 17, pp. 10749–10758, 2015.

[196] T. C. Leung, H. Hu, A. J. Liu, and M. C. Lin, "Adsorbate induced modulation of strain effects on work functions of a tungsten (100) surface," *Phys. Chem. Chem. Phys.*, vol. 21, no. 46, pp. 25763–25772, Nov. 2019.